Air Force Office of Scientific Research #AFOSR-91-0269

PARAMETERIZATION OF ICE CRYSTAL CONVERSION PROCESSES IN CIRRUS CLOUDS USING DOUBLE-MOMENT BASIS FUNCTIONS

by Jerry L. Harrington

William R. Cotton, P.I.

Colorado State University

DEPARTMENT OF ATMOSPHERIC SCIENCE

PAPER NO. 554

PARAMETERIZATION OF ICE CRYSTAL CONVERSION PROCESSES IN CIRRUS CLOUDS USING DOUBLE-MOMENT BASIS FUNCTIONS

by

Jerry L. Harrington

Department of Atmospheric Science

Colorado State University

Fort Collins, CO 80523

Research Supported by

Air Force Office of Scientific Research

under Grant #AFOSR-91-0269

April 5, 1994

Atmospheric Science Paper No. 554

ABSTRACT

PARAMETERIZATION OF ICE CRYSTAL CONVERSION PROCESSES IN CIRRUS CLOUDS USING DOUBLE-MOMENT BASIS FUNCTIONS

With the onset of increased scientific interest in cloud-effects on climate and the need of cirrus forecasts to support military operations and the aviation industry has come the need to develop more credible microphysical parameterizations of the ice transfer processes occuring in cirrus clouds. Herein a parameterization is developed for the transfer between two defined categories of ice; pristine ice (which grows by vapor deposition only and is constrained to have mean diameters less than 125 μm) and snow (resulting from the direct conversion of pristine ice). Each category is assumed to conform to a generalized gamma distribution function, with variations in ice crystal habits allowed. Analytical transfer equations for the flux of number concentration and mass between the pristine ice and snow categories during ice supersaturated and subsaturated atmospheric regimes are derived. A parameterization of ice number concentration loss from each of these distributions during sublimation is also described.

These parameterizations are tested in a one-dimensional Lagrangian parcel model for ice supersaturated ascents and ice subsaturated decents. These tests allow analysis of the parameterizations during variations in physical parameters such as the shape of assumed distributions and the ice crystal habit. It is shown that variations in both of these parameters have large impacts on the evolution of the distribtutions. These results show similarities to other modeling efforts.

The ice parameterizations are implemented into the Regional Atmospheric Modeling System (RAMS) developed at CSU and two-dimensional sensitivity tests are conducted using observations from the November 26, 1991 FIRE II cirrus case. Tests of the model using rosette crystals and exponential distribution shapes showed the flexibility of the RAMS model in simulating these systems. The RAMS results compared favorably with data obtained during the FIRE II field project. Tests with larger values of the distribution shape parameter showed possible improvements over the test case in that larger ice masses were found near cloud bases (as was observed). The type of crystal modeled was shown to have a large impact on the microphysical evolution of the simulated cirrus system; cloud depth, ice water content (IWC), number concentrations and updraft profiles were all sensitive to these changes. Tests that examined the profiles of ice nuclei (IN), radiative parameterization, and two moment versus one moment predictions all showed the importance of credible parameterizations and of correct model initialization.

Jerry L. Harrington
Department of Atmospheric Science
Colorado State University
Fort Collins, Colorado 80523
Spring 1994

ACKNOWLEDGEMENTS

My most sincere and warmest thanks are extended to my advisor, William R. Cotton, for his guidance and support during the development of the ice parameterization. My graduate committee, Professors Stephen K. Cox and Paul W. Mielke, are thanked for their time and consideration of this manuscript; their comments were most helpful. Many thanks are extended to Robert Walko for his much needed help with version 3a of the RAMS model and for many endearing microphysical conversations. A special note of thanks is extended to Michael P. Meyers for his suggestions and comments on not only this manuscript but also the modeling work. Hans Verlinde and Lewis Grasso were both very helpful with giving mathematical suggestions and, at times, reviewing some of my ideas. My word processing abilities and the use of Latex to type this thesis would have been greatly hindered without the help of Brenda Thompson and Abby Hodges; you two have been a lot of fun to work with! I also would like to extend a much needed and appreciated note of gratitude to all of my friends, not only the ones here at Colorado State University, but also my old friends at the University of Iowa who have made such a concerted effort to keep our friendship alive over such a long distance.

Finally, a very special note of thanks goes out to Debra Youngblood for her much needed support during the completion of this thesis.

This research was supported by the Air Force Office of Scientific Research (AFOSR) under contract # AFOSR-91-0269. Computations were performed on a RISC 6000 workstation purchased under support of the National Oceanic and Atmospheric Administration (NOAA) contract # NA90RHH-00077.

TABLE OF CONTENTS

1 INTRODUCTION 1

2 PREVIOUS WORK 3
2.1 Microphysics 3
2.2 Dynamics of Cirrus 6
2.3 Mesoscale and Cloud Scale Modeling of Cirrus Clouds 7

3 THE RAMS MODEL 11
3.1 Model Description 11
3.2 Model Microphysics 12
3.3 Ice Nucleation 14
3.3.1 Heterogeneous nucleation of ice 15
3.3.2 Homogeneous nucleation of ice 16
3.4 Two-Moment Predictions 19

4 THE BIMODAL ICE SPECTRA 20
4.1 Theoretical Development 20
4.1.1 Crystal Capacitance 21
4.1.2 Development of the Flux Equations 22
4.2 Loss of Ice Species by Sublimation 34

5 MICROPHYSICAL TESTS USING A ONE-DIMENSIONAL LAGRANGIAN MODEL 45
5.1 Lagrangian Model 45
5.2 Results of the One-Dimensional Simulations 47
5.2.1 Distribution Bounds 47
5.2.2 One-dimensional simulations 49

6 THE NOVEMBER 26, 1991 FIRE II CIRRUS EVENT: OBSERVATIONS 68
6.0.3 Cirrus cloud development and dynamics 68
6.1 Microphysical observations 73

7 TWO-DIMENSIONAL SENSITIVITY TESTS WITH RAMS 79
7.1 Control Simulation and Comparison with Observations 81
7.2 Sensitivity Tests of the Model Parameterizations 90
7.2.1 Needle Crystals, Snow and Aggregate Distribution Shape, $\nu = 1$ 90
7.2.2 Plate Crystals with Snow Distribution Shape $\nu = 1$ 97
7.2.3 Needle crystals with Snow Distribution Shape $\nu = 3$ 101
7.2.4 Rosettes with Snow and Aggregate Distribution Shape $\nu = 3$ 104

7.2.5 Rosette Crystals, Single Moment Predictions 106
7.2.6 Rosettes without the Radiative Parameterization 110
7.2.7 Rosettes without Homogeneous Nucleation 112
7.2.8 Needles with a Modified Sounding 115
7.2.9 Rosettes with Perturbed Ice Nuclei Profile 118

8 SUMMARY AND CONCLUSIONS 121
8.1 Conclusions 121
8.2 Future Research 126

LIST OF FIGURES

4.1 Example of the bimodal spectra 23
4.2 The bin representation 35
4.3 Fractional mass vs. fractional number loss: S_i variation 39
4.4 Fractional mass vs. fractional number loss: T variation 39
4.5 Fractional mass vs. fractional number loss: P variation 40
4.6 Fractional mass vs. fractional number loss: $\bar{D}$ variation 40
4.7 Fractional mass vs. fractional number loss: P, T, and $\bar{D}$ variation 41
4.8 Fractional mass vs. fractional number loss: ν variation 42
4.9 Fractional mass vs. fractional number loss: Habit variation 43

5.1 Example of distribution evolution 48
5.2 Saturated ascent distribution evolution: Needle PI with $\nu = 3$ 51
5.3 S_i vs. Pressure: Needle PI with $\nu = 3$ 51
5.4 $\bar{D}$ vs. pressure: Needle PI with $\nu = 3$ 52
5.5 Δr vs. pressure for model ascent: Needle PI with$\nu = 3$ 52
5.6 N_t vs. pressure: Needle PI with $\nu = 3$ 53
5.7 Distribution evolution for subsaturated descent: Pristine ice $\nu = 3$ 53
5.8 Δr vs. pressure for model descent: Needle PI with $\nu = 3$ 54
5.9 Distribution evolution during model ascent: Needle PI with ν =1 56
5.10 S_i vs. pressure: Needle PI with ν =1 56
5.11 N_t vs. pressure: Needle PI with ν =1 57
5.12 Distribution evolution for model descent: Needle PI with ν =1 57
5.13 Δr vs. pressure for model ascent: Needle PI with ν =1 58
5.14 $\bar{D}$ vs. pressure: Needle PI with ν =1 58
5.15 Δr vs. pressure for model descent: Needle PI with ν =1 59
5.16 Distribution evolution for model ascent: Plate PI with ν =1 60
5.17 $\bar{D}$ vs. pressure: Plate PI with ν =1 60
5.18 N_t vs. pressure: Plate PI with ν =1 61
5.19 r_t vs. pressure: Plate PI with ν =1 61
5.20 Δr vs. pressure for model ascent: Plate PI with ν =1 62
5.21 Distribution evolution for model descent: Plate PI with ν =1 62
5.22 Δr vs. pressure for model descent: Plate PI with ν =1 63
5.23 dD/dt vs. D: variations in S_i 65

6.1 300 mb analysis of heights/isotachs for 0000 UTC, November 26, 1991. 69
6.2 300 mb analysis of heights/isotachs for 1200 UTC, November 26, 1991. 69
6.3 300 mb analysis of heights/isotachs for 0000 UTC, November 27, 1991. 70
6.4 700 mb NGM analysis of heights/RH for 0000 UTC, November 27, 1991. 70
6.5 Wind speeds contoured at 10km on Nov. 26, 1991 71

6.6 Vertical vorticity cross-sections for 1800 UTC and 2100 UTC on the 26th of November, 1991. 72
6.7 Vertical velocities from adiabatic flow for 1800 and 2100 UTC. 72
6.8 2D-C probe and ice replicator measurementsof ice crystal habits and sizes. . . . 74
6.9 Spectral representation of the 2D-C probe and ice replicator data. 75
6.10 Time-height cross-section of retrieved ice crystal concentrations. 76
6.11 Time-height cross-section of retrieved ice crystal median diameters. 76
6.12 Time series of retrieved effective radius, number concentration, and IWC. . . . 77
6.13 Radar echo boundaries of the November 26, 1991 cirrus event. 78

7.1 King Air and Saberliner data in cloud for the November 26, 1991 cirrus case. . 80
7.2 Total Ice Mixing Ratio for the RN1 simulation. 82
7.3 W (m/s) for the RN1 simulation. 82
7.4 RN1 Pristine Ice Mixing Ratio. 84
7.5 RN1 Pristine Ice Concentration. 84
7.6 RN1 Pristine Ice Size. 85
7.7 RN1 Snow Mixing Ratio. 85
7.8 RN1 Snow Concentration. 86
7.9 RN1 Snow Size. 86
7.10 RN1 Aggregate Mixing Ratio. 87
7.11 RN1 Aggregate Concentration. 87
7.12 RN1 Aggregate Size. 88
7.13 RN1 Total Mixing Ratio. 88
7.14 RN1 w field 89
7.15 RN1 Total Mixing Ratio Time-Series. 89
7.16 NN1 Pristine Ice Mixing Ratio. 93
7.17 NN1 Pristine Ice Concentration. 93
7.18 NN1 Pristine Ice Size. 94
7.19 NN1 Snow Mixing Ratio. 94
7.20 NN1 Snow Concentration. 95
7.21 NN1 Snow Size. 95
7.22 NN1 Total Ice Mixing Ratio. 96
7.23 PN1 Pristine Ice Mixing Ratio. 98
7.24 PN1 Pristine Ice Concentration. 98
7.25 PN1 Pristine Ice Size 99
7.26 PN1 Snow Mixing Ratio. 99
7.27 PN1 Snow Concentration. 100
7.28 PN1 Snow Size. 100
7.29 NN3 Total Ice Mixing Ratio. 102
7.30 NN3 Pristine Ice Concentration. 102
7.31 NN3 Snow Concentration. 103
7.32 NN3 Pristine Ice Size. 103
7.33 RN3 Total Ice Mixing Ratio. 105
7.34 RN3 Pristine Ice Concentration. 105
7.35 RN3 Snow Concentration. 106
7.36 RSM Pristine Ice Mixing Ratio. 107
7.37 RSM Pristine Ice Concentration. 107
7.38 RSM Snow Mixing Ratio. 108

7.39 RSM Aggregate Mixing Ratio. 108
7.40 RNR Total Ice Mixing Ratio. 110
7.41 RNR Pristine Ice Concentration. 111
7.42 RNR Snow Concentration. 111
7.43 RNR w Fields. 112
7.44 RNH Total Ice Mixing Ratio. 113
7.45 RNH Pristine Ice Concentration. 113
7.46 RNH Snow Concentration. 114
7.47 N5RH Total Ice Mixing Ratio. 116
7.48 N5RH Pristine Ice Concentration. 116
7.49 N5RH Snow Concentration. 117
7.50 N5RH Pristine Ice Size. 117
7.51 RCIN Total Ice Mixing Ratio. 118
7.52 RCIN Pristine Ice Concentration. 119
7.53 RCIN Snow Concentration. 120

Chapter 1

INTRODUCTION

Cirrus clouds have a complex microphysical structure that seems to be strongly linked to their radiative properties and their heating and dynamics (Mitchell, 1994; Flatau, 1990). The growth of real ice crystals in the cloud environment is a complex process involving diffusion kinetics (the release of latent heat and its transfer to the environment which is a function of vapor content, temperature gradient, and pressure), surface tension effects, and crystalline anisotropy (Langer, 1980). Models of crystal formation and growth can be extremely complex (e.g. see Ben-Jacob et al., 1983) involving sets of differential equations and complex solution methods. Even with these models, there is still much uncertainty about the growth of ice crystals and their variation in habit. Habit variation itself, is quite important to the radiative properties of cirrus clouds (Flatau, 1992; Mitchell, 1994), and to their feedback on any given climate change event (Stephens et al., 1990). In the world of cloud modeling, these processes must be parameterized in order to correctly simulate a cloud system, especially cirrus. Crystalline habit, and their subsequent size distributions, are quite important to the physical processes of cirrus clouds. Habit determines growth rates and fall velocities which, in turn, has an effect on the depth of the layer. Crystalline habit effects the absorption and scattering of cirrus clouds; this has an effect on the heating of the cloud system and, therefore, on the dynamical structure. Thus, it is important to model cirrus microphysical processes correctly if one is to successfully simulate these systems.

Unfortunately, in the realm of multi-dimensional numerical cloud modeling, one does not have the computational freedom to explicitly define crystal growth, habit change, and size distributions. Parameterizations need to be found which cover, in a simple set of equations, the most relevant physical processes associated with cloud systems. To address the problem of modeling cirrus clouds, with the ultimate goal of forecasting these systems operationally or parameterizing them in global models, the Regional Atmospheric Modeling System (RAMS) developed at Colorado State University was used. The RAMS model sports a new microphysical package that includes 7 hydrometeor species (pristine ice, snow, aggregates, cloud water, hail, graupel, and rain) with predictions on two-moments of the hydrometeor spectra (number concentration and mass mixing-ratio) for all species except cloud water. Because of recent observational evidence showing the possibility for the existence of a bimodal spectra of ice in cirrus clouds (Arnott et al., 1993), a parameterization was developed in which ice is allowed to have two separate distributions (defined as pristine ice and snow). Within this parameterization, the possibility exists for the addition of the two distributions to have only one mode, if the model physics dictates it. Transfer equations are developed in which pristine ice is allowed to transfer into the snow category during ice supersaturated cloud regimes. A similar transfer occurs in the reverse direction (snow to pristine ice) in ice subsaturated regimes. Number concentration loss during ice subsaturation is parameterized for both the pristine ice and snow distributions with the smallest crystals in the distribution evaporating first. Depending upon the environmental variables in the model six crystal habits are possible; plates, columns, needles, spheres, dendrites, and bullet rosettes.

Background information on cirrus cloud microphysics, radiative properties, dynamics, and modeling efforts are presented in Chapter 2. The RAMS model is described in Chapter 3 with specific attention paid to the new microphysical package. In Chapter 4 efforts are directed toward the development of the bimodal ice representation, including the mass mixing-ratio and number concentration transfer scheme and the parameterization of number concentration loss of ice species to sublimation. In Chapter 5 the evolution of the ice spectra in a simple one-dimensional Lagrangian parcel model is discussed. The FIRE II case study of November 26, 1991 is briefly overviewed and microphysical results are discussed in Chapter 6. The two-dimensional simulations and sensitivity studies of the November 26, 1991 FIRE II are presented in Chapter 7. Chapter 8 contains summary and conclusions of this work and suggestions for future research.

Chapter 2

PREVIOUS WORK

The modeling of cirrus clouds, even with cloud scale models, is a challenging endeavor. Cirrus cloud dynamics and the complexity of the detail in their microphysical structure tends to test the limits of physical theory and model parameterizations. A large difficulty in making a credible physical hypothesis about the nature of cirrus structure is the limited measurements of the properties of these clouds due to their atmospheric "remoteness". Recently, evidence is mounting that these clouds, due to their structure and high global frequency, are important in the global radiation budget and, thus, in calculating atmospheric climatic effects. Because of the far reaching implications of these clouds, this section will be directed towards a brief explanation of not only the microphysical structure of these clouds but also the dynamical structure. A final section deals with modeling work related to the mesoscale modeling developed here.

2.1 Microphysics

As was stated in the introduction, the microphysical properties of cirrus clouds are quite important because of the complex structure of the ice that makes up these clouds and the interactions of the growth of ice habits, radiative interactions, and effects on the dynamical structure of these clouds.

Measurements by Heymsfield et al. (1972) of the crystalline habits, size distributions, number concentrations and ice water contents (IWC) in cirrus uncinus, cirrus spissatus, cirrostratus, and a cumulonimbus cirrus shield showed number concentration, size distribution, and IWC variation with cloud type. Cirrus uncinus tended to have the largest IWC and number concentration (excluding the anvil cirrus shield) with number concentrations up to 40,000 m^{-3} and IWC up to 0.27 $g\ m^{-3}$. The cumulonimbus cirrus shield had number concentrations and IWC in excess of 100,000 m^{-3} and 1.0 $g\ m^{-3}$ respectively. The maxima in IWC occurred near cloud base, as would be expected since more massive crystals falling out of the updraft would be located here. The size spectra varied between cloud types, but showed distinctive gamma-type distribution shapes. Variations in habit were also noted, with bullets, columns, and bullet rosettes dominating the generating cells and the larger sizes while plates were associated with the smaller crystal sizes. These measurements, however, were restricted to crystal sizes above about 100 μm since this was the limit of the spectrometers lower range. Later measurements by Heymsfield (1975) showed large number concentrations in the size range 25-50 μm.

Heymsfield (1975) also showed that vertical velocities and temperature play a role in the determination of IWC (as was suggested by the measurements given above). When temperature or vertical velocities increased, it was found that there was a subsequent increase in the measured IWC. The nucleation rate of ice crystals and water drops in clouds are also known to be a function of the updraft profile.

There is also the possibility for the existence of supercooled water at cirrus levels. Recently, during the FIRE II experiment December 5, 1991 cirrus case, aircraft wing icing was noted. This is not possible with solid ice and presumes some sort of liquid water content in these clouds. Sassen (1992) conjectured that aerosol particles from the Mnt. Pinitubo eruption carried by the jet stream influenced the formation of cirrus clouds on this day. These aerosol could have been abundant enough to allow the formation of supercooled water droplets. Lidar measurements suggested the existence of liquid water topped cirrus uncinus on the day in question. It is expected that volcanic aerosols change the microphysical structure of the cirrus cloud and, therefore, its radiative properties. This influence may have a climatic effect (Sassen (1992)).

During the FIRE II experiment in Coffeeville, Kansas Arnott et al. (1993) used ice particle replicator data to show the existence of a bimodal spectrum of ice particles in cirrus clouds. Small ice was shown to have an exponential shape with a maximum dimension between 125-150 μm while a second peak was evident with a gamma-type distribution shape and a mean maximum dimension around 400-500 μm. Hein et al. (1993), using a forward Monte Carlo method spectral model, showed the need for a large concentration of small ice (maximum dimensions less than 50 μm) in their model in order to have their spectral calculations conform to observations. Larger concentrations at smaller particle sizes were inferred by Intrieri et al. (1993) during the FIRE II experiment with CO_2 lidar and 8mm radar. Particle concentrations in the upper level of a cirrus deck that occurred on 26 November 1991 were of small sizes (about 25-65 μm) with number concentrations of about 1000 l^{-1}.

Mitchell et al. (1989) and Mitchell et al. (1994) used data from orographic winter storms to derive mass-dimensional relationships for ice particles of different habits of the form,

$$m = \alpha D^{\beta} \tag{2.1}$$

where D is the maximum dimension of a given crystal. It was found that for needle and column type habits that the mass exponent, β, was around 1.8 while for more spatial habits such as hexagonal plates and bullet rosettes it is around 2.5.

Habits of ice particles, as stated previously, are very important to the scattering and absorptive properties of cirrus clouds. Ice particles in cirrus tend to orient themselves with the maximum dimensions horizontally. This has important implications for scattering calculations since different habits will tend to have different cross-sectional areas (Mitchell et al., 1994). Also, differing ice habits have different path lengths through the individual crystals, which has important implications when it comes to the scattering and absorptive properties of the cloud system.

Stackhouse et al. (1990) examined the radiative properties of cirrus clouds using a two-stream radiative transfer model. They found that the longwave heating and shortwave cooling of a cirrus deck depends upon the amount of ice in the clouds. It was also found that the longwave budget is altitude dependent, with cirrus clouds in the tropics (of generally higher altitude) produced a net heating while subarctic cirrus (generally lower altitude) produced a net cooling. The higher altitude tropical cirrus were more sensitive to changes in the IWC of the cloud. The addition of small ice particles (maximum dimensions less than 44 μm) with larger number concentrations had a large impact on solar wavelength scattering (because of increased projected surface areas) and longwave absorption, with increases in both.

Using a two-stream radiative transfer model and a simple climate model Stephens et al. (1990) showed that the assumed values of the asymmetry parameter, g, and the effective radius of cirrus ice particles, r_e are important when calculating the climate feedback effects of cirrus clouds. Cirrus clouds with an assumed asymmetry parameter of 0.87 produced about two times the warming during a CO_2 warming event as simulations with an asymmetry parameter of 0.7. The calculated climate feedback was found to vary between warming and cooling depending upon the value of r_e assumed.

2.2 Dynamics of Cirrus

The dynamical processes that control the formation of cirrus clouds are as varied as the forms of cirrus themselves. Cirrus clouds can form via upper level frontal lifting, from the motions around jet streams, upward propagation of waves produced by orography, or mountain waves, ascending motions in extra-tropical cyclones, and cumulonimbus anvil outflow. However, there are some features of the dynamical processes associated with cirrus clouds and their formation that are quite similar. For example, Heymsfield et al. (1972) noticed in case studies of cirrus uncinus, cirrus spissatus, cirrostratus, and a cumulonimbus cirrus shield, that all cirrus seem to form by some sort of generating cell with convective motions associated with it. Heymsfield (1975) showed that cirrus clouds usually form in regions where stable layers exist below cloud and above cloud. These layers are usually thin and are shown in the usual "thinness" that is characteristic of cirrus.

The generation of turbulent kinetic energy (TKE) in cirrus is not likely associated with an external diabatic heat source related to surface heating such as is normally observed in stratocumulus (Flatau et al., 1990). Generation is most likely associated with radiative effects, vertical wind shear, wave instabilities, or latent heat release. Turbulence associated with cirrus clouds can generally be characterized as two-dimensional. Flatau et al. (1990), using data from the FIRE experiment in Oshkosh, Wisconsin, and the GASP experiment found that vertical velocity variances were about an order of magnitude less than the u and v variances; thus suggesting a two-dimensional nature to turbulence in cirrus. Flatau also found that TKE production within cloudy air was noticeably higher than in clear air. The authors postulated that turbulence must be due to in-cloud processes. Along similar lines, Starr and Cox (1980) noted that buoyancy production of TKE was larger than shear production, indicating turbulence origins within cloud.

Using the FIRE data set, Gultepe et al. (1990) did calculations of the moisture and heat budgets of cirrus clouds. The moisture budget of cirrus associated with the October 31, 1987 case was characterized by moisture convergence at low and mid-levels and moisture divergence at cloud top. Moisture sources and sinks seemed to be dominated by advection at all levels with microphysics having some significant contributions at mid-level. The heat budget of the cirrus system was dominated by vertical advection and radiative cooling.

2.3 Mesoscale and Cloud Scale Modeling of Cirrus Clouds

Modeling cirrus clouds is difficult because of the intricate interactions of microphysics, radiative properties, and cloud dynamics (Flatau et al., 1990). Even though, the modeling of cirrus clouds has taken many routes, some modelers have explained cirrus-anvil cloud structure and dynamics with mixed-layer theory which exploits various similarities between cirrus clouds and stratocumulus (Lilly (1988)). Modeling cirrus in this fashion requires a well mixed layer with a dry adiabatic lapse rate sandwiched between two stable layers. An external diabatic heat source (as is usually the case in stratocumulus) is not present in cirrus clouds because of a lack of a heated lower boundary. Outside mechanisms for the generation of TKE in cirrus exist; such as radiative effects, latent heating from particle growth, shear production, gravity waves, orographic effects and lifting due to ageostrophic circulations in jet streaks. Lilly (1988) used this model to describe cirrus that forms in the outflow regions of cumulonimbus clouds, where the 3-D convectively generated turbulence collapses to 2-D turbulence. Flatau et al. (1990) used this model of cirrus clouds along with bulk microphysical and radiative properties to derive a model of cirrus for use in global climate models.

A two-dimensional cloud scale model was developed by Starr and Cox (1985) for the simulation of cirrus clouds. The 2-D model (x and z directions) had 100m resolution in both the x and the z directions and a model timestep of 30 seconds. The model parameterizations included the phase changes of water, radiative processes, and the vertical flux of ice. These parameterizations were based upon observational evidence when possible. The model was constrained in the types of cirrus that it could reasonably simulate due to the fact that it was restricted to temperatures between -25 and -45 °C, weak vertical velocities, and no vertical shear (which makes it difficult to simulate cirrus uncinus clouds). Their results were reasonable, with profiles of ice water content, vertical motions, scale between convective cells, and cirrus layering effects all in good agreement with observations. The results of these modeling efforts showed that the physical properties of cirrus are highly dependent upon the large scale ascent (descent) and to changes in the microphysical properties. Tests of the effects of day and night radiational effects on cirrus showed that the daytime cirrus tended to be more convectively active but less dense in structure when compared to the nocturnal case. This seems to show how radiational variations can affect in-cloud buoyancy.

Mitchell et al. (1994) derived an analytical model for cirrus microphysics using a gamma function for ice habits of the form,

$$N(D) = N_0 D^{\nu} exp(-\lambda D). \tag{2.2}$$

Using a general dynamic expression for the number concentration of the given ice species, Mitchell came up with both first and second order mass-moment conserving equations. The model allows for hexagonal plates, hexagonal columns, and bullet rosette ice crystals. Changes in habit within cloud layers is accounted for and happens suddenly with changes in the ambient temperature (number concentration is varied in order to keep the IWC field constant during the change). Mass-dimensional relationships of the form $m(D) = \alpha D^{\beta}$ are used in the model where the exponential term β can be thought of as a measure of the growth of any given ice crystal. The model is initialized with a predetermined IWC field (assumed horizontally homogeneous) and u and v wind fields but does not prognose changes to these initial fields. The model performed well when compared with observations of IWC, number concentration, and maximum dimensions. The most notable conclusions drawn from these simulations lies in the effects of various variables on the size distributions. It was shown the cloud updrafts had the general characteristic of increasing distribution breadth and lowering number concentrations when compared to simulations with no updraft. The updraft simply increased the response of ice crystal growth to any change in IWC. Changes in habit produced noticeable changes in the distribution parameters. This is easily seen to be due to differences in the parameter β in the mass-dimensional relationship. Larger values of β cause smaller increases in particle size for any given growth conditions. Thus, ice columns (with $\beta = 1.8$) grow faster than bullet rosettes (with $\beta = 2.26$). A change in crystal habit from columns to spacial crystals has the tendency to narrow the size distribution and increase number concentrations (since IWC is held constant during the change). Aggregation may negate this effect since it decreases number concentrations and increases sizes (thus, distribution breadth). Mitchell stated, however, that since aggregation in cirrus is not well understood on a quantitative level (the collection kernel is not well defined) (but is quite commonly observed) this process could not be looked at in any real detail.

These differences in size distributions and their dependencies upon ice crystal habits also has important implications when it comes to cirrus cloud radiative properties. With so much recent emphasis placed upon global climate change coupled with the fact that cirrus clouds are quite frequent globally, questions about the influence of cirrus clouds on a global warming event (or the effects of cirrus frequency due to warming) are being asked. In the literature, there seems to have been considerable evidence showing that cirrus clouds can have a positive feedback on a global warming event. Studies by Mitchell et al. (1989), however, have shown that the feedback can be negative. Radiative transfer models that are used in GCM's for climate study need parameters such as crystalline asymmetry parameters, cloud optical depth, and absorptive and reflective cirrus properties in order to simulate cirrus effects. Mitchell et al. (1994) shows that these parameters are quite sensitive to the habit of the crystal chosen. In their study, the absorptive properties of cirrus crystals are not allowed to be parameterized through effective area spheres (since the path of a ray of light through a sphere can be much longer than that of a needle crystal or rosette). They parameterize an effective distance, d_e, through given crystal habits and integrate the effect over the entire size distribution in order to get absorption and reflection from the cirrus layer. This has the effect of decreasing the absorption by cirrus clouds and increasing their single scattering albedo. The study also showed that absorption and single scatter albedo are a strong function of crystal habit. Bullet rosettes had less absorption and larger single scattering albedos than did clouds with columnar crystals (this is, again due to the fact that the rosettes have narrower distributions and, thus, larger projected areas).

Heckman et al. (1993) used the RAMS model developed at Colorado State University to simulate cirrus cloud systems observed on the 26th of October during the FIRE 1986 experiment in Oshkosh, Wisconsin. The RAMS model is a mesoscale model and has the capability of nested-grids. The model prognoses the wind components, the ice-liquid water potential temperature, density of dry air, total liquid mass mixing-ratio, the mixing ratio's of the hydrometeor species, and the concentration of pristine ice crystals (all other number concentrations are diagnosed). Heckman used hexagonal plates as the crystalline habit and pristine ice nucleation was calculated with the hybrid nucleation of Cotton et al. (1986). Resolution in the vertical was high in order to better simulate the cirrus features. The results of their study showed that cirrus could be modeled successfully with a mesoscale model. The predictions of cloud height, thickness, cloud extent (horizontal), and the dynamics all compared well with observations from the FIRE experiment. The simulations were also able to resolve the cloud layering often associated with cirrus and cloud-top generation mechanisms. The optical thickness of the simulated cirrus was, however, underpredicted.

Chapter 3

THE RAMS MODEL

3.1 Model Description

The model used for the cirrus studies presented here is the Regional Atmospheric Modeling System (RAMS) developed at Colorado State University. The model is a mesoscale model of such diversity that many different cloud systems of varying physical characteristics may be effectively simulated with it. A general description of the model details may be found in Tripoli and Cotton (1982), Cotton et al. (1982; 1986), Tremback et al. (1985), Tripoli (1986), Tremback (1990), and Peilke et al. (1992). The version used is a two-dimensional version of the RAMS model which is ideal for the types of sensitivity studies that will be posed in Chapter 6. The version of the model used here includes a hybrid time differencing scheme for model solutions. For integration of acoustic terms occur on short time steps (while all other terms are integrated on a long time step) a time-splitting scheme is utilized.

RAMS prognoses the u , v , and w components of the wind, the ice-liquid water potential temperature (Tripoli and Cotton (1982)), perturbation Exner function, total liquid water mass mixing ratio, the mixing ratios and number concentrations (besides cloud water) of the various hydrometeor species. This version of RAMS also includes the possibility of mixed-phase hydrometeors. A more detailed explanation of this and the other new features of the RAMS microphysical module is explained in the next section. Diagnosed variables include model dry air density, temperature, potential temperature, and the mass mixing ratios of vapor and cloud water.

The grid system employed in RAMS is the standard Arakawa C-grid (Arakawa and Lamb, 1981). In this two-dimensional set-up the nested grid capabilities of RAMS are not utilized. RAMS uses a polar stereographic grid in the horizontal (not used in this study) and $\sigma - z$ terrain following coordinates in the vertical. The turbulence scheme employed is a deformation eddy viscosity described by Tripoli and Cotton (1982). A soil model developed by Tremback and Kessler (1985) that uses 11 vertical levels is used. The "wall on top" vertical boundary condition is employed in this study. A modified Rayleigh friction scheme is an option in RAMS since this "rigid-lid" causes reflections at the top boundary (Heckman, 1991); this scheme is used in this study. The Klemp and Wilhelmson (1978) lateral boundary conditions are used in the simulations. The specific grid set-up, spacing and initialization is included in the sensitivity studies presented in Chapter 6.

Radiation is an important consideration in the modeling of cirrus clouds. RAMS currently contains two possible radiative transfer schemes. The first, developed by Mahrer and Pielke (1977) includes the effects of water vapor, CO_2 and O_3 on radiative transfer. This scheme is computationally efficient, but ignores the effects of clouds. The scheme used here is one described by Chen and Cotton (1983) and includes the effects of condensate on radiative transfer. This scheme uses the total mass mixing-ratio to calculate the radiative transfer and, thus, does not differentiate between liquid water and ice, nor the size distribution of the hydrometeors.

Recently, there has been a trend in modeling (Nickerson, 1978; Ferrier, 1993; and Mitchell, 1994) towards prediction on two moments of the hydrometeor spectra, namely number concentration and mass mixing-ratio. Similar modifications for predictions on two moments of the hydrometeor spectra has been added to RAMS. This and the rest of the new RAMS microphysical package will be described in the following section.

3.2 Model Microphysics

Cirrus clouds are, as was stated above, quite a challenge to simulate with mesoscale models due to their sometimes thin vertical structure and the complexity of the ice crystals that make up their microphysical characteristics. Thus, the detail of the microphysical package employed is of great importance in the simulations of these systems. The model microphysics employed for these simulations include various improvements over old versions of the RAMS model (Cotton et al., 1982; 1986). RAMS Version 3A allows for seven water categories defined as vapor, cloud droplets, rain, pristine ice, snow, aggregates, graupel, and hail. In older versions of RAMS Marshall-Palmer or exponential-type basis functions were used to describe distributions of the various hydrometeor types, except for pristine ice which was considered monodisperse. Also, mixed phase hydrometeors were not allowed, hydrometeor collection was described by a parameterized form of the continuous collection equation, and there was only the possibility to predict on one moment of a given size distribution (the mixing-ratio). A description of the complete two-moment prediction schemes can be found in Meyers (1994).

The new version of the cloud microphysics implemented into the RAMS model (Walko et al., 1994) allows for all of the above types of water species (except for water vapor) to be described by the generalized gamma function given in Flatau et al. (1990) and Verlinde et al. (1990) as,

$$f_{gam}(D) = \frac{1}{\Gamma(\nu)}\left(\frac{D}{D_n}\right)^{\nu-1}\frac{1}{D_n}exp\left(-\frac{D}{D_n}\right), \tag{3.1}$$

where ν is the shape parameter of the distribution, $\Gamma(\nu)$ is the gamma function of ν which serves to normalize the integral of this function over $0 \rightarrow \infty$, and D_n is the characteristic diameter of the distribution which serves to non-dimensionalize the function.

Heat budget equations are formulated for the rain, graupel, and hail hydrometeor species, allowing for non-thermal equilibrium. This allows for mixed-phase hydrometeors in the cases of graupel and hail. These are formulated by noting that the temperature of any given hydrometeor can differ from that of the surrounding ambient air temperature. This temperature differential controls the rate of heat, vapor diffusion to the hydrometeors surface, and the sensible heat transferred during Collisional-coalescence processes. Sources and sinks to each category are assumed to be: (1) heat generation (loss) due to vapor depositional processes, (2) heat generation (loss) due to sensible heat diffusion, and (3) heat generation (loss) due to conversion of hydrometeors. Using a reference internal category energy of a given hydrometeor species defined for ice at T=0°C, the heat transferred when hydrometeor conversion occurs can be calculated simply. The processes of heat generation (loss) due to vapor deposition is calculated by integrating the growth equation for hydrometeors over the hydrometeor distribution. From this a change in the mixing ratio of a given hydrometeor species can be found, and, by multiplication by the latent heat (L_{lv} or L_{iv}) the heating due to vapor depositional growth is found. A similar relation is found for the heat generation (loss) due to sensible heat transfer (see Walko et al., 1994). It should be noted that in the older version of the RAMS microphysical module temperature differentials between the hydrometeor surfaces and the ambient environment were allowed, however latent heat release was assumed to be always in balance with the sensible heat transfer (i.e. diffusion).

Nucleation in the model occurs both heterogeneously and homogeneously for pristine ice crystals (nucleation of ice is discussed in more detail in the next section). Ice crystals nucleate homogeneously from haze solution droplets or supercooled cloud droplets (DeMott et al., 1994). Pristine ice, snow, and aggregates are considered completely frozen in the model. All of the hydrometeor classes have appreciable fall velocities except for cloud droplets. For growth processes, snow is allowed to grow by vapor deposition and riming while the pristine ice category only grows by vapor deposition. This is consistent with the results of Pitter (1977) and Schlamp and Pruppacher (1977) showing that small ice crystals are not affected by riming growth. Aggregates form through collisional-coalescence of pristine ice, snow, or other aggregates and is described by the stochastic collection equation. This equation is solved in general by Verlinde et al. (1990). Solutions to the general equation are calculated and placed in three dimensional look-up tables to reduce computational costs. A detailed discussion of these microphysical parameterizations is given in Walko et al. (1994).

3.3 Ice Nucleation

Ice nucleation in the model occurs through either heterogeneous or homogeneous processes. Since this initiation mechanism is of such importance in cirrus clouds, it will be helpful to give a brief discussion of the model parameterizations of these processes here.

3.3.1 Heterogeneous nucleation of ice

Fletcher (1962) parameterized deposition and condensation-freezing nucleation by an equation that predicted number as a simple exponential function of the degree of supercooling. This result seriously overpredicted the number of crystals nucleated when temperatures ranged below about $-25°C$ and underpredicted at temperatures warmer than about $-10°C$. In order to obtain better ice nucleation estimates, Cotton et al (1986) combined Fletcher's equation with Huffman et al's (1973) result that predicted on the degree of ice supersaturation to obtain the following hybrid result

$$N_{id} = N_0\{(S_i - 1)(S_0 - 1)^{-1}\}^b exp(aT_{sup}) \tag{3.2}$$

where N_{id} is the number nucleated, N_0 is a base concentration derived from experimentation, $(S_0 - 1)$ is the fractional ice supersaturation at water saturation, and T_{sup} is the degree of supercooling. This is the form of the nucleation equation that was previously used in RAMS.

By use of a conglomeration of recent laboratory ice nuclei measurements with continuous flow diffusion chambers, Meyers et al. (1992) suggested that this result is insufficient. Meyers et al. (1992), fitted the continuous flow diffusion chamber data with a simple exponential function of ice supersaturation of the form,

$$N_{id} = exp\{a + b(100(S_i - 1))\} \tag{3.3}$$

where N_{id} is the number nucleated, a and b are empirical constants of the fit (a=-0.639 and b=0.1296), and $S_i - 1$ is the supersaturation with respect to ice. The laboratory data were interpreted to represent a combination of deposition freezing, condensation-freezing, and immersion freezing. Since conditions in which these nucleation methods occur (freezing temperatures and water supersaturations) are similar, the data that the above parameterization is based on are assumed to encompass all of them.

What is needed next is a formulation for the nucleation of ice crystals through the process of contact-freezing. Unfortunately, there are not very many measurements available that have made actual attempts at isolating the freezing of drops via the contact-freezing mechanism. This makes any model parameterization of the contact-freezing process narrow in scope. Nevertheless, it is important to describe this process by some sort of parameterization that encompasses as much of the relevant data as possible.

Contact-freezing was parameterized by Young (1974) by fitting a simple function to data collected by Blanchard (1957) in a vertical wind tunnel standing in a cold aircraft hanger. The air flowing through the wind tunnel was probably not representative of normal atmospheric conditions. This fit is given by the equation,

$$N_{ic} = N_{a0}(270.16 - T_c)^{1.3} \tag{3.4}$$

where N_{ic} is the number nucleated per liter, $N_{a0} = 2.0 \times 10^2 l^{-1}$, and T_c is the cloud droplet temperature. As stated in Meyers et al (1992), however, laboratory simulations of contact nuclei using airborne membrane filter data processed in an electrostatic precipitation (Vali,1974;1976; Cooper, 1990), a thermal gradient diffusion chamber, and techniques that rely upon Brownian diffusion and phoretic forces to transport the aerosols to the surfaces of supercooled water drops (Deshler,1982) produced results that are inconsistent with Banchards (1957) data. Quantification of the contact-freezing process of heterogeneous nucleation was accomplished by finding a numerical fit to the data of Vali (1974, 1976), Cooper (1980) and Deshler (1982) and is given in Meyers et al (1992) as

$$N_{ic} = exp\{a + b(273.15 - T_c)\} \tag{3.5}$$

where a=-2.80 and b=0.262 are constants determined by the numerical fit and T_c is the degree of supercooling. This parameterization of ice nucleation is the one that we will adopt in this modeling study. It should be noted that these parameterizations are based on measurements in the lower troposphere, not at cirrus levels. There are no measurements of ice nuclei available at cirrus altitudes.

3.3.2 Homogeneous nucleation of ice

Homogeneous freezing production of ice crystals is a process that, until recently (DeMott et al., 1993), has not been considered in the microphysics of RAMS. This parameterization of the homogeneous freezing process assumes nucleation upon two separate populations; cloud droplets and haze particles. The homogeneous freezing of cloud droplets may be formulated in the following manner, following DeMott et al. (1993),

$$N_f = \int_0^\infty (1 - exp(-J_{ls} V_l \Delta t)) n(D) dD \tag{3.6}$$

where

$$J_{ls} = J_{ls0}; V_l = \frac{\pi D^3}{6}, \tag{3.7}$$

where n(D) is the distribution of cloud droplets, V_l is the volume of the drops, and J_{ls0} is the nucleation rate for pure water. In order to solve (3.6) for the number of drops frozen per time increment, a formulation for J_{ls0} is needed. This was formulated in DeMott et al (1993) by following the theoretical framework in Pruppacher and Klett (1978) for the steady state approximation of the number of embryos that pass a critical size. Comparison to Sassen and Dodd's (1988) numerical calculations coupled with aircraft measurements and with the results of DeMott and Rodgers (1988) showed that the theoretical description given by (3.6) was sufficient. What is needed for a parameterization in a cloud model, however, is a formulation of the nucleation process that is a simple function of temperature and saturation. Heymsfield and Sabin (1989) used the temperature dependent formulation given by Eadie (1971),

$$J_{ls0} = 10^y \tag{3.8}$$

with

$$y = -606.3952 - (52.6611 T_c) - (1.7439 T_c^2) - (0.0265 T_c^3) - (1.536E - 4 T_c^4). \tag{3.9}$$

Both this parameterization and the result given by (3.6) gain support from the above experimental results and from Eadie's results. Eadie's results, however tend to be higher at the lower end of the temperature range. This is better represented by the parameterization of Heymsfield and Sabin (1989). For these reasons, (3.8) is used to parameterize the homogeneous freezing of cloud droplets in the model.

The homogeneous freezing of haze solution drops is a little more difficult to approach theoretically, however a parameterization is still possible. DeMott et al. (1993) derive a freezing rate for haze solution droplets by considering changes to the nucleation rate, J_{ls}, in (3.6) ; such as addition of a water activity term and a term for the additional depression of the freezing temperature due to nonideal ionic interactions. The Kohler curves were used to obtain values for other needed values such as the solution drop size, D_s, the solution density, ρ_l'', and the molality, M. Using these results, a theoretical expression for the freezing rate of haze solution drops was obtained. A simple parameterization of this result was obtained that fit the theoretical solutions reasonable well. This is given by the following result,

$$F_{hf} = 1 - exp(-aD_s^b), \tag{3.10}$$

where

$$a = c1(\pi\rho_s)^2(S_w)^{c2}; andb = 5 \tag{3.11}$$

$$c1 = 0.0277exp(-23.3 - (2.12(T_l - 273.16))) \tag{3.12}$$

$$c2 = 4910 + 179.6(T_l - 273.16) + 1.8(T_l - 273.16)^2. \tag{3.13}$$

Using this result it is then easy to write down an expression for the the number of haze solution droplets freezing per time increment. This is given by,

$$N_f = N_t \int_0^{y_{max}} exp(-y)\left\{1 - exp\left(-y^b\left(\frac{D_n}{D_m}\right)^b\right)\right\}dy \tag{3.14}$$

where

$$y = \frac{D}{D_n}. \tag{3.15}$$

This equation is solved numerically in the model and tables are made of the nucleation rates for various temperatures. Again, it should be noted that there are very few measurements of upper tropospheric haze and CCN concentrations. Projects like FIRE II have introduced new data such as Levinson et al. (1993) who describes measurements of lidar observations of aerosols from the Mount Pinatubo eruption in June of 1991. These stratospheric aerosols can enter the troposphere through tropospheric folding events and may effect ice nucleation in cirrus clouds.

3.4 Two-Moment Predictions

It has usually been the case with bulk models of the recent past, such as older versions of the RAMS model (Cotton et al., 1986), to follow a framework in which only mass moment predictions of the hydrometeor spectra were used. In these schemes, mass mixing ratio is computed while either the mean diameter or intercept parameter is set by the user. Then, the unknown variable is diagnosed from the prognostic variable and the user defined variable. Some recent and bulk models (e.g. Nickerson et al., 1978; Zeigler, 1987; and Ferrier, 1993) have gone to predictive equations using two moments of the particle distributions; namely number concentration and mass mixing ratio. In RAMS the model parameterizations include number predictions for graupel and hail that include number concentration loss due to melting and sublimation, number concentration sources and sinks due to collision and coalescence and precipitation processes, and predictions of the number concentration and mass transfers between the pristine ice and snow classes. These schemes are discussed in detail in Meyers et al. (1994). The parameterization of the number concentration and mass mixing ratio transfers for pristine ice and snow are described in the next chapter along with the general parameterization of evaporative number concentration loss. This evaporative loss scheme is extended by Meyers et al. (1994) to take into account the melting loss of graupel and hail.

Chapter 4

THE BIMODAL ICE SPECTRA

The parameterization of ice species in mesoscale models has always been risky, especially when it comes to upper tropospheric clouds such as cirrus. The main reason for this is that not many significant measurements of ice at those atmospheric heights have been obtained (Meyers et al., 1991). Recent evidence, as discussed previously, has suggested a bimodal ice spectra in cirrus clouds which consists of large numbers of small ice crystals (Arnott et al., 1993; Hein et al.,1993, Intrieri et al., 1993; and Matrosov et al., 1993). Because of this, the new RAMS microphysics contains two ice classes, pristine ice and snow, which are differentiated by a "cut-off" diameter, D_b. Each ice class is described by a separate, complete gamma distribution function with fluxes of crystals between each class dependent upon the ambient saturation with respect to ice. The addition of the spectra need not be bimodal, the representation given here allows for a single mode if the model physics so dictates. The equations that describe the mass mixing-ratio and number concentration flux between the ice classes is developed below.

4.1 Theoretical Development

This section describes a parameterization that predicts the flux of concentration and mass from a pristine ice category to a snow category. Both pristine ice and snow are described by separate gamma distributions. Crystals of either type are allowed to transfer between the distributions depending on the ambient saturation with respect to ice. The flux equations are developed with the assumption that there is some critical diameter D_b that is the boundary between the pristine ice and snow classes. Equations are then developed which describe the transfer of concentration and mass between the distributions due solely to vapor deposition or evaporation.

We first describe the relevant equations that will be used in the development of the flux model. These are given by,

$$N_t = \int_0^\infty n(D)dD, \tag{4.1}$$

where

$$n(D) = \frac{N_t}{\Gamma(\nu)}(\frac{D}{D_n})^{(\nu-1)}\frac{1}{D_n}exp(\frac{-D}{D_n}). \tag{4.2}$$

Also,

$$\bar{r}_i = \bar{r}_s = \frac{1}{\rho_a}\int_0^\infty m(D)n(D)dD \tag{4.3}$$

where $D = D(t)$ for simplicity and N_t is the total number concentration of ice particles. By using a mass-dimensional relationship such as that given by Mitchell et al. (1989) in Equation (2.1), we may solve the above integral in terms of the complete gamma function. Rearranging this expression gives a result for the characteristic diameter, D_n as

$$D_n = \left\{\frac{\bar{r}_{i,s}}{N_t}\frac{\rho_a}{\alpha}\frac{\Gamma(\nu)}{\Gamma(\nu+\beta)}\right\}^{1/\beta}. \tag{4.4}$$

The rate of mass growth of a single ice crystal by vapor deposition (sublimation) is

$$\frac{dm}{dt} = 4\pi(C_i)(S_i - 1)G_i(T,P) \tag{4.5}$$

$$G_i(T,P) = \left\{\left(\frac{L_s}{R_vT} - 1\right)\frac{L_s}{KT} + \frac{R_vT}{e_i(T)D_v}\right\}^{-1}. \tag{4.6}$$

In the discussion of the parameterization it is necessary to delineate between the pristine ice and snow distributions. To do this we will adopt a general policy of subscripting the distribution and it's various parameters with either a i for pristine ice or s for snow. This also allows for a more general solution.

4.1.1 Crystal Capacitance

When the integrals (4.1) and (4.3) are used to develop the flux representation, it is necessary to write the capacitance term in Equation (4.5) in such a way that the integration does not have to include both terms (the major and the minor dimensions). In order to do this it is possible to write the capacitance as a function of its aspect ratio, A, and its major dimension, which we will for now delineate as c:

$$C_i = f(c, a) = g(c, A) \tag{4.7}$$

$$C_i = \chi D \text{ where } \chi = \chi(A). \tag{4.8}$$

The aspect ratio in the capacitance term is held constant only during the integration so that analytical solutions are attainable. In order to vary the model aspect ratio, the mass-diameter relationship is related to the equivalent volume of the crystal. For needles, long and short columns this may be written,

$$m(D) = \alpha' D^{\beta_m} = \alpha' c^{\beta_m} = \rho_i V = \rho_i \left(\frac{a}{2}\right)^2 c\pi, \tag{4.9}$$

where c is the crystal major axis and a is the minor axis. Solving for a yields,

$$a = Z^{1/2} c^{(\beta-1)/2} \text{ where } Z = \frac{4\alpha'}{\pi \rho_i}. \tag{4.10}$$

For hexagonal plates we may write

$$\alpha' c^{\beta_m} = \rho_i \left(\frac{c}{2}\right)^2 a\pi. \tag{4.11}$$

Thus, the equation for a is,

$$a = Zc^{\beta-2}. \tag{4.12}$$

Growth of crystals is assumed to occur along the major dimension, c, and the aspect ratio is changed by using the above equations for a. Note that this type of analysis is not needed for thin plates and dendrites whose capacitance term is D/π; thus a major and minor axis do not enter the picture.

4.1.2 Development of the Flux Equations

Development of a bimodal description of ice in upper level clouds has its foundations in some very basic concepts and in some observational evidence, as was stated above. Motivated by these recent studies which suggest a bimodal ice crystal spectrum in cirrus clouds, a bimodal representation of the ice crystal spectrum was developed using the gamma function given by Equation (4.2). Figure 4.1 shows a schematic of the distributions with a certain diameter, D_b, set as a threshold between the pristine ice crystal and snow categories. The data of Arnott et al. (1993) suggests that a value of D_b of 125 μm is reasonable. There is some overlap of each distribution, however, this is usually insignificant artifact of the complete distribution representation. To remove this artifact, truncated distributions would be required. Solutions of this type, however, would increase the model time (and therefore cost) of the simulations.

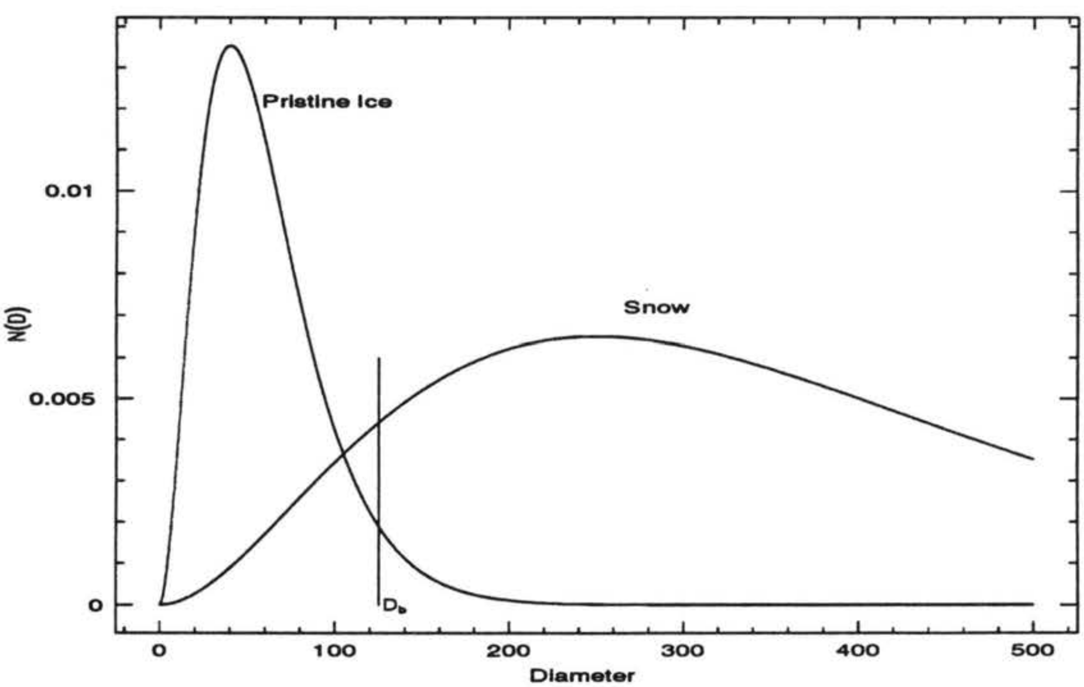

Figure 4.1: Example of the bimodal representation: Fluxes are assumed to occur across a boundary at $D_b = 125\mu m$

Following are the equations developed for the flux of crystals across the boundary, D_b, along with an equation for the mass growth and evaporation of the distribution. This is all accomplished by differentiating Equations (4.1) and (4.3) and using the vapor depositional growth equation given by (4.5). For the total vapor depositional growth rate of the distributions we may write:

$$\dot{r} = \frac{d}{dt}\frac{1}{\rho_a}\int_0^\infty m(D)n(D)dD. \tag{4.13}$$

This is written in the general case, and can be expanded to two distributions by including the subscripts i for pristine ice and s for snow as was stated above.

The flux equations are developed by considering the spectral shift due to the gain of mass given by (4.13). For the fluxes of pristine ice to the snow category the shift in the pristine ice distribution beyond the boundary ,D_b, needs to be considered. This shift in number concentration and mass-mixing ratio may be written as,

$$\dot{r}_i^f = \frac{d}{dt}\frac{1}{\rho_a}\int_{D_b}^\infty m(D)n_i(D)dD \tag{4.14}$$

$$\dot{N}_i^f(D) = \frac{d}{dt}\int_{D_b}^\infty n_i(D)dD. \tag{4.15}$$

Equation (4.14) describes the rate of change of mass in the region from $D_b \rightarrow \infty$ of the pristine ice distribution and (4.15) the rate of change of number concentration. This is exactly the amount due to the growth of crystals beyond the boundary.

For the subsaturated case, when snow is being converted to pristine ice, formulations similar to (4.14) and (4.15) are derived as

$$\dot{r}_s^f = \frac{d}{dt}\frac{1}{\rho_a}\int_0^{D_b} m(D)n_s(D)dD \tag{4.16}$$

$$\dot{N}_s^f(D) = \frac{d}{dt}\int_0^{D_b} n_s(D)dD. \tag{4.17}$$

To solve these equations we will recast them in a more physically digestible form, starting by using Leibniz' rule to rewrite (4.13) through (4.17) as,

$$\dot{r} = \frac{1}{\rho_a}\int_0^\infty \left(\frac{\partial m(D)}{\partial t}n(D) + m(D)\frac{\partial n(D)}{\partial t}\right) dD \tag{4.18}$$

$$\dot{r}_i^f = \frac{1}{\rho_a}\int_{D_b}^\infty \frac{\partial}{\partial t}\left\{m(D)n_i(D)\right\} dD - m(D_b)n_i(D_b)\frac{\partial D_b}{\partial t} \tag{4.19}$$

$$\dot{N}_i(D) = \int_{D_b}^\infty \frac{\partial n_i(D)}{\partial t} dD - n_i(D_b)\frac{\partial D_b}{\partial t} \tag{4.20}$$

$$\dot{r}_s^f = \frac{1}{\rho_a}\int_0^{D_b} \frac{\partial}{\partial t}\left\{m(D)n_s(D)\right\} dD + m(D_b)n_s(D_b)\frac{\partial D_b}{\partial t} \tag{4.21}$$

$$\dot{N}_s(D) = \int_0^{D_b} \frac{\partial n_s(D)}{\partial t} dD + n_s(D_b)\frac{\partial D_b}{\partial t}. \tag{4.22}$$

Since D_b is not a function of time, all of the $\partial D_b/\partial t$ terms are zero. Equations (4.19) and (4.21) can then be written by expanding the derivatives as,

$$\dot{r}_i^f = \frac{1}{\rho_a}\int_{D_b}^{\infty}\left(n_i(D)\frac{\partial m(D)}{\partial t} + m(D)\frac{\partial n_i(D)}{\partial t}\right)dD \tag{4.23}$$

$$\dot{r}_s^f = \frac{1}{\rho_a}\int_0^{D_b}\left(n_s(D)\frac{\partial m(D)}{\partial t} + m(D)\frac{\partial n_s(D)}{\partial t}\right)dD. \tag{4.24}$$

In these equations, the derivatives are all from a Eulerian framework (since we are looking at this problem from a distribution-relative point of view). In this framework, $\partial m(D)/\partial t$ is zero because we are sitting at points on the distribution and asking questions about how particles are growing. At any given diameter the mass per particle *at that point* is not changing because the diameter is not changing. Thus, our equation system becomes,

$$\dot{r} = \frac{1}{\rho_a}\int_0^{\infty} m(D)\frac{\partial n(D)}{\partial t}dD \tag{4.25}$$

$$\dot{r}_i^f = \frac{1}{\rho_a}\int_{D_b}^{\infty} m(D)\frac{\partial n_i(D)}{\partial t}dD \tag{4.26}$$

$$\dot{N}_i^f = \int_{D_b}^{\infty} \frac{\partial n_i(D)}{\partial t}dD \tag{4.27}$$

$$\dot{r}_s^f = \frac{1}{\rho_a}\int_0^{D_b} m(D)\frac{\partial n_s(D)}{\partial t}dD \tag{4.28}$$

$$\dot{N}_s^f = \int_0^{D_b} \frac{\partial n_s(D)}{\partial t}dD. \tag{4.29}$$

By invoking a result from Berry (1965) these equations can be written in a form that is more physically understandable. For vapor depositional growth we may write,

$$\frac{\partial n(D)}{\partial t} = -\frac{\partial}{\partial D}\left\{\frac{dD}{dt}n(D)\right\}. \tag{4.30}$$

Using this result in the above equations gives

$$\dot{r} = -\frac{1}{\rho_a}\int_0^{\infty} m(D)\frac{\partial}{\partial D}\left\{\frac{dD}{dt}n(D)\right\}dD \tag{4.31}$$

$$\dot{r}_i^f = -\frac{1}{\rho_a}\int_{D_b}^{\infty} m(D)\frac{\partial}{\partial D}\left\{\frac{dD}{dt}n_i(D)\right\}dD \tag{4.32}$$

$$\dot{N}_i^f = -\int_{D_b}^{\infty} \frac{\partial}{\partial D}\left\{\frac{dD}{dt}n_i(D)\right\}dD \tag{4.33}$$

$$\dot{r}_s^f = -\frac{1}{\rho_a}\int_0^{D_b} m(D)\frac{\partial}{\partial D}\left\{\frac{dD}{dt}n_s(D)\right\}dD \tag{4.34}$$

$$\dot{N}_s^f = -\int_0^{D_b}\frac{\partial}{\partial D}\left\{\frac{dD}{dt}n_s(D)\right\}dD. \tag{4.35}$$

In finding solutions to the above equations the following hierarchy will be adhered to: first, Equation (4.31) will be rewritten in a form which is easier to talk about physically, then the resulting equation will be solved. Second, we will rewrite and solve Equations (4.32) and (4.33). Finally, the results for (4.34) and (4.35) will simply be written down since obvious similarities exist between Equations (4.32), (4.33), (4.34) and (4.35).

The integrand of Equation (4.31) may be written in the following form,

$$m(D)\frac{\partial}{\partial D}\left\{\frac{dD}{dt}n(D)\right\} = \frac{\partial}{\partial D}\left\{m(D)\frac{dD}{dt}n(D)\right\} - \frac{\partial m(D)}{\partial D}\frac{dD}{dt}n(D). \tag{4.36}$$

Substitution of this result into Equation (4.31) gives

$$\dot{r} = -\frac{1}{\rho_a}\int_0^{\infty}\left\{\frac{\partial}{\partial D}\left(m(D)\frac{dD}{dt}n(D)\right) - \frac{\partial m(D)}{\partial D}\frac{dD}{dt}n(D)\right\}dD. \tag{4.37}$$

In order to evaluate the terms in this expression it is necessary to break this integral into two parts. Since it is an improper integral, however, it is necessary to show that each term of the integrand converges separately and, therefore, that the two independent integrals may be written in the following manner,

$$\begin{aligned}
&-\frac{1}{\rho_a}\left(\int_0^{\infty}\frac{\partial}{\partial D}\left(m(D)\frac{dD}{dt}n(D)\right)dD - \int_0^{\infty}\frac{\partial m(D)}{\partial D}\frac{dD}{dt}n(D)dD\right)\\
&\quad = -\frac{1}{\rho_a}\int_0^{\infty}\left\{\frac{\partial}{\partial D}\left(m(D)\frac{dD}{dt}n(D)\right) - \frac{\partial m(D)}{\partial D}\frac{dD}{dt}n(D)\right\}dD.
\end{aligned} \tag{4.38}$$

To prove this, each term will be examined and shown to converge. The first term on the right hand side can be written

$$\begin{aligned}
A &\equiv \int_0^{\infty}\frac{\partial}{\partial D}\left\{m(D)\frac{dD}{dt}n(D)\right\}dD\\
&= lim_{x\to\infty}\left\{m(x)\frac{dD}{dt}\mid_x n(x)\right\} - m(D=0)\frac{dD}{dt}\mid_{D=0} n(D=0).
\end{aligned} \tag{4.39}$$

The second term on the right hand side of this expression is clearly zero. It is not obvious, however, that the first term on the right hand side converges. In order to see this, let us write out the entire expression for the limit. First, we will need an expression for the mass of an individual crystal. This is given by an empirical expression from Mitchell et al. (1989)

$$m(D) = \alpha D^{\beta}. \tag{4.40}$$

For dD/dt let us first write Equation (4.5) as

$$\frac{dm}{dt} = \Psi D \tag{4.41}$$

where

$$\Psi = 4\pi\chi(S_i - 1)G_i(T,P). \tag{4.42}$$

Now, using the definition of crystal mass as given above we may write

$$\frac{dD}{dt} = \frac{\Psi}{\alpha\beta}D^{2-\beta}, \tag{4.43}$$

or

$$\frac{dD}{dt} = \Phi D^{2-\beta} \text{ where } \Phi = \frac{\Psi}{\alpha\beta}. \tag{4.44}$$

In light of these equations the limit becomes,

$$lim_{x\to\infty}\left\{\alpha x^{\beta}\Phi x^{2-\beta}\frac{N_t}{\Gamma(\nu)}\left(\frac{x}{D_n}\right)^{\nu-1}\frac{1}{D_n}exp\left(-\frac{x}{D_n}\right)\right\}. \tag{4.45}$$

Rewriting this gives,

$$lim_{x\to\infty}\left\{\alpha\Phi D_n\frac{N_t}{\Gamma(\nu)}\left(\frac{x}{D_n}\right)^{\nu+1}exp\left(-\frac{x}{D_n}\right)\right\}\to 0. \tag{4.46}$$

From this expression it is easy to see that the exponential term will dominate in the limit. Thus, this term will go to zero as x approaches infinity and the first term on the right hand side of (4.37) goes to zero. The second term in (4.37) is,

$$B \equiv \frac{1}{\rho_a}\int_0^{\infty}\frac{\partial m(D)}{\partial D}\frac{dD}{dt}n(D)dD. \tag{4.47}$$

Recall that if we have,

$$\frac{dm}{dt} = \frac{d\alpha D^{\beta}}{dt}, \tag{4.48}$$

we can write,

$$\frac{dm}{dt} = \alpha\beta D^{\beta-1}\frac{dD}{dt} \text{ or } \frac{dm}{dt} = \frac{\partial m(D)}{\partial D}\frac{dD}{dt}. \tag{4.49}$$

So, we may write (4.47) as,

$$B = \dot{r} = \frac{1}{\rho_a}\int_0^\infty \frac{dm}{dt}n(D)dD = \frac{\Psi}{\rho_a}\int_0^\infty Dn(D)dD. \tag{4.50}$$

Equation (4.50) converges since it is just a description of the complete gamma function. B converges for all $R(\nu+1) > 0$. Therefore it is possible for (4.37) to be written as the two separate terms, A and B. As we have seen, A goes to zero in the limit which leaves (4.50) as the final form of the equation for $\dot{r}$.

This equation is easy to interpret. It shows that the amount of mass gained or lost by the distribution is calculated by considering the growth/evaporation of a single crystal and then summing over the entire distribution. This is definitely easier to see in this version of the equation than in the previous version, (4.25).

To solve the integral in (4.50) let us write out the expressions for dm/dt and n(D) in the integral,

$$\dot{r} = \int_0^\infty \Psi D\frac{N_t}{\Gamma(\nu)}\left(\frac{D}{D_n}\right)^{\nu-1}\frac{1}{D_n}exp\left(-\frac{D}{D_n}\right)dD. \tag{4.51}$$

Changing variables from D to D_y where $D_y = D/D_n$ gives

$$\dot{r} = \frac{\Psi}{\rho_a}D_n\frac{N_t}{\Gamma(\nu)}\int_0^\infty D_y^{(\nu+1)-1}exp(-D_y)dD_y. \tag{4.52}$$

Noting that the complete gamma function is defined by

$$\Gamma(n) = \int_0^\infty X^{n-1}exp(-X)dX, \tag{4.53}$$

we may write (4.52) as

$$\dot{r} = \frac{\Psi}{\rho_a}D_n\frac{N_t}{\Gamma(\nu)}\Gamma(\nu+1). \tag{4.54}$$

Since a moments representation of these solutions tends to be more mathematically elegant, Equation (4.54) will be written in terms of the moments of the distribution function. First off, the moments of the complete distribution can be described by the following relation,

$$I(P) = \int_0^\infty D^P n(D)dD. \tag{4.55}$$

If the above definition of n(D) is used then the moments of the complete distribution can be written as,

$$I(P) = D_n^P \frac{N_t}{\Gamma(\nu)} \Gamma(\nu + P). \tag{4.56}$$

So, Equation (4.54) when written in terms of the moments of the complete distribution function is

$$\dot{r} = \frac{\Psi}{\rho_a} I(1). \tag{4.57}$$

Equations (4.32) and (4.33) can be solved in a similar manner to that used to solve (4.31). Starting with (4.32) we may write,

$$\dot{r}_i^f = -\frac{1}{\rho_a} \int_{D_b}^{\infty} \left\{ \frac{\partial}{\partial D} \left(m(D) \frac{dD}{dt} n_i(D) \right) - \frac{\partial m(D)}{\partial D} \frac{dD}{dt} n_i(D) \right\} dD. \tag{4.58}$$

The first term on the right hand side can be written,

$$\begin{aligned} \int_{D_b}^{\infty} \frac{\partial}{\partial D} \left(m(D) \frac{dD}{dt} n_i(D) \right) dD &= lim_{x \to \infty} \left\{ m(x) \frac{dD}{dt} \mid_{D=x} n_i(x) \right\} \\ &\quad - m(D_b) \frac{dD}{dt} \mid_{D=D_b} n_i(D_b). \end{aligned} \tag{4.59}$$

The limit above (as shown earlier) goes to zero. Substituting into equation (4.58) and rewriting the second term on the right hand side of (4.58) gives,

$$\dot{r}_i^f = \frac{1}{\rho_a} m(D_b) \frac{dD}{dt} \mid_{D=D_b} n_i(D_b) + \frac{1}{\rho_a} \int_{D_b}^{\infty} \frac{dm}{dt} n_i(D) dD. \tag{4.60}$$

Equation (4.60) describes the flux of mass from distribution i to distribution s across the boundary D_b. This equation is easily interpreted from a physical perspective. The first term on the right hand side of (4.60) describes the amount of mass shifted across the boundary, D_b, due to vapor depositional growth. The second term describes the gain of mass of crystals in the $D_b \to \infty$ range due to vapor depositional growth. It may seem that only the first term is required in order to describe the flux process, however, ignoring the second term can lead to some errors. Remember that the description of pristine ice is through the use of complete distributions. Therefore, if only the first term is included then, the tail of the distribution will continue to grow. Now, the crystals in this tail regime are really in the snow category (since D_b delineates categories) but, as long as the tail is a small percentage of the mass it contributes little. The second term in (4.60) causes this tail to grow larger, and after a long enough period, the tail can contain a significant portion of the distribution mass. Therefore, we choose to keep the second term in (4.60) as part of the flux description.

To solve this equation let us start with the first term on the right hand side of equation (4.60). Substitution of equations (4.40), (4.44) and (4.2) gives

$$\frac{1}{\rho_a} m(D_b) \frac{dD}{dt} \mid_{D=D_b} n_i(D_b) = \frac{1}{\rho_a} \alpha D_b^{\beta} \Phi D_b^{2-\beta} \frac{N_{t;i}}{\Gamma(\nu)} \left(\frac{D_b}{D_{n;i}}\right) \frac{1}{D_{n;i}} exp\left(-\frac{D_b}{D_{n;i}}\right). \quad (4.61)$$

Or for simplicity,

$$m(D_b) \frac{dD}{dt} \mid_{D=D_b} n_i(D_b) = \frac{\Phi}{\rho_a} \alpha D_b^2 n_i(D_b). \quad (4.62)$$

The second term on the right hand side of Equation (4.60) can be written by the use of Equations (4.41) and (4.2) as

$$\frac{1}{\rho_a} \int_{D_b}^{\infty} \frac{dm}{dt} n_i(D_b) dD = \frac{1}{\rho_a} \int_{D_b}^{\infty} \Psi D \frac{N_{t;i}}{\Gamma(\nu)} \left(\frac{D}{D_{n;i}}\right) \frac{1}{D_{n;i}} exp\left(-\frac{D}{D_{n;i}}\right) dD. \quad (4.63)$$

Changing variables from D to D_y again gives,

$$\frac{1}{\rho_a} \int_{D_b}^{\infty} \frac{dm}{dt} n_i(D_b) dD = \frac{\Psi}{\rho_a} D_{n;i} \frac{N_{t;i}}{\Gamma(\nu)} \int_{D_b}^{\infty} D_y^{(\nu+1)-1} exp(-D_y) dD_y. \quad (4.64)$$

The solution to this integral is given in Ambromowitz and Stegun (1972) as the incomplete gamma function defined by,

$$\Gamma(n, Y) = \int_{Y}^{\infty} X^{n-1} exp(-X) dX. \quad (4.65)$$

For completeness, let us also write down the solution for the integral from 0 to Y. This is given as,

$$\gamma(n, Y) = \int_{0}^{Y} X^{n-1} exp(-X) dX. \quad (4.66)$$

Using the above definition of the incomplete gamma function we may write,

$$\frac{1}{\rho_a} \int_{D_b}^{\infty} \frac{dm}{dt} n_i(D_b) dD = \frac{\Psi}{\rho_a} D_{n;i} \frac{N_{t;i}}{\Gamma(\nu)} \Gamma(\nu+1, D_b/D_{n;i}). \quad (4.67)$$

As before, Equation (4.67) will be written in terms of the moments of the distribution functions. For an incomplete distribution, the moments may be defined as,

$$T(P) = \int_{X}^{\infty} D^P n(D) dD \quad (4.68)$$

$$T(P) = D_n^P \frac{N_t}{\Gamma(\nu)} \Gamma(\nu + P, X/D_n). \tag{4.69}$$

For the integral from 0 to X,

$$U(P) = \int_0^X D^P n(D) dD \tag{4.70}$$

$$U(P) = D_n^P \frac{N_t}{\Gamma(\nu)} \gamma(\nu + P, X/D_n). \tag{4.71}$$

Using these definitions of the moments of the incomplete gamma functions we may write (4.67) in the form,

$$\frac{1}{\rho_a} \int_{D_b}^{\infty} \frac{dm}{dt} n_i(D_b) dD = \frac{\Psi}{\rho_a} T_i(1). \tag{4.72}$$

Substitution of Equations (4.62) and (4.72) into (4.60) gives our mass flux equation as,

$$\dot{r}_i^f = \frac{\Phi}{\rho_a} Co\alpha D_b^2 n(D_b) + \frac{\Psi}{\rho_a} T_i(1). \tag{4.73}$$

In order to complete the description of crystal fluxes from i to distribution s , (4.33) needs to be solved in order to determine the concentration flux from distribution i to distribution s . Following procedures similar to the above derivations (4.33) is written in the following form,

$$\dot{N}_i^f = -\int_{D_b}^{\infty} \frac{\partial}{\partial D} \left(\frac{dD}{dt} n_i(D) \right) dD \tag{4.74}$$

$$\dot{N}_i^f = -lim_{x \to \infty} \left\{ \frac{dD}{dt} \,|_{D=x}\, n_i(x,t) \right\} + \frac{dD}{dt} \,|_{D=D_b}\, n_i(D_b). \tag{4.75}$$

The first term on the right hand side of (4.75) is zero in the limit, so (4.75) becomes

$$\dot{N}_i^f = \frac{dD}{dt} \,|_{D=D_b}\, n_i(D_b). \tag{4.76}$$

Again, the initial equation reduces to one that is simple to interpret on a physical level. Equation (4.76) is a statement of the number concentration that has crossed the boundary, D_b, due to the spectral shift.

As a final step in the derivation of this equation, let's substitute (4.44) into (4.76); this gives,

$$\dot{N}_i^f = \Phi D^{2-\beta} n_i(D_b). \tag{4.77}$$

Equations (4.73) and (4.77) are the description of concentration and mass flux from distribution i to s .

In subsaturated conditions, fluxes will occur from the snow distribution to the pristine ice distribution. In order to describe this process, it is necessary to solve equations (4.34) and (4.35). Just by examining these equations and the definitions of the incomplete gamma functions, it is possible to immediately write down the solutions to these equations. These solutions are,

$$\dot{r}_s^f = -\frac{1}{\rho_a}m(D_b)\frac{dD}{dt}\mid_{D=D_b} n_s(D_b) + \frac{1}{\rho_a}\int_0^{D_b}\frac{dm}{dt}n_s(D)dD \tag{4.78}$$

$$\dot{r}_s^f = -\frac{\Phi}{\rho_a}\alpha D_b^2 n(D_b) + \frac{\Psi}{\rho_a}D_{n;s}\frac{N_{t;s}}{\Gamma(\nu)}\gamma(\nu+1, D_b/D_{n;s}) \tag{4.79}$$

$$\dot{r}_s^f = -\frac{\Phi}{\rho_a}\alpha D_b^2 n(D_b) + \frac{\Psi}{\rho_a}U_s(1) \tag{4.80}$$

$$\dot{N}_s^f = -\int_0^{D_b}\frac{\partial}{\partial D}\left(\frac{dD}{dt}n(D)\right)dD \tag{4.81}$$

$$\dot{N}_s^f = -\frac{dD}{dt}\mid_{D=D_b} n_s(D_b) \tag{4.82}$$

$$\dot{N}_s^f = -\Phi D_b^{2-\beta}n_s(D_b). \tag{4.83}$$

Equations (4.80) and (4.83) are solutions for fluxes from the snow to the pristine ice distribution for sublimating ice crystals. However, the second term in (4.78) (and (4.80)) will be dropped. In order to see why, consider (4.78). The first term on the right hand side describes the mass-mixing ratio amount that crosses the D_b boundary due to the spectral shift (it is positive because $\partial D/\partial t < 0$). The second term describes the mass loss in the tail due to the evaporative process. Equation (4.78) is a statement of the mass change in the region of from $0 \rightarrow D_b$, so, at times the second term can overpower the first when mass loss due to evaporation in the region $0 \rightarrow D_b$ is large enough. Also, the second term describes a reclassification of the ice as vapor. To include the term in the flux equations, then, would make no physical sense. For this reason we choose to drop the second term in (4.78) through (4.80).

This may seem a little inconsistent with the mass-mixing ratio flux equation for PI to snow transfer. Remember, however, that the extra term was kept there because of the possibility of extraneously large tail growth. Also, in that case (the case of vapor deposition), the extra term described mass going *from vapor to ice* , so that at the very least the term was physically consistent.

As a summary of the flux model, let us write out our final equations. For mass growth of a complete distribution,

$$\dot{r} = \int_0^\infty \frac{dm}{dt} n(D) dD \tag{4.84}$$

$$\dot{r} = \frac{\Psi}{\rho_a} I(1). \tag{4.85}$$

For the mass and number flux form distribution i to s in a supersaturated regime,

$$\dot{r}_i^f = \frac{1}{\rho_a} m(D_b) \frac{dD}{dt} \mid_{D=D_b} n_i(D_b) + \frac{1}{\rho_a} \int_{D_b}^\infty \frac{dm}{dt} n_i(D) dD, \tag{4.86}$$

or

$$\dot{r}_i^f = \frac{\Phi}{\rho_a} \alpha D_b^2 n(D_b) + \frac{\Psi}{\rho_a} T_I(1), \tag{4.87}$$

and

$$\dot{N}_i^f = \frac{dD}{dt} \mid_{D=D_b} n(D_b), \tag{4.88}$$

or

$$\dot{N}_i^f = \Phi D_b^{2-\beta} n(D_b). \tag{4.89}$$

The mass mixing-ratio and number concentration flux from distribution s to i in a subsaturated regime is given by,

$$\dot{r}_s^f = -\frac{1}{\rho_a} m(D_b) \frac{dD}{dt} \mid_{D=D_b} n_s(D_b), \tag{4.90}$$

or

$$\dot{r}_s^f = -\frac{\Phi}{\rho_a} Co \alpha D_b^2 n(D_b), \tag{4.91}$$

and

$$\dot{N}_s^f = -\int_0^{D_b} \frac{\partial}{\partial D} \left(\frac{dD}{dt} n(D) \right) dD, \tag{4.92}$$

or

$$\dot{N}_s^f = -\Phi D_b^{2-\beta} n_s(D_b). \tag{4.93}$$

These equations are a description of flux during the growth/evaporative processes in the cloud environment. In order to complete the model, we need a way of finding number concentration loss from the pristine ice and snow distributions during evaporation. We will consider sublimation loss of any given ice category (e.g. pristine ice, snow, hail, aggregates, graupel) in the next section.

4.2 Loss of Ice Species by Sublimation

A parameterization of the process of sublimation loss of concentration from the pristine ice distribution is considered in this section. What is needed is a way to describe the loss of concentration from a given distribution of ice using as few dependent parameters as possible. One way to approach this problem is to find the size of crystal that will completely disassociate into vapor in a given model time-step by sublimation. This can be done by using (4.44) in integral form given by,

$$\int_{D_{evap}}^{0} D^{\beta-2} dD = \int_{t}^{t+\Delta t} 4\pi\chi(A)(S_i - 1)G_i(T,P)dt = 4\pi\chi(A)(S_i - 1)G_i(T,P)\Delta t, \quad (4.94)$$

where $\chi(A)$, S_i and $G_i(T,P)$ must be assumed constant over the given time-step. This gives D_{evap} as

$$D_{evap} = \{4\pi\chi(A)(S_i - 1)G(T,P)(\beta - 1)\Delta t\}^{1/(\beta-1)}. \quad (4.95)$$

The number concentration lost during a given time-step can then by found by integrating the following,

$$N_{loss} = \int_{0}^{D_{evap}} n(D)dD = N_t \frac{\gamma(\nu, D_{evap}/D_n)}{\Gamma(\nu)}. \quad (4.96)$$

Although this result is useful, it unfortunately requires the calculation of the incomplete gamma function at every time-step, which is computationally expensive. We could opt to create tables of these functions as is done for the incomplete gamma functions given in the section above; these tables would be three dimensional and be of the form,

$$\gamma(\nu, D_{evap}/D_n) = F(\nu, D_{evap}, D_n). \quad (4.97)$$

This table would have to range over values of D_{evap} and D_n from about 1 to 500 micrometers. Since this table would be quite large, we opt for a different method for the parameterization of number concentration loss by sublimation. The following parameterization is based on the idea that the ratio of mass lost from the distribution to the total mass (defined as $\dot{r}\Delta t/r_{tot}$) is related to the ratio of the concentration loss to the total concentration ($\dot{n}\Delta t/n_{tot}$).

Development of the parameterization is done from the perspective of a bin model. Since exact equations which describe the loss of concentration are not known, the parameterization is developed here as a table of percent concentration loss versus various important physical parameters.

To develop the scheme, the situation will be considered in which all physical parameters are held constant and the crystals in the distribution are slowly allowed to sublimate. Then, the relevance of certain physical parameters (such as temperature and pressure) will be examined by relaxing the conditions and allowing them to vary.

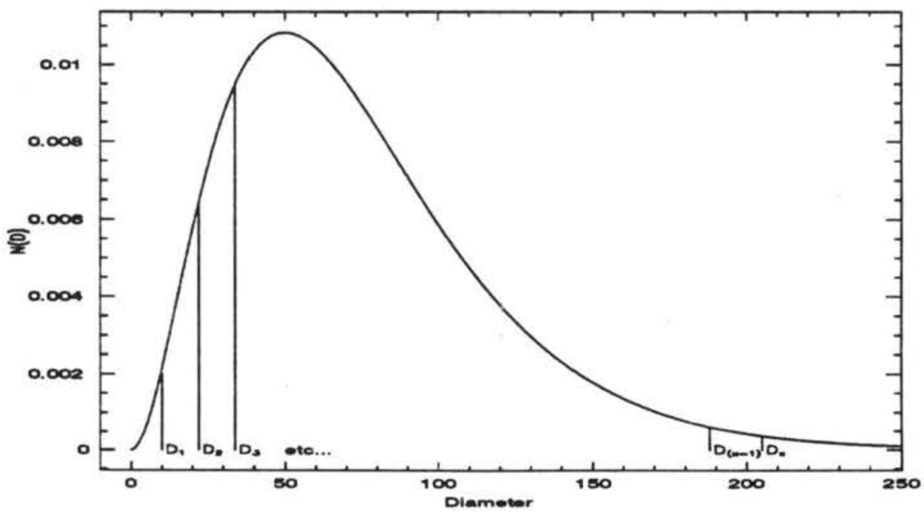

Figure 4.2: Bin Representation: An example of the bin representation of the gamma distribution. The distribution is divided up into x number of bins of a given diameter defined by $D_i = D_{i-1} + \Delta D$

Consider the established distribution shown in Figure 4.2 with $\nu \simeq 3$. To initialize the bin representation, the range of the distribution ($0 \rightarrow D_{max}$ =RANGE) is divided into a certain number of bins (N_{bins}) by defining each bin in terms of a specific diameter. The bins start with $D_0 = 0$ and continue as $D_i = D_{i-1} + \Delta D$ where $\Delta D = N_{bins}/D_{max}$ and i denotes the ith bin. To complete the bin representation of the distribution, the number and mass in each bin (at each diameter, D_i) needs to be specified. This is accomplished by the use of the following relations,

$$N_i = n(D_i)\Delta D = \frac{1}{\Gamma(\nu)}\left(\frac{D_i}{D_n}\right)^{\nu-1}\frac{1}{D_n}exp\left(-\frac{D_i}{D_n}\right)\Delta D, \tag{4.98}$$

and

$$M(D_i) = \frac{1}{\rho_a}m(D_i)N_i, \tag{4.99}$$

where $n(D_i)$ is the normalized gamma distribution and $M(D_i)$ is defined by using (4.3). The total mass in the distribution is also needed in order to define the mass loss ratio and is defined by,

$$r_{tot} = \sum_{i=0}^{N_{bins}} M(D_i). \tag{4.100}$$

Note that since (4.98) is normalized, $N_{tot} = 1$.

Using this representation, the model is run using time steps (chosen by the model) which are small enough to resolve a user-defined increment of $X\%$ in the $\dot{r}\Delta t/r_{tot}$ and $\dot{n}\Delta t/n_{tot}$ ratios. During these runs values of S_i, D_n, T, P, ν and the crystal habit are held constant. The total time for the evaporation run is found by integrating (4.44) to find the time needed to completely evaporate the largest crystal (D_{max}) in the distribution. The integral is,

$$\int_{D_{max}}^{0} D^{\beta-2}dD = \int_0^T \Phi dt = \Phi\int_0^T dt, \tag{4.101}$$

as long as we assume that Φ is not a function of time. This is not necessarily true, however we are only after an estimate of the time for the evaporation run, so this formulation is sufficient. Solving for T gives,

$$T = -\frac{D_{max}}{\beta - 1}\frac{1}{\Phi}. \tag{4.102}$$

This time, T (or a multiple of T depending upon the time step used), is used to put an upward limit on the amount of time needed for the distribution to completely evaporate.

Tabulation of the relationship between the $\dot{r}\Delta t/r_{tot}$ and $\dot{n}\Delta t/n_{tot}$ ratios is accomplished by using the growth equations (4.41) and (4.44). In order to find the new diameter in a given bin after a time step, Δt, (4.44) is written in integral form as,

$$\int_{D_{t-\Delta t}}^{D_t} D^{\beta-2}dD = \int_{t-\Delta t}^{t} \Phi dt, \tag{4.103}$$

where D_t is the diameter at the present time, after mass has evaporated from the crystal, and $D_{t-\Delta t}$ is the previous value of the diameter. Assuming that Φ does not vary over the time-step (a reasonable assumption if the time step is small) allows this integral to be solved easily, it yields

$$D_t = \left\{(\beta - 1)\Phi\Delta t + D_{t-\Delta t}^{\beta-1}\right\}^{1/(\beta-1)}. \tag{4.104}$$

This relation is used to describe the evaporative number and mass loss processes. Note that according to (4.104) two possible situations exist. The first being when in (4.104) the following condition exists,

$$ABS\{(\beta - 1)\Phi\Delta t\} \geq D_{t-\Delta t}^{\beta-1}. \tag{4.105}$$

When this condition exists in any given bin, the crystals in that bin have completely evaporated. When this occurs the number within that bin is passed to a variable for the total loss. This is done for all bins in which the above condition exists. If I_e is assumed to describe the maximum bin in which the above condition is true, then the variable for the total concentration loss can be written as,

$$N_{tloss} = N_{tloss} + \sum_{i=0}^{I_e} N_i. \tag{4.106}$$

The mass lost due to the complete evaporation of crystals is given by

$$M_e = \sum_{i=0}^{I_e} M(D_i). \tag{4.107}$$

The total mass removed, however, cannot be written just at this point. The reason is that we are looking for the ratio of total mass loss to the total mass in the distribution. To describe total mass loss we need to look at the second situation described by (4.104). This condition is,

$$ABS\{(\beta - 1)\Phi\Delta t\} < D_{t-\Delta t}^{\beta-1}. \tag{4.108}$$

When this condition is true the crystals in that bin shrink due to evaporation but do not completely evaporate. The new diameter that the crystal obtains is described by (4.104). Mass removal from this bin is given by,

$$M_{loss}(D_i) = \frac{1}{\rho_a}\frac{dm}{dt}N_i. \tag{4.109}$$

The total mass removed is then described by adding the amount from the crystals that completely evaporate, M_e, and the amount given by (4.107). This is,

$$M_{tloss} = M_{tloss} + M_e + \sum_{I_e}^{N_{bins}} M_{loss}(D_i). \tag{4.110}$$

Equations (4.106) and (4.110) are the equations that are needed to calculate the ratios,

$$\frac{\dot{r}\Delta t}{r_{tot}} = \frac{M_{tloss}}{r_{tot}} \tag{4.111}$$

$$\frac{\dot{r}\Delta t}{r_{tot}} = \frac{N_{tloss}}{n_{tot}}. \tag{4.112}$$

This procedure is continued with values of the above ratios stored in $X\%$ increments until all of the crystals in the distribution have completely evaporated.

At this point it should be noted that the new diameter calculated with (4.104) is *not* reclassified and placed into a different bin. The bins in this model are fixed and the diameters in the bins are allowed to shrink by evaporation in accordance with (4.104). This is not an exactly realistic representation since the real spectra would shift to smaller sizes as the evaporative process takes place. For our purposes, however, this shift is not necessary. All we are after is the relation between the two ratios and the shift in the spectra will not affect this in this model set up.

To check the importance of the physical parameters S_i, T, P, D_n, ν and crystal habit on the mass and number loss ratios, runs were done in which these physical parameters were varied over a wide range of values. The reason for doing this becomes apparent when one considers the fact that any variable that causes significant variations in the results will need to be included in the look-up tables. Therefore we would like to minimize these.

Runs were done of this evaporative concentration loss scheme in which S_i, P, T, and $\bar{D}$ were varied over large ranges. Figure 4.3 shows the generated curves of mass loss ratios plotted against number concentration loss ratios. In this simulation, temperature, pressure, and mean diameter were all held fixed; also the runs were done for needles and for hexagonal plates. Note that variation of the curves is slight over the range of S_i used. There seems to be larger variations at smaller mass loss ratios for needles, but this is mostly due to uncertainty at these points.

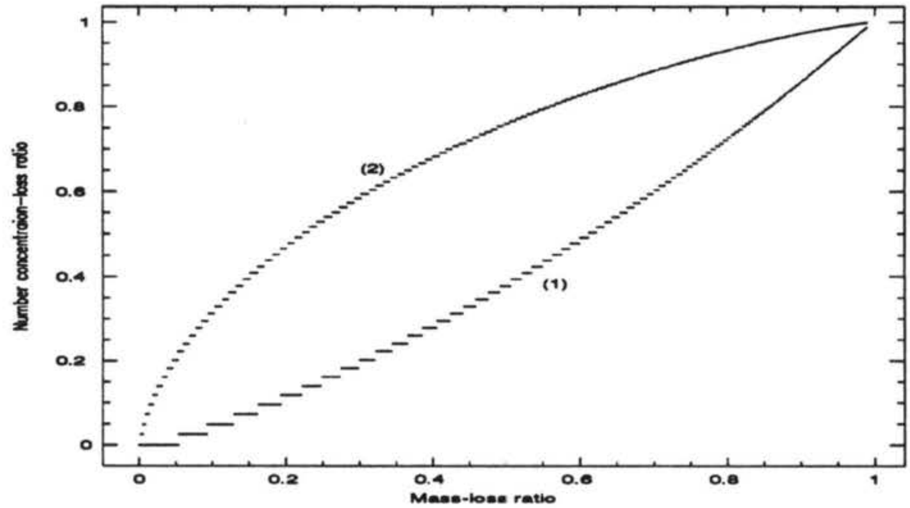

Figure 4.3: Plots of $(\dot{r}\Delta t)/r_{tot}$ vs. $(\dot{n}\Delta t)/n_{tot}$: Curve (1) is for needles and curve (2) is for hexagonal plates. Variation is over the range $S_i = 0.1 \rightarrow 0.9$

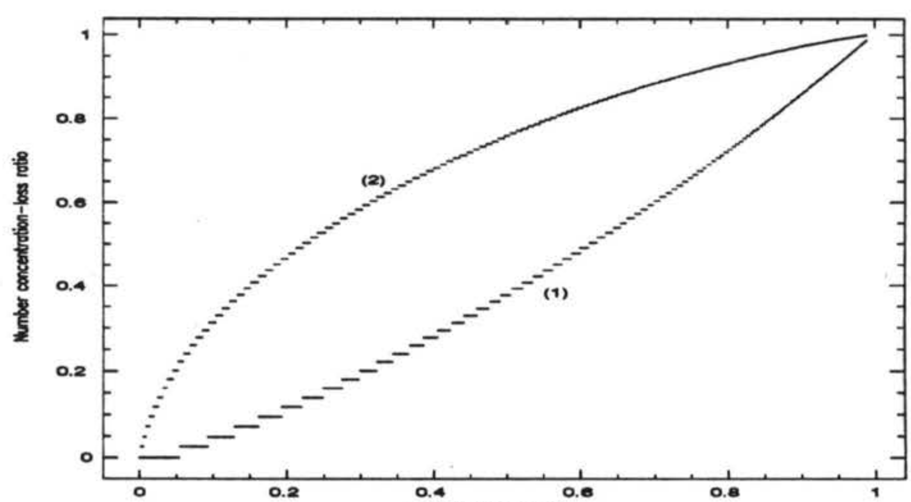

Figure 4.4: Plots of $(\dot{r}\Delta t)/r_{tot}$ vs. $(\dot{n}\Delta t)/n_{tot}$: Curve (1) is for needles and curve (2) is for hexagonal plates. Variation is over the range $T = -30 \rightarrow 30°C$

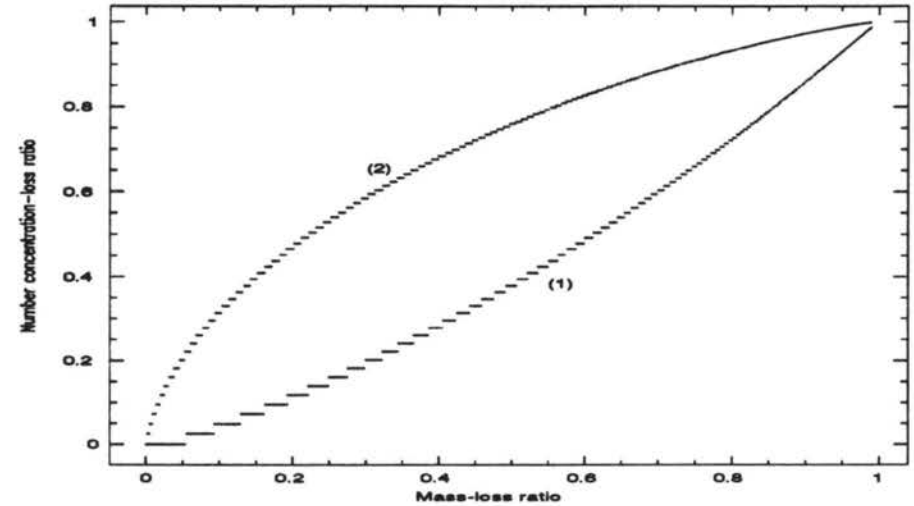

Figure 4.5: Plots of $(\dot{r}\Delta t)/r_{tot}$ vs. $(\dot{n}\Delta t)/n_{tot}$: Curve (1) is for needles and curve (2) is for hexagonal plates. Variation is over the range $P = 600 \rightarrow 200mb$

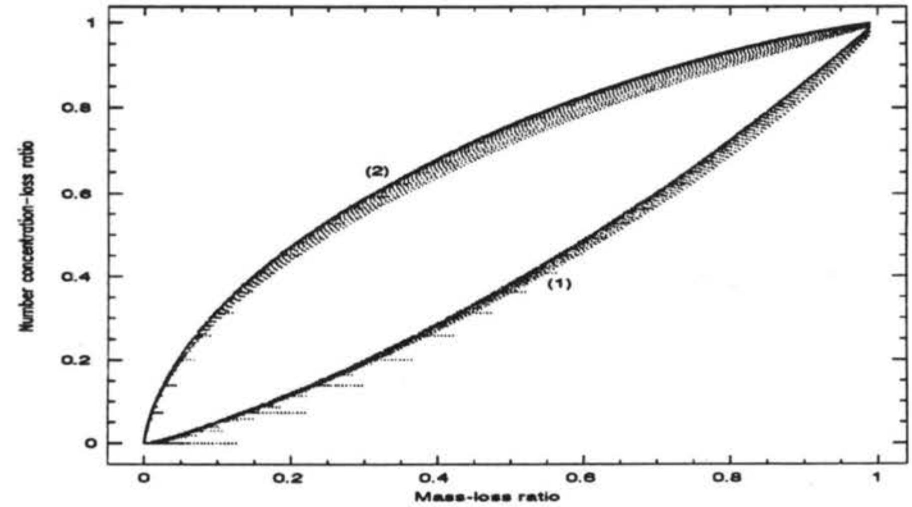

Figure 4.6: Plots of $(\dot{r}\Delta t)/r_{tot}$ vs. $(\dot{n}\Delta t)/n_{tot}$: Curve (1) is for needles and curve (2) is for hexagonal plates. Variation is over the range $\bar{D} = 10 \rightarrow 300\mu m$

As a quick aside, the reason for using only two habits is that habit, as will be shown, is important in the evaporative scheme because of the power, β, in the mass-diameter relationships. Since the lowest value of β is 1.8 for needles and the highest is 2.5 for hexagonal plates, these two crystal habits were used as examples to illustrate the effect.

Figures 4.4 and 4.5 show the results for variation in temperature and pressure, respectively. Note that these curves are very similar to the variation in S_i curve. It seems that both pressure and temperature do not affect out number concentration loss values enough to include them in the look-up table. Figure 4.6 shows the results for variation in $\bar{D}$. This curve, unlike the others, has a noticeable spread. Since the dependence of the ratios on $\bar{D}$ is not too large, we will choose to leave any D dependence out of the look-up tables; instead the $\bar{D}$ results are used to define the $\bar{D}$ used in creating the look-up tables.

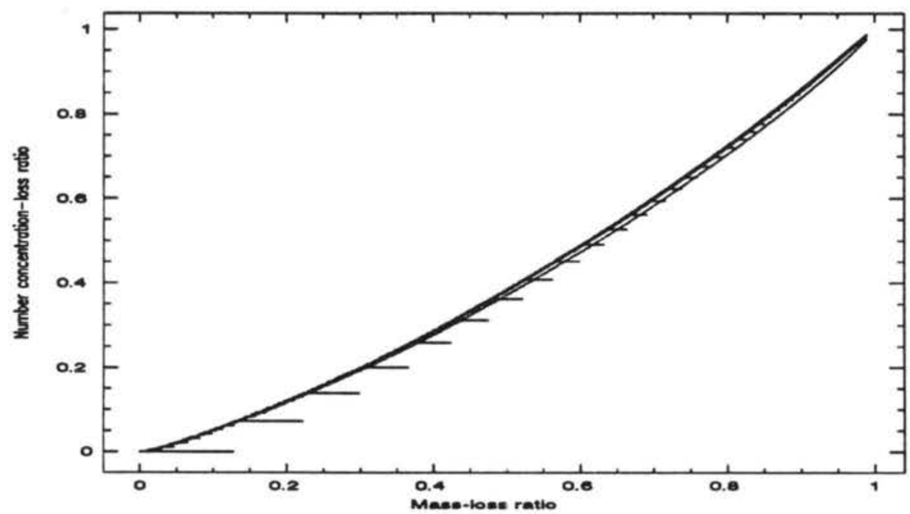

Figure 4.7: Plots of $(\dot{r}\Delta t)/r_{tot}$ vs. $(\dot{n}\Delta t)/n_{tot}$: Simulation for needles with $\nu = 1$; ranges over pressure from $P = 600 \rightarrow 200mb$, temperature from $T = -30 \rightarrow 30°C$ and mean diameter from $\bar{D} = 10 \rightarrow 300\mu m$

Figure 4.7 shows a plot of the mass-loss and number concentration-loss curve with variation over ranges in P, T, and $\bar{D}$; S_i was set to 0.8 and the distribution shape was assumed to be Marshall-Palmer ($\nu = 1$). Simulations were done over these different ranges in order to test as many possible cases that may cause deviations in the curve. Note that there is little variation in the curve for the evaporative ratios over the given ranges. The widest variations shown in the figure are due to the diameter variation. Still, we feel it is possible to parameterize the evaporative number concentration-loss look-up tables with values of these parameters set at values that define the bulk average of the curve. The values chosen here are T=273.15 K, P=400 mb, and $\bar{D} = 40\mu m$. These values are representative of values that define an average curve. Errors associated with the removal of $\bar{D}$ from the tables are around a maximum of about 9 % . Similar results can be shown for different values of the ν and for different habits. However, these are not produced here.

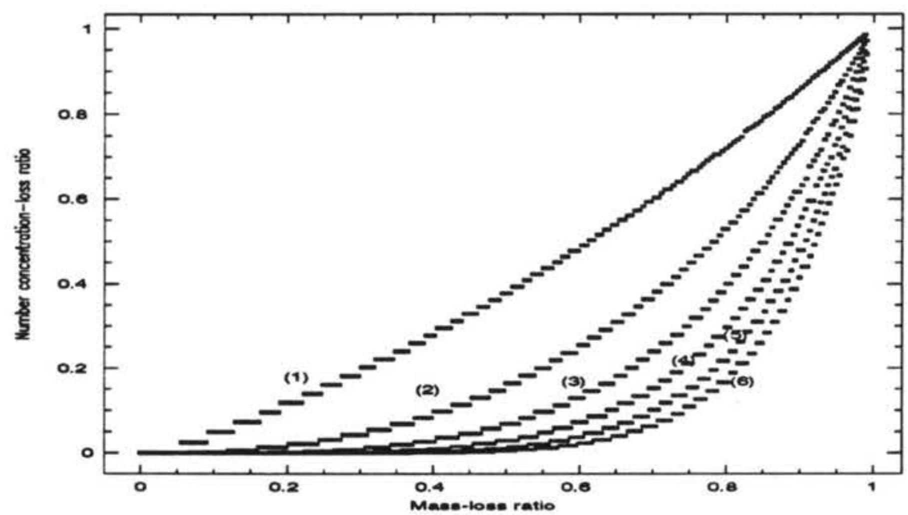

Figure 4.8: Sublimation ratio's varying ν: Curve (1) describes evaporation for $\nu = 1$, curve (2) describes evaporation for $\nu = 2$, etc. up to $\nu = 6$. For these simulations T=273.15 K, P=400mb, $\bar{D} = 30\mu m$, and $S_i = 0.8$. Crystal habit was needles.

The parameters that do cause significant shifts in the evaporative loss curves are ν and the crystal habit. The reasons for this will be explained shortly. Figure 4.8 shows plots of the mass-loss and number concentration-loss ratios for different values of ν. Note that for a value of $\nu = 1$ the mass-loss ratio to number loss ratio is roughly 1:1, and as the value of ν increases, the evaporation ratio must become larger and larger before a significant loss in number concentration is observed. This is due to the fact that as ν increases, the tail of the distribution near zero becomes tighter. For example, a distribution with $\nu = 1$ has more of its mass and number near zero than a distribution with $\nu = 3$. Thus, it only makes sense that evaporation of crystals (since the tail end is removed first in the bin model) would

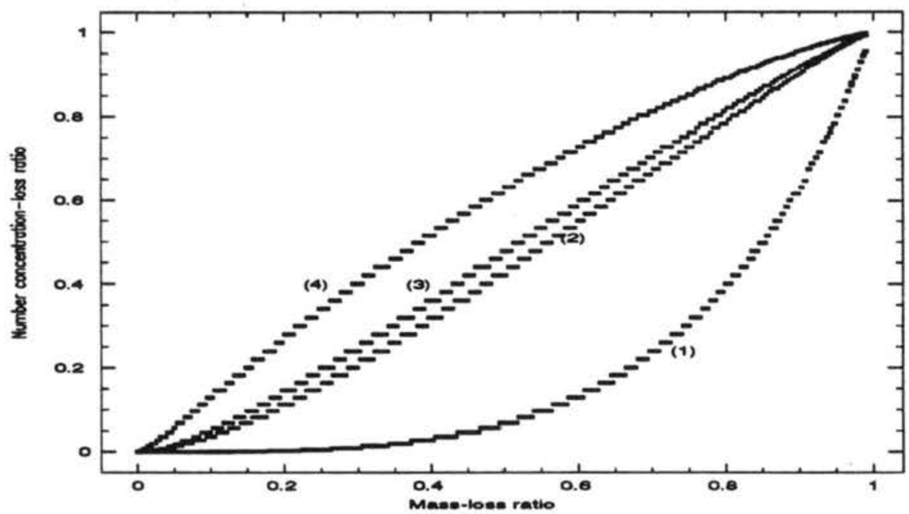

Figure 4.9: Sublimation ratio's varying crystal habit. Curve (1) describes evaporation for needles and for long columns, curve (2) for hexagonal plates, curve (3) for short columns and curve (4) for spheres. Simulation T, P, S_i, and $\bar{D}$ are the same as above. A shape parameter of $\nu = 3$ was used.

proceed faster initially from a number-concentration-loss stand-point for a distribution with $\nu = 1$ than for a distribution with $\nu = 3$.

Figure 4.9 shows the relation of the mass-loss ratio and number concentration-loss ratio to the choice of habit. Again, note the shift in the curve due to this choice. Of particular interest is the fact that for spheres, the percentage number concentration-loss is larger initially for any given percentage mass-loss with this tendency reversing as the ratios approach 1. The opposite trend is observed for needles, with large initial percentage mass-losses being needed in order to see any appreciable change in the percentage number concentration loss. The reason for this shift in the curve due to the different habits is related to the mass-diameter relationship. Recall that this is given by,

$$m(D) = \alpha D^{\beta} \tag{4.113}$$

where α and β are given constants. Now, for spheres, $\beta = 3$ while for needles $\beta \simeq 1.8$. This power influences the way in which the given crystals evaporate. To see this recall our equation for the time change of diameter,

$$\frac{dD}{dt} = \Phi D^{2-\beta}. \tag{4.114}$$

This equation, which was used above to evaporate the distributions, is the reason for the observed shifts in the curves. For spheres, $2 - \beta = -1$, giving a 1/D dependence while for needles $2 - \beta = 0.2$, giving a $D^{0.2}$ relationship. Since the bin model allows for the evaporation of the smallest crystals first, note that the 1/D relationship for a small diameter will give a larger number than the $D^{0.2}$ relationship for needles. Thus, for a given percentage mass-loss ratio (below about 0.50) the percentage number concentration-loss will be larger for the sphere than for the needle habit. This can be seen for the hexagonal plates and the short columns. Hexagonal plates have a $\beta = 2.5$ while short columns have a $\beta = 2.6$. For hexagonal plates we then have a $D^{-0.5}$ dependence to the dD/dt equation while short columns have a $D^{-0.6}$ dependence. Thus, we would expect to see larger initial losses in number concentration (for percentage mass-losses of less than about 0.5) for short columns than for hexagonal plates, this is what Figure 4.9 shows.

Upon examining Figures 4.3 to 4.9 it is obvious that the number loss ratio is weakly dependent upon T, P, D_n, and S_i. It may seem that certain parameters such as S_i should have a large effect on the number loss ratio, it does; through the mass loss ratio. The mass loss ratio is a strong function of ice subsaturation and, as it would seem, the number loss ratio is a strong function of the mass loss ratio. Thus, the S_i dependence really is taken into account through the relation of the number loss ratio to the mass loss ratio. Since the evaporative number loss ratio is weakly dependent upon these parameters, we choose here to fix the values of these parameters at physically realistic values for the creation of the tables. Values of ν and variation in crystal habit, however, have a large effect upon the shape of the curves of $\dot{r}\Delta t/r_{tot}$ and $\dot{n}\Delta t/r_{tot}$. Our table of evaporative number loss is thus set to be a function of the shape of the distribution, the crystal habit, and the evaporative mass loss ratio.

Chapter 5

MICROPHYSICAL TESTS USING A ONE-DIMENSIONAL LAGRANGIAN MODEL

The evolution of the ice spectra described above is examined through the use of a simple one-dimensional Lagrangian parcel model as described by Tripoli and Cotton (1981). In this section the one-dimensional model will be described breifly. Then, the basic set-up of the model for the tests of the spectral evolution will be explained. Finally, examination and comparison of the tests will be done.

5.1 Lagrangian Model

The one-dimensional model used here is run for ice-saturated accent and ice-subsaturated descent. The model is initialized with a given pressure level, P_{bot}, a given vapor content r_t, and a given temperature, T_{init}. An updraft profile is assumed and has the following matehmatical form,

$$w = w_{max}\left\{sin\left(-\frac{\pi(P - P_{bot})}{P_{bot}}\right)\right\} \tag{5.1}$$

where w_{max} is the maximum of the updraft. This formulation for w is used here simply as a means of finding a time scale for the microphysical calculations. The pressure in the model was lowered (or raised) in increments of ΔP and a height scale derived from this using the hypsometric equation, given in Tripoli and Cotton as

$$\Delta Z = -\frac{RT}{g}ln\left\{\frac{P}{P+\Delta P}\right\}, \tag{5.2}$$

where ΔZ is the height change associated with the given pressure drop (or increase). This is then used to calculate the time scale for the calculations as,

$$\Delta t = \frac{\Delta Z}{w}. \tag{5.3}$$

Diagnosis of temperature at every step is accomplished by using the conservative variable, θ_{il}. The ice-liquid water potential temperature, θ_{il} is conservative during phase changes of water as long as fluxes of water species into or out of the parcel do not occur. Because it is conserved during phase changes of water, θ_{il} is ideal for use as a thermodynamic variable. Since all water species must travel with the parcel, the total initial mixing ratio is set as,

$$r_t = r_v + r_p + r_s \tag{5.4}$$

where r_t is the total mixing ratio, r_v is the mixing ratio of water vapor, r_p is the mixing ratio of pristine ice, and r_s is the mixing ratio of snow. The model is run with preexisting distributions (r_p and r_s not zero) and with initially only water vapor present.

In order to diagnose temperature during the model generated ascent or descent an initial value of θ_{il} needs to be known, and can be calculated with the following relation,

$$\theta_{il} = \theta_{il,init} = \theta_{init}(T_{init})exp\left\{-\left(\frac{L_{iv}(T_0)r_i}{C_pT_{init}}\right)\right\} \tag{5.5}$$

where L_{iv} is the latent heat of sublimation, $r_i = r_p + r_s$ is the ice mixing ratio, C_p is the specific heat of dry air at constant pressure, and θ_{init} is the value of θ calculated from the initial temperature. Note that this equation for θ_{il} lacks the terms for the liquid phase. This is not a problem here, however, since only the vapor and ice phases of water are used.

Knowing the value of θ_{il} allows the value of θ and T to be calculated at every step. Calculation of an exact value of θ requires solution of the equation,

$$d_i ln\left(\frac{\theta_{il}}{\theta}\right) = -d_i\left\{\frac{L_{lv}r_l}{C_pT} + \frac{L_{iv}r_i}{C_pT}\right\} + \frac{r_l}{C_p}d\left(\frac{L_{lv}}{T}\right) + \frac{r_i}{C_p}d\left(\frac{L_{iv}}{T}\right) \tag{5.6}$$

where L_{lv} is the latent heat of vaporization and r_l is the mixing ratio of liquid water. The terms in the above equation that include these variables are not of interest here since only vapor and ice phases of water are used. Approximations to the solutions of this equation are common for the diagnosis of θ, one of which is to throw out the last two terms that deal with the changes in the latent heats by assuming that they are small. Since the second term in the above equation becomes increasingly important at low temperatures approximations of this sort can result in large errors in the diagnosis of θ at low temperatures. To compensate for this, Tripoli and Cotton (1981) defined the following function that allowed for better diagnosis of θ,

$$\theta = \theta_{il}\left\{1 + \frac{L_{iv}(T_0)r_i}{C_p max(T, 253)}\right\} \tag{5.7}$$

The term for the liquid phase has been left out. This equation is used here to diagnose θ during the model runs.

5.2 Results of the One-Dimensional Simulations

One-dimensional simulations of the prognostic equations were run using the above model for distributions initiated with the Meyers et al. (1992) nucleation equation. Before going into a description of the simulations, the bounds of the distributions are defined and how the calculations are corrected if the distributions beyond these.

5.2.1 Distribution Bounds

During any type of modeling study, it is important to make sure that the physical processes that are being studied stay within a certain set of realistic bounds. When using a bimodal description of the ice spectra, one of these bounds is on the mean diameter of the particles. Since we define pristine ice to be any crystal with a diameter less than D_b and snow to be any crystal larger than D_b, it seems reasonable that this value should bound the diameters of the two ice classes. The bounds for pristine ice and snow are defined as,

$$\bar{D}_{max} = 0.9D_b\text{: for pristine ice} \tag{5.8}$$

$$\bar{D}_{min} = 1.1D_b\text{: for snow.} \tag{5.9}$$

The mean diameter for pristine ice is not allowed to get larger than D_{max} and the mean diameter of snow is not allowed to get smaller than D_{min}.

The reason for imposing these constraints, besides the obvious fact that pristine ice and snow should be confined to a definite size range, has to do with reforming the distribution as a complete gamma distribution after every time-step. Consider the situation shown in Figure 5.1 , which shows an example of the pristine ice distribution at times t and $t + \Delta t$ during evolution in an environment that is supersaturated with respect to ice. Since the crystals are in a ice supersaturated environment, pristine ice crystals will grow by vapor deposition, and some of the pristine ice mass and number concentration will be transfered to the snow distribution. The process of vapor depositional growth causes the spectra to shift to larger diameters since D_n is diagnosed from r_p. The flux process moves mass and number concentration from a region of $D + \Delta D$ around the boundary D_b of the pristine ice distribution to the snow category causing a decrease in the pristine ice D_n. There are two possible limiting situations for the evolution of the D_n profile. The first is when the flux of crystals becomes greater than the vapor depositional growth of the distribution. For this case, the mean diameter, and therefore D_n will decrease. The second situation is when the vapor depositional growth of the distribution is greater than the transfer rate. When this occurs the mean diameter of the ice crystals increases, as shown in Figure 5.1. There is, therefore, the possibility of the values of D_n going beyond their physical bounds.

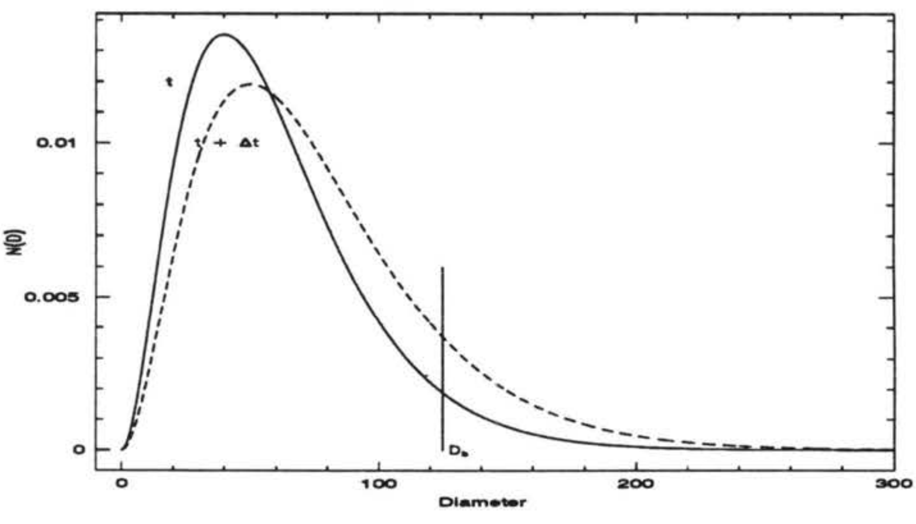

Figure 5.1: Pristine ice distribution at times t and $t + \Delta t$. The value of D_n at time, t, is 20 μ m; at time $t + \Delta t$ the value of D_n is 25 μ m. Note the larger amount of mass associated with the distribution tail at time $t + \Delta t$.

A similar thing happens for the snow distribution when the ambient air is subsaturated with respect to ice. As mass is lost from the distribution due to evaporation and due to the flux of mass and number concentration from snow to pristine ice, the values of D_n can become smaller than physically plausible.

In order to constrain the distribution mean diameters from becoming too large or too small (depending upon the case), the above constraints are placed on the mean diameters of the pristine ice and snow distributions. If, in a given time-step, the values of D_n become too large for the case of pristine ice, then the number concentration transfer to snow is suppressed while the mass transfer is kept at the model determined value. This keeps the pristine ice D_n value within reasonable physical bounds since D_n is an inverse function of number concentration (recall (4.4)). For the case of the transfer of snow to pristine ice, if the value of the mean diameter of snow becomes less than the given constraint, number concentration flux to pristine ice is increased to compensate. Our choice of limiting number concentrations is an arbitrary one. We argue, however, that it is more important to conserve mass than particle number concentration.

5.2.2 One-dimensional simulations

The model that was described above is used here to show the evolution of the ice spectra for various ice crystal habits and distribution shape parameters, ν. The growth of the ice spectra also varies depending upon the initial temperature and water vapor mixing ratio, however, variations in these parameters just tend to shift the model profiles. Lowering or raising these parameters either enhances ice nucleation or causes it to occur at higher model levels. Thus, variations in these parameters will not be examined. Two model crystal habits, needles and hexagonal plates, were examined. The reason for picking these two habits has to do with the exponential parameter β in the ice crystal mass relation. The parameter β is an important parameter in the determination of the mass and number concentration fluxes and in the equations for the mass gain and loss of the distributions, crystals which characterized the lowest and highest values of β were used. Needles have the lowest value, $\beta = 1.8$ while hexagonal plates have one of the highest values at $\beta = 2.6$. A constant updraft of 1 m/s was used, giving a time step of $\Delta t = 1.7$ seconds.

The simulations conducted test how the equations respond to the different crystal types and distribution shapes given above. Simulations are first conducted for needle crystals with a distribution shape of $\nu = 3$. This simulation is compared with a run initialized with the same physical conditions except that the distribution shape is Marshall-Palmer; $\nu = 1$. This shape of the pristine ice distribution conforms to the replicator data of Arnott et. al. (1993) from the FIRE II experiment. A final simulation tests the difference in spectral evolution when a different crystal type is considered. For this simulation hexagonal plates were used with a distribution shape of $\nu = 1$.

Case 1: Needle crystals with pristine ice distribution shape $\nu = 3$

Figure 5.2 shows the evolution of the ice spectra during parcel ascent for ice supersaturated conditions. Ice supersaturation increases quite rapidly as the parcel ascends but drops of as pristine ice crystals nucleate and grow by vapor deposition (see Figure 5.3). After the first 61 time-steps (about 103.7 seconds), the initial peak of pristine ice due to nucleation via the Meyers et al. (1992) formulation can be seen. The distribution of pristine ice grows quickly, broadening as mass is added by vapor deposition. Peak (2) is reached after only 400 time-steps and (3) after 500 time-steps. The rapid broadening of the pristine ice distribution can also be seen by examining the profile of $\bar{D}$ with pressure (see Figure 5.4).

Note that $\bar{D}$ for pristine ice increases quite quickly during the ascent and reaches its maximum value around P=379 mb. At this point, the model doesn't allow for further broadening of the distribution.

The snow distribution becomes noticeable after 150 time-steps (as denoted by (4) in the figure) and broadens after this point very quickly. The reason for the rapid broadening of the distributions has to do with the dependence of the growth equation (dD/dt) on the parameter β and will be examined in more detail later. Again, this rapid broadening is shown in Figure 5.4; $\bar{D}$ for snow initially resides around it's minimum value, however, once the distribution accumulates a significant amount of snow mass, the broadening becomes rapid. Refering to Figure 5.5 (dr/dt Δt) shows this.

Examination of the number concentration profile with pressure given in Figure 5.6 shows that pristine ice number concentration peaks quickly due to nucleation, but starts to fall off as crystals become large enough to become classified as snow.

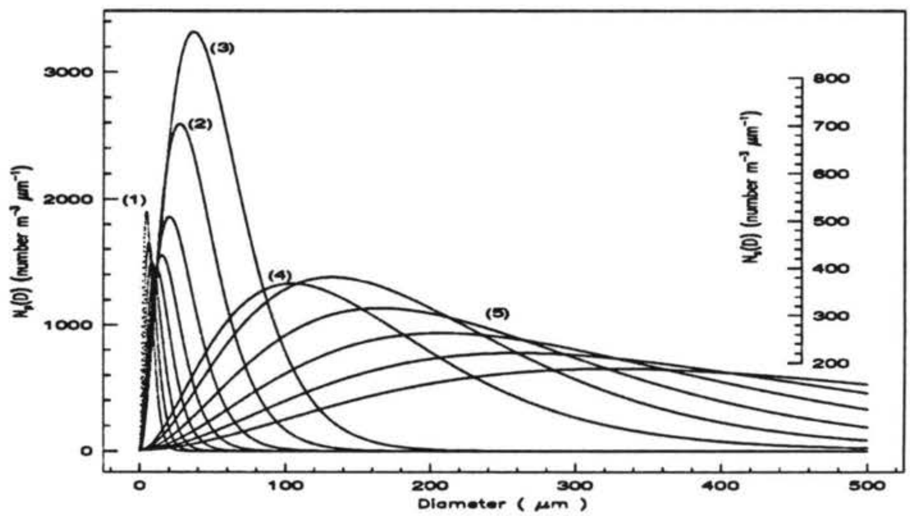

Figure 5.2: Evolution of the ice spectra during model saturated ascent. T=243 K, $r_v = 0.0007$ kg/kg, and the habit assumed for pristine ice and snow is needles.

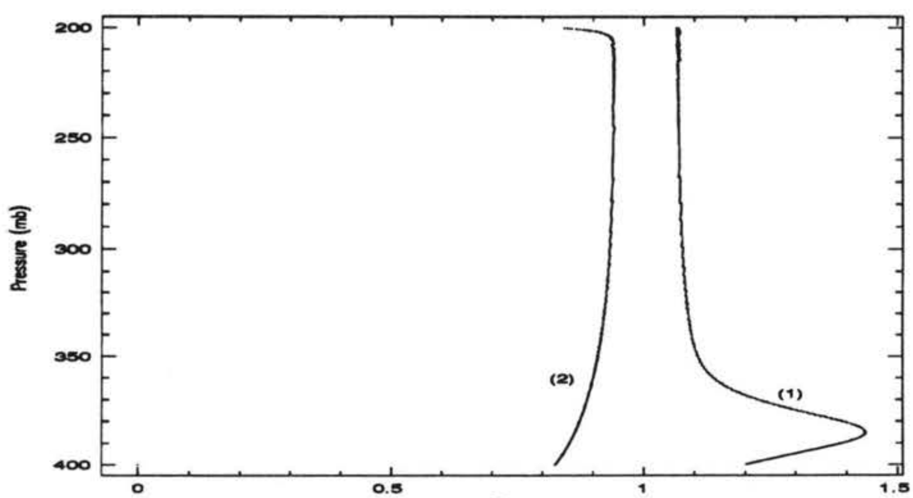

Figure 5.3: S_i vs. Pressure: Model ascent and descent denoted by (1) and (2) respectively

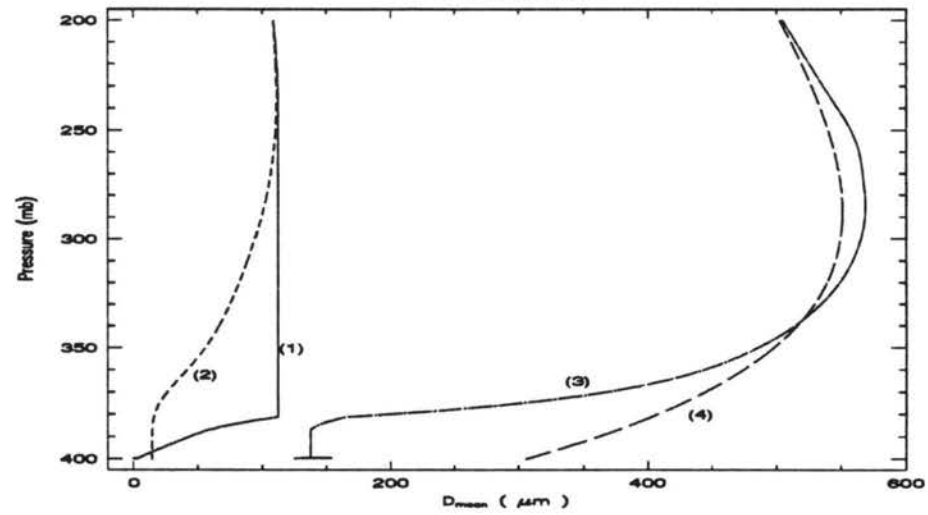

Figure 5.4: D_{mean} vs. Pressure for model ascent and descent. Profile of pristine ice D_{mean} for model ascent and descent are denoted by (1) and (2) respectively. Snow D_{mean} profiles are denoted by (3) and (4) for model ascent and descent respectively.

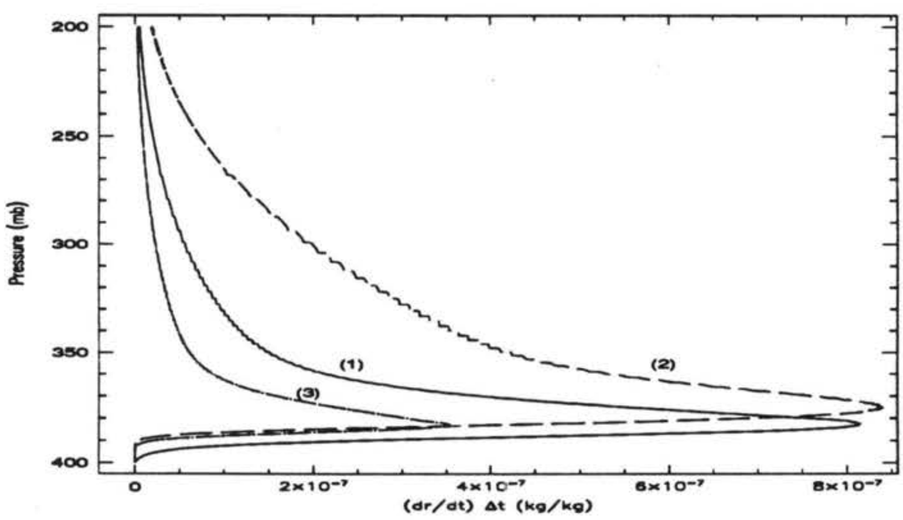

Figure 5.5: $(dr/dt)\Delta t$ vs. Pressure. (1): Pristine ice distribution growth due to vapor deposition. (2): Snow distribution growth due to vapor deposition. (3) The flux of mass from the pristine ice to the snow distribution.

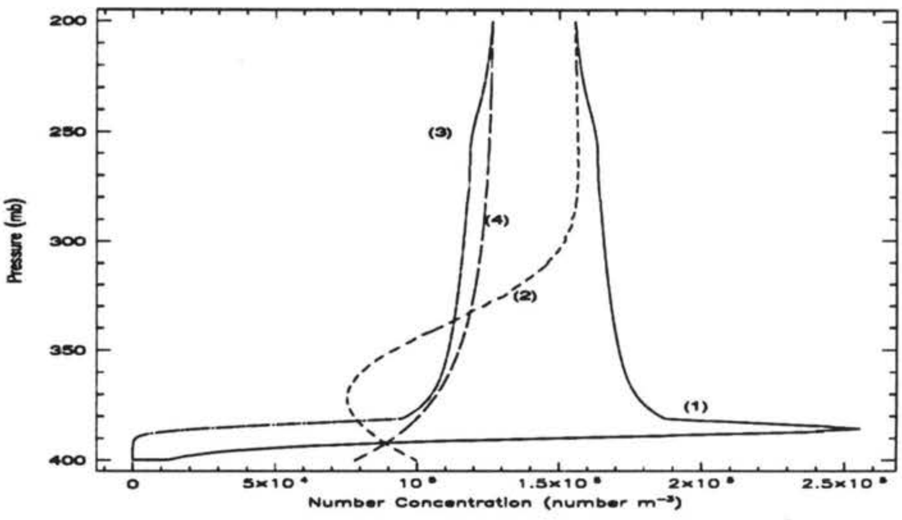

Figure 5.6: Number concentration vs. pressure. (1) Pristine ice number concentration profile during model ascent. (2): Pristine ice number concentration during model descent. (3) Snow number concentration during model ascent. (4): Snow number concentration during model descent.

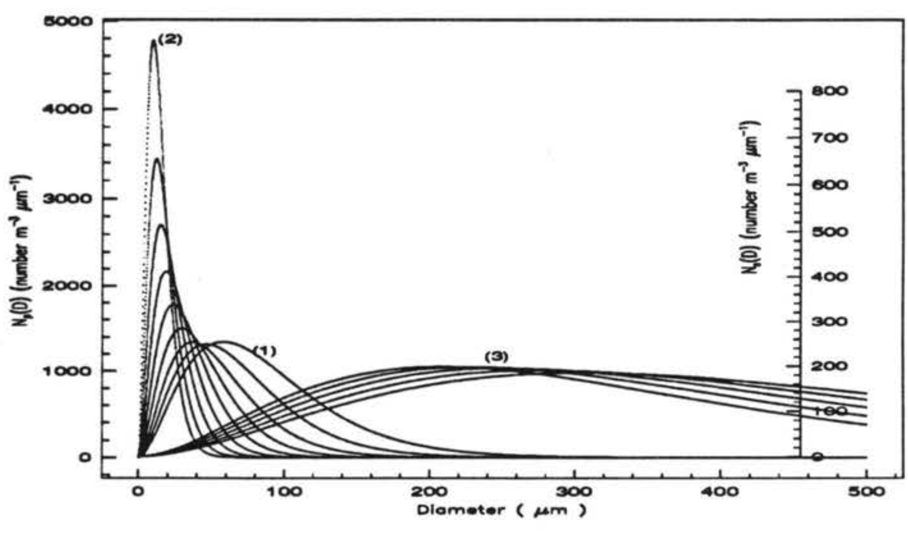

Figure 5.7: Evolution of the ice spectra during model subsaturated descent. Initialization of the model parameters was with the parameters at the top of the ascent

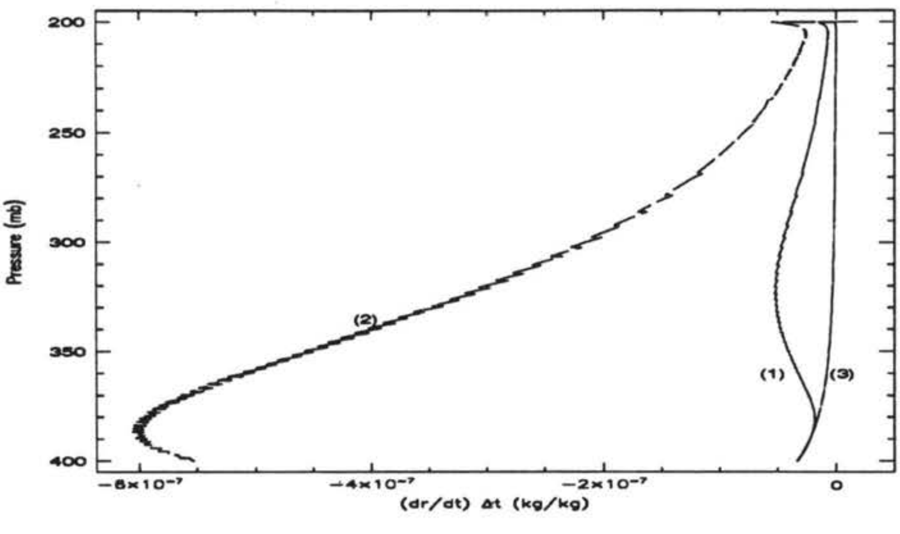

Figure 5.8: $(dr/dt)\Delta t$ vs. pressure for the model descent. (1):Pristine ice mass loss due to sublimation, (2): Snow mass loss due to sublimation (3): Mass transfer from snow to pristine ice.

Note that the number concentration of snow increases quickly and then tends to level off with increases occuring slowly. The initial increase in the snow distribution's number concentration is due to the large number of rapidly growing needle ice crystals produced by nucleation. The snow number concentration increase with height slows during asscent due to the decrease in the initial number concentration of pristine ice.

The ice spectra evolution for the descent is shown in Figure 5.7. The final pristine ice and snow distributions from the ascent phase are used as the initializations for the model descent. In Figure 5.7 the initial pristine ice distribution becomes increasingly more narrow in time due to the evaporation. The peaking of the distribution shown is due to the narrowing and the increase in number concentration due to the flux of number concentration from snow to pristine ice. This narrowing of the pristine ice distribution is shown in Figure 5.4; where the value of $\bar{D}$ slowly decreases as the parcel descends.

Figure 5.5 shows the values of the mass evaporation rates for the pristine ice and snow along with the flux of mass from snow to pristine ice. Note that pristine ice loses more mass due to evaporation than it gains from the flux of snow; this is the reason for the narrowing of the distribution. Number concentrations peaking as the distribution narrows is controlled by the evaporative number loss routine. Figure 5.6 shows the number concentration loss from the pristine ice and snow distribution. Note that the number loss follows the shape of the mass loss curves given in Figure 5.8; as it should, since number concentration loss is a function of distribution mass loss.

Case 2: Needle crystals with pristine ice distribution shape ($\nu = 1$)

The above simulation was repeated for the case of a Marshall-Palmer shaped pristine ice distribution ($\nu = 1$). The evolution of the ice spectra is shown in Figure 5.9. The initial slope of the pristine ice distribution is quite steep due to the large number of ice crystals nucleated at a small diameter.

As the parcel ascends, ice supersaturations increase (see Figure 5.10) and, as a result, ice nucleation increases as does vapor depositional growth of the pristine ice distribution. Thus, the distribution increases drastically at the smaller diameters while continuing to broaden due to growth processes.

As shown in the ice saturation profile, the ice supersaturation continues to increase during ascent until the nucleation and growth processes halt its increase. At this point (or before) nucleation shuts off (since the Meyers et al (1992) formulation is a number tendency and needs to be compared with the number of crystals currently in the parcel). When this occurs, the concentration at smaller diameters ($D \leq 40\mu m$) decreases due to the broadening occuring through vapor depositional growth.

The number concentration profile in Figure 5.11 shows the burst in nucleation of prisitine ice. At P=385 mb nucleation effectively "shuts-off" and the pristine ice number concentration decreases due to the transfer of pristine ice crystals. The snow number concentration increases quickly due to the large amount of pristine ice around. This increase slows as the parcel ascends since pristine ice number concentration is decreasing.

Initially, the snow distribution shown in Figure 5.12 has a small number concentration and mixing ratio due to the fluxes from a pristine ice distribution that is narrow. Thus, the mean diameter of the ice crystals in the distribution are centered around the minimum allowed for snow (as discussed above).

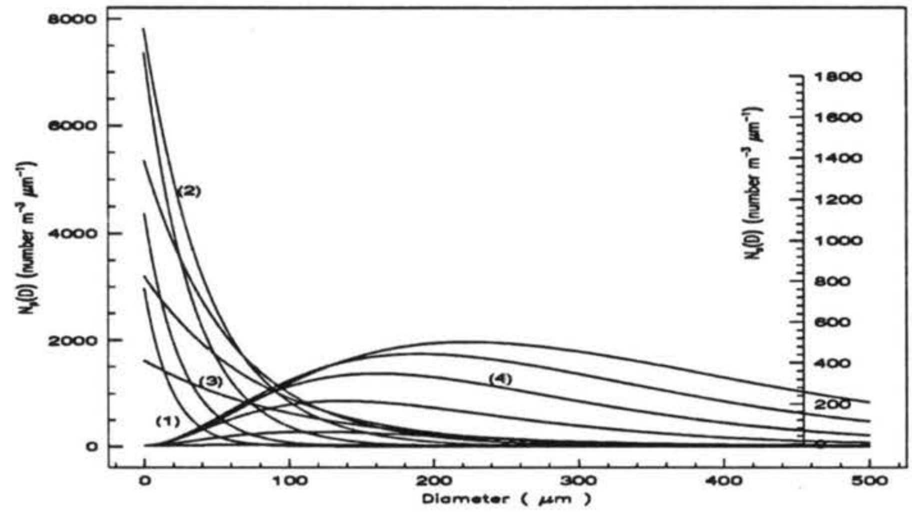

Figure 5.9: Ice spectra evolution during ascent for: $\nu = 1$, $T_{init} = 243$ K, and $r_v = 0.0007$ kg/kg. The pristine ice distribution after 61, 200, and 600 time-steps are denoted by (1), (2), and (3) respectively. (4) shows the snow distribution.

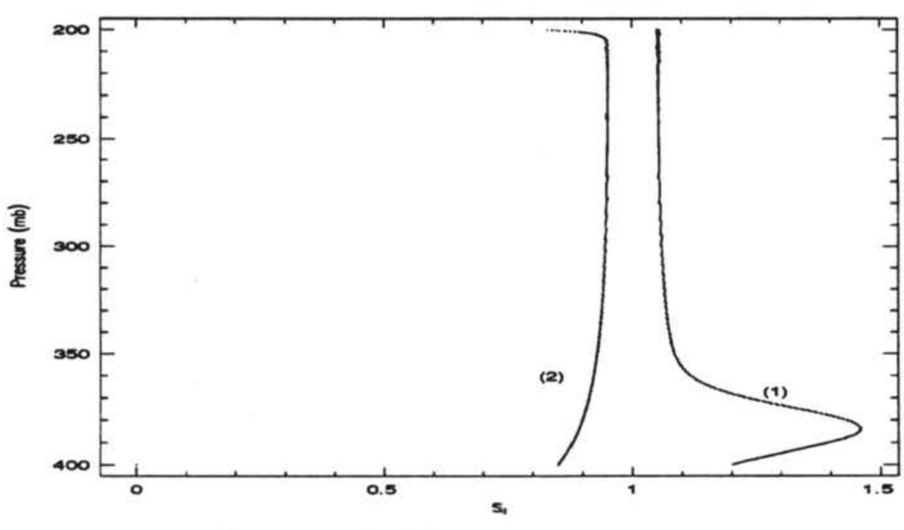

Figure 5.10: S_i vs. Pressure for, (1): model ascent, and (2): model descent.

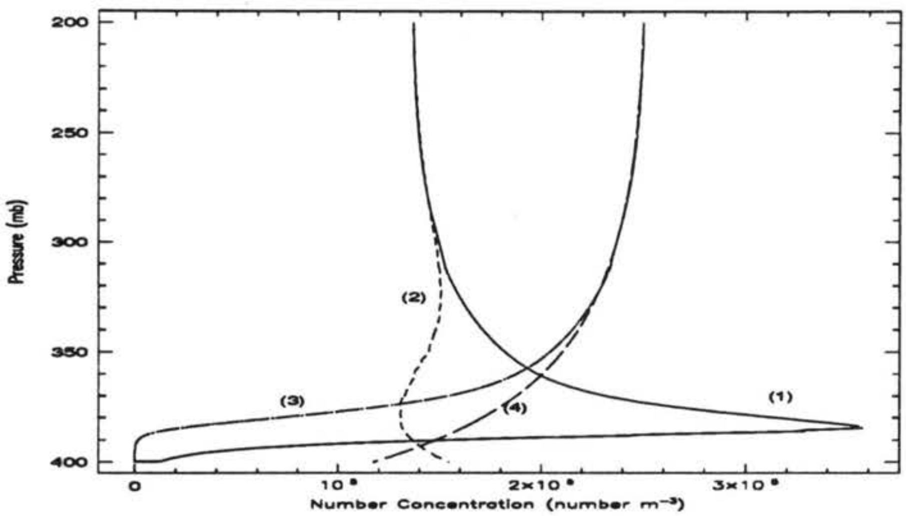

Figure 5.11: Number concentration profile for; (1): pristine ice, model ascent. (2): pristine ice, model descent. (3): snow, model ascent. (4): snow, model descent.

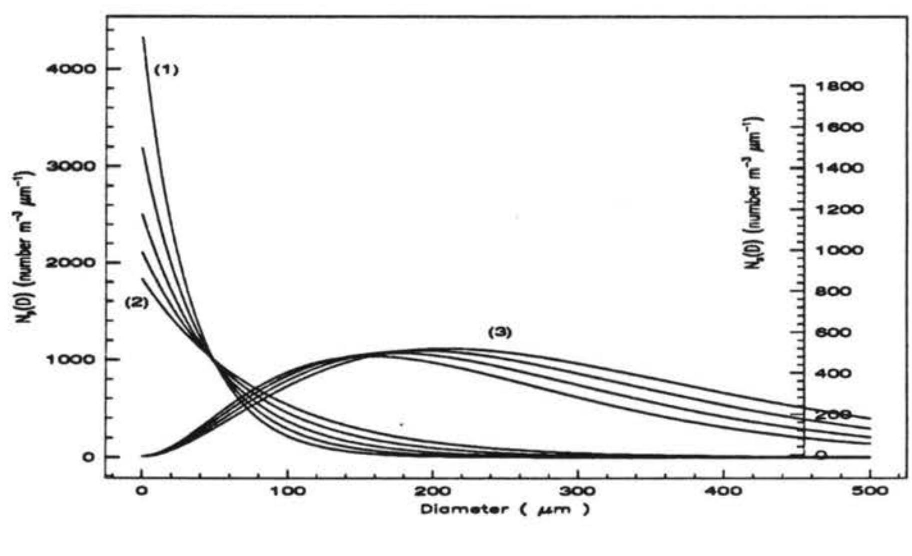

Figure 5.12: Evolution of the ice sepctra for model descent.

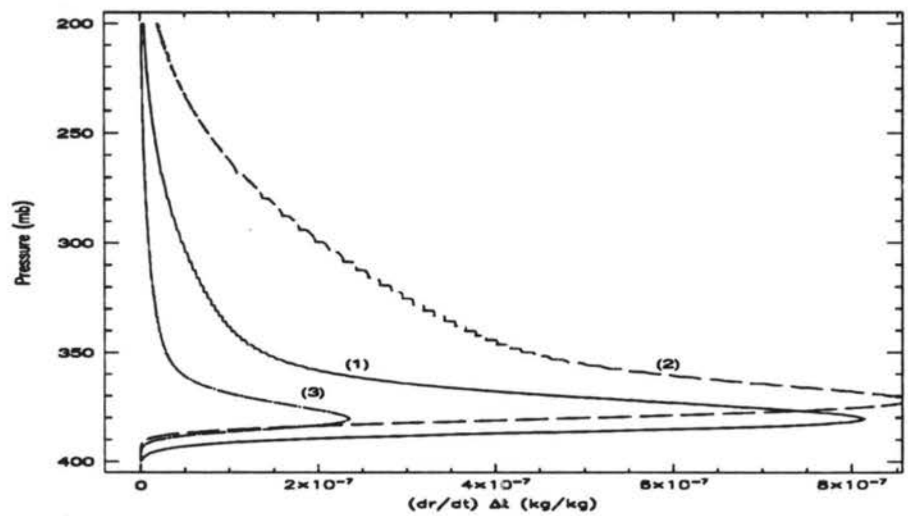

Figure 5.13: $(dr/dt)\Delta t$ vs. Pressure for model ascent: Vapor depositional growth of pristine ice and snow are denoted by (1) and (2) respectively. Mass flux to snow from pristine ice denoted by (3).

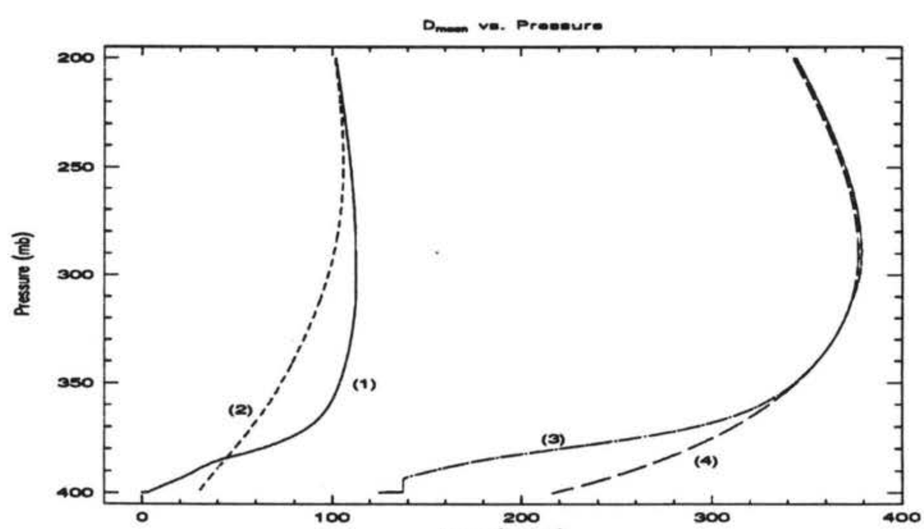

Figure 5.14: $\bar{D}$ profile for; (1): pristine ice, model ascent. (2): pristine ice, model descent. (3): snow, model ascent. (4): snow, model descent.

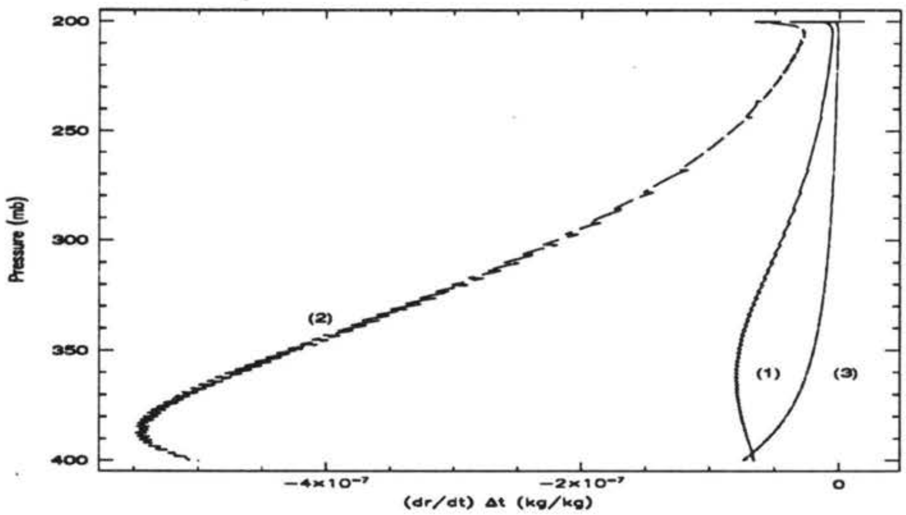

Figure 5.15: $(dr/dt)\Delta t$ vs. Pressure for model descent: Evaporation of mass from pristine ice and snow are denoted by (1) and (2) respectively. Mass flux to pristine ice to snow denoted by (3).

As the distribution of snow gains mass and the distribution broadens it is constrained by the number concentration and mass that is continually added through the flux equations.

Both snow and pristine ice distributional broadening are due to the vapor depositional growth rates shown in Figure 5.13. Pristine ice broadening is hindered by the transfer of mass to the snow category while the snow broadening is enhance by this mass transfer.

The evolution of the spectra for the model descent is shown in Figure 5.12. Both pristine ice and snow distributions become increasingly more narrow as ice mass is lost to the ambient air in the form of vapor. The evolution of the profiles of $\bar{D}$ (Figure 5.14), the number concentration and mass flux profiles (Figures 5.11 and 5.15 respectively) are similar to those presented for the previous case.

Case 3: Hexagonal Plates with Pristine ice distribution shape $\nu = 1$

To examine the effects of crystal habit on the spectral evolution, simulations were conducted in which the physical parameters were the same as for the simulations presented above, however, the crystal shapes were assumed to be hexagonal plates.

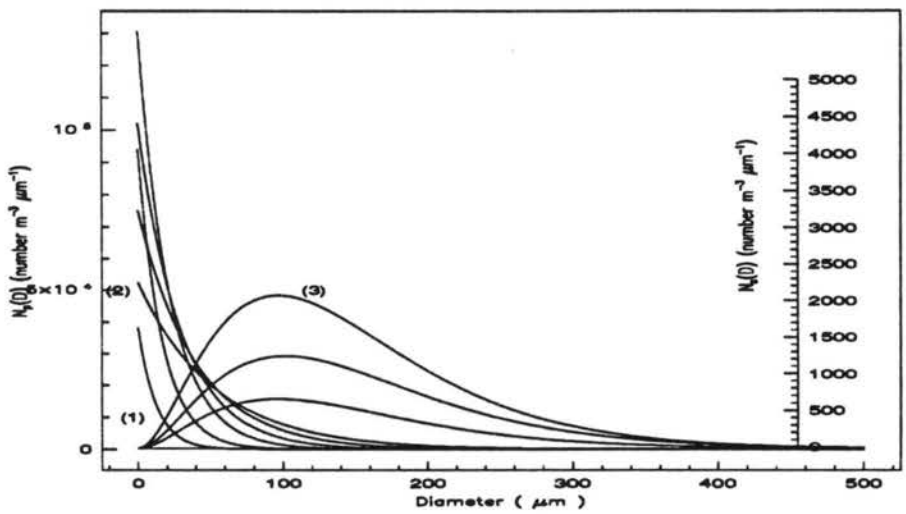

Figure 5.16: Evolution of the ice spectra for hexagonal plates, model ascent. (1): Pristine ice at model time step 61, (2): Pristine ice at model time-step 600.

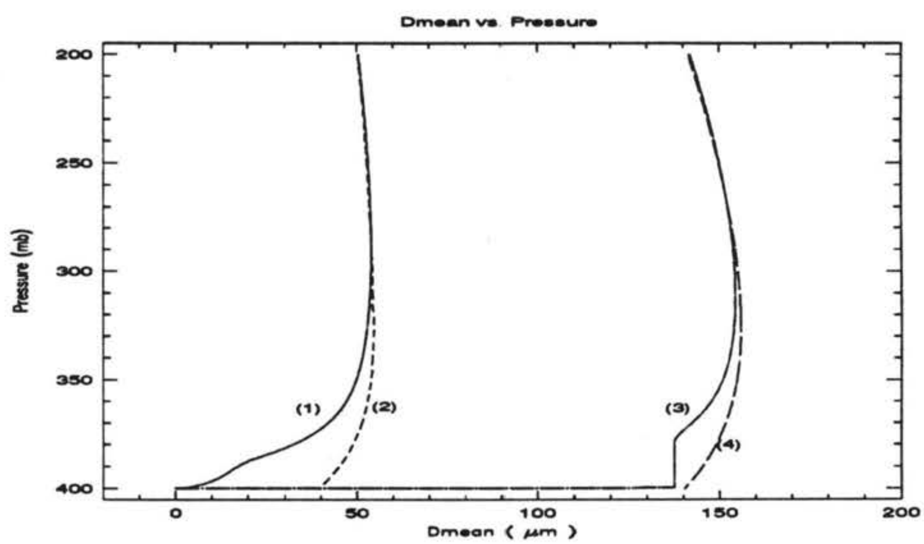

Figure 5.17: $\bar{D}$ vs. Pressure. Ascent and descent profiles for pristine ice are denoted by (1) and (2) respectively. Ascent and descent profiles for snow are denoted by (3) and (4) respectively.

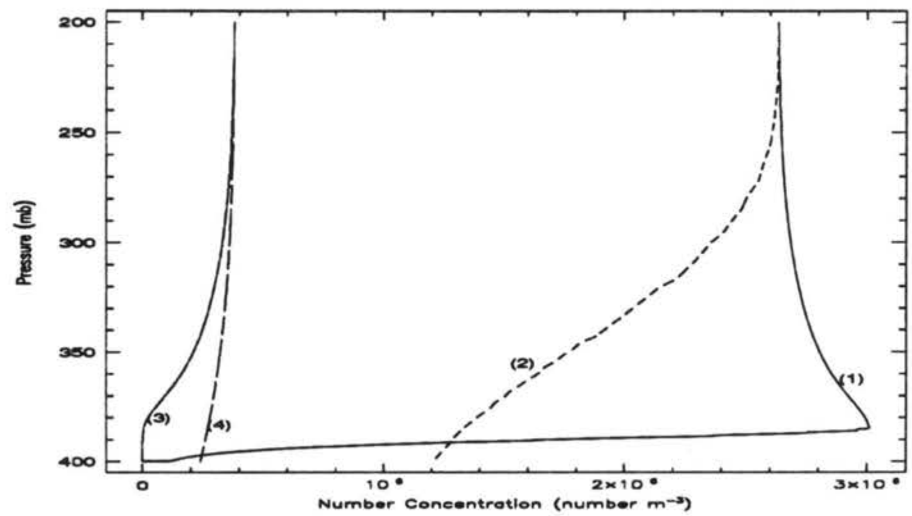

Figure 5.18: Number concentration vs. Pressure. Ascent and descent profiles for pristine ice are denoted by (1) and (2) respectively. Ascent and descent profiles for snow are denoted by (3) and (4) respectively.

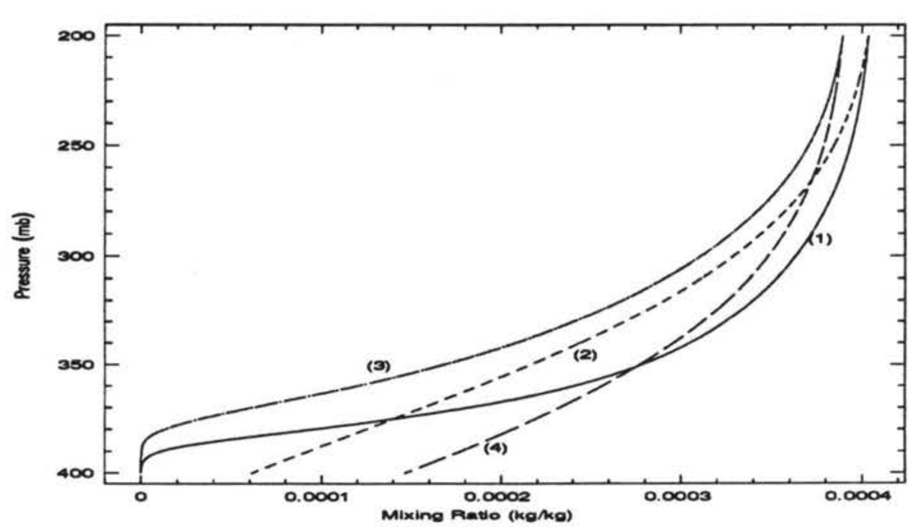

Figure 5.19: Ice mixing ratio vs. Pressure. Ascent and descent profiles for pristine ice are denoted by (1) and (2) respectively. Ascent and descent profiles for snow are denoted by (3) and (4) respectively.

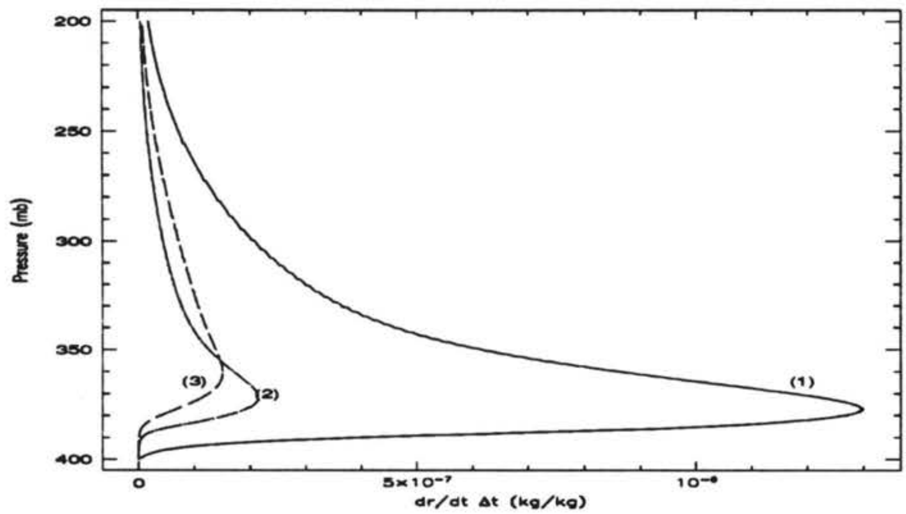

Figure 5.20: $dr/dt\Delta t$ vs. Pressure for model ascent. Mass growth of the pristine ice and snow distributions are denoted by (1) and (3) respectively. Mass flux from pristine ice to snow is denoted by (2).

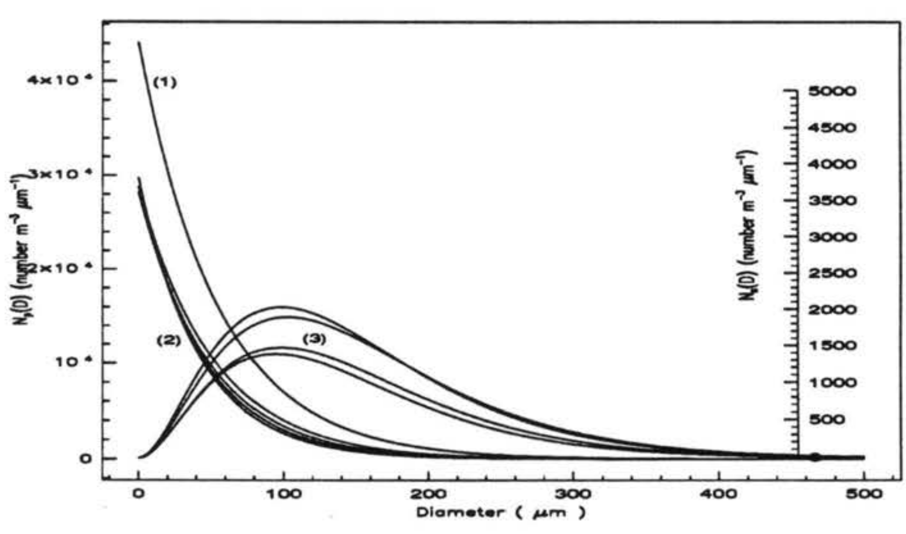

Figure 5.21: Evolution of the ice spectra for hexagonal plates, model descent.

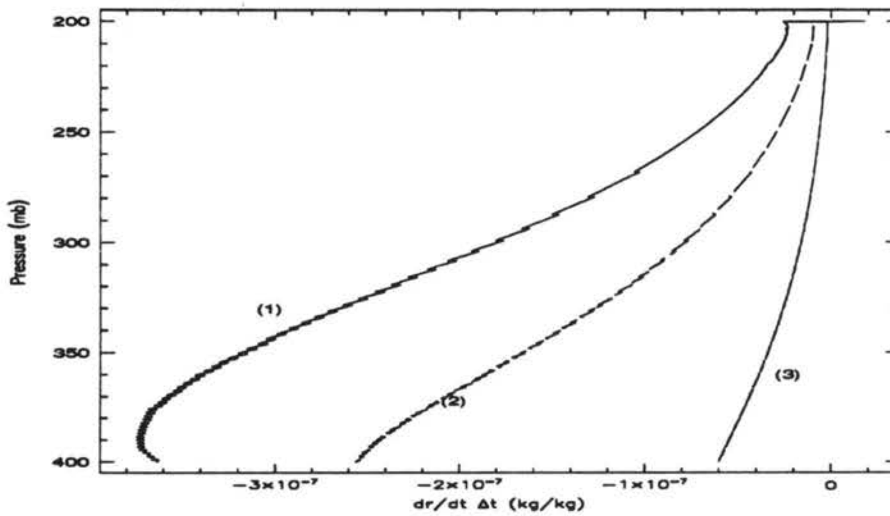

Figure 5.22: $dr/dt\Delta t$ vs. Pressure for model descent. Mass loss due to evaporation of the pristine ice and snow distributions are denoted by (1) and (2) respectively. Mass flux from snow to pristine ice is denoted by (3).

Figure 5.16 shows the evolution of the ice spectra for hexagonal plates with T=243 K and $r_v = 0.7$ g/kg. As with the simulations given above the inital distribution is narrow with the largest concentrations associated with the smallest diameters. As the parcel ascends, the distribution of pristine ice broadens as it grows due to vapor deposition. After 200 model time-steps the snow distribution becomes noticable, however, it is still much smaller and broader than the pristine ice distribution.

Note that the snow distribution does not broaden much during model ascent. This is also noted in Figure 5.17, the profile of $\bar{D}$ with pressure. The reasons for this will become apparant when comparisons between this simulation and Case 2 are discussed.

Examination of the number concentration profile (Figure 5.18) shows pristine ice increasing quickly during ascent while snow concentrations never reach very large values. The profiles of mixing ratio with respect to pressure, Figure 5.19, show that the masses of pristine ice and snow are comparable during ascent with pristine ice always having the larger value.

The mass growth of the pristine ice and snow distributions are shown in Figure 5.20. The mass growth of the pristine ice distribution is quite large (labeled (1) in the figure) when compared to the mass growth of the snow distribution. This is due to the interactions between the high number concentration of pristine ice and the growth equation for hexagonal plates and will be discussed in the next section. Also, note that the mass added to the snow distribution by the transfer of pristine ice is larger than the actual growth of the snow distribution by vapor deposition during the first 45 mb of ascent.

During model descent the pristine ice distribution (shown in figure 5.21) slowly narrows as does the snow distribution. The narrowing of the distributions is much less than was examined for the case of needle crystals. This will be examined in the next section.

Comparison of the model results

Intercomparisons between the results for needle crystals, Cases 1 and 2, and of the differing crystal habit simulations, Cases 2 and 3 are made in this section. For cases 1 and 2, the prominent difference in the two simulations is the faster broadening of the $\nu = 3$ case as compared to the $\nu = 1$ case; note the larger mean diameters attained for snow in Figure 5.4 as compared with Figure 5.14, the $\nu = 3$ case reaches mean diameters approximately 200 μm larger. The reason for the larger distribution broadening has to do with the vapor depositional growth of the distributions. According to (4.54), the vapor depositional growth of a given distribution is a function of ν,

$$\dot{r} = \frac{\Psi}{\rho_a} D_n N_t \frac{\Gamma(\nu+1)}{\Gamma(\nu)}. \tag{5.10}$$

Writing the gamma function fractions for $\nu = 1$ and $\nu = 3$ gives

$$\frac{\Gamma(1+1)}{\Gamma(1)} = \frac{1!}{0!} = 1 \tag{5.11}$$

$$\frac{\Gamma(3+1)}{\Gamma(3)} = \frac{3!}{2!} = 3. \tag{5.12}$$

Thus, for a distribution with $\nu = 3$ the vapor depositional growth will be 3 times as large as for a $\nu = 1$ distribution. Since the transfer of mass and number concentration is a function of the crystal growth rates, mass will be transfered at a larger rate for the $\nu = 3$ pristine ice distribution. This larger mass transfer rate is shown by comparison of Figures 5.5 and 5.13. Since more mass and number concentration is transfered to the snow distribution, and since dm/dt is written as a linear function of D, the snow distribution for the $\nu = 3$ case will grow faster and broaden more.

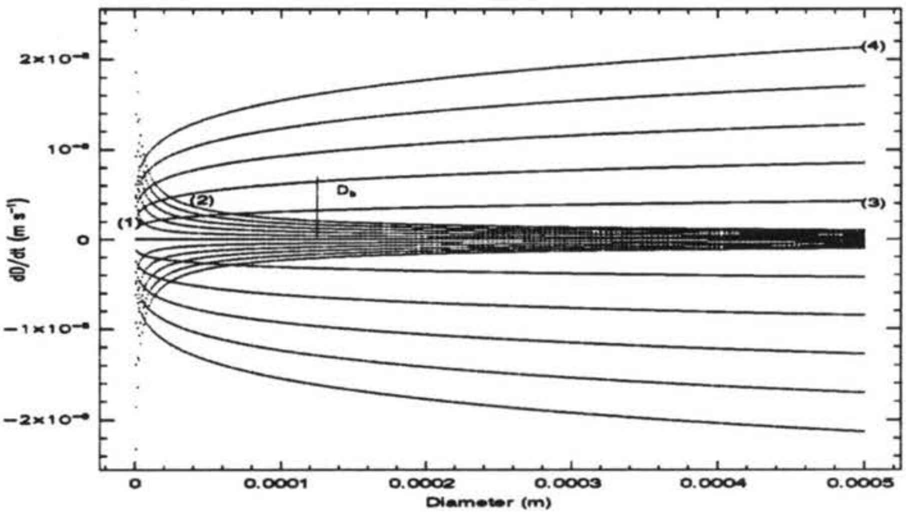

Figure 5.23: dD/dt vs. D for various values of S_i. (1)-(2) are curves for hexagonal plates and (3)-(4) are for needles. The range of S_i that these curves represent are 1.1 → 1.5 in 0.1 increments of S_i. Curves for the range 0.5 → 0.9 are also plotted

Upon comparison of the distribution evolution for cases 2 and 3 (Figures 5.9 and 5.16) it is apparent that the snow distribution composed of hexagonal plates does not broaden as much as the needle crystals. Figures 5.14 and 5.17 show the mean diameters for the needle crystals reach much larger maximum values than do the hexagonal plates. The number concentrations of pristine ice reach much larger values and stay consistently higher for needle crystals than for hexagonal plates. Also, note the differences in the mass growth and transfer values between the two different habits. The vapor depositional growth of pristine ice needles is much less than pristine ice hexagonal plates, while snow needle vapor depositional growth rates are much larger than snow hexagonal plates. In fact, during the first 55 mb of the parcel ascent, the vapor depositional growth of the snow hexagonal plates is less than the mass transfered from the pristine ice distribution. This has important consequences when trying to explain the differences in the two simulations.

The differences between these two simulations can be explained by examining the figures of the mass growth rates hinted at above (Figures 5.16 and 5.20). As stated above, for the hexagonal plates, more mass is added to the snow class by transfer from pristine ice than by vapor depositional growth during the first 55 mb of the model ascent. This keeps the snow distribution narrow, as noted by the minimum value of the snow mean diameter in Figure 5.17. As the model ascent continues, the mass transfer becomes less than the vapor depositional growth of the distribution, however the two processes are still quite comparable and the snow distribution does not broaden much. For the snow distribution composed of needle crystals, distribution broadening is quite fast and can be seen by noting the larger vapor depositional growth rates of the snow distribution as compared to the mass transfer rates shown in Figure 5.20.

These explanations are satisfactory when examining the broadening of the distributions. They do not, however, explain why the mass growth of the pristine ice distribution for hexagonal plates is greater than for the needle case, why the mass transfer rates from pristine ice to snow is lower for hexagonal plates than for needles, and why the vapor depositional growth rate of snow is less for hexagonal plates than for needles. To answer these questions, the growth of needle crystals and hexagonal plates (dD/dt) are plotted over a range of diameters for various saturations over ice in Figure 5.23. Recalling that the equation for dD/dt is a function of D like

$$dD/dt \simeq D^{(2-\beta)} \tag{5.13}$$

and that $\beta = 1.8$ for needles and $\beta = 2.5$ for hexagonal plates, respectively. Thus,

$$dD/dt \simeq D^{-0.2} \text{for needles} \tag{5.14}$$

and

$$dD/dt \simeq D^{0.5} \text{for hexagonal plates.} \tag{5.15}$$

This is the tendency shown in Figure 5.23 for needles and hexagonal plates. Note that for needles, the growth rate is larger for large particles than for smaller particles. This explains the larger growth of the snow distribution by vapor depositional processes than by mass and number concentration transfer from the pristine ice distribution; mass and number transfer are functions of the vapor depositional growth equation. For the hexagonal plate crystals, the vapor depositional growth is largest for the smaller crystals, thus mass and number concentration transfers from the pristine ice distribution to snow can be as large or larger than the vapor depositional growth of the snow distribution itself. This is shown in the slow broadening of the snow distribution composed of hexagonal plates given above.

These routines were implemented into the microphysical module of the RAMS model. The next chapter is dedicated to two-dimensional sensitivity studies of cirrus clouds, where model tests of this scheme and both the homogeneous and heterogeneous nucleation schemes are given.

Chapter 6

THE NOVEMBER 26, 1991 FIRE II CIRRUS EVENT: OBSERVATIONS

This chapter is dedicated to an analysis of the cirrus event that occured on the 26th of November, 1991. A discussion of the development of the cloud system and it's observed dynamical processes will be discussed in the first section. The second section will be taylored towards a description of the observed microphysical fields derived from lidar, radar, and aircraft measurements. The purpose of this is to identify the physical processes that produced the cirrus clouds that we are attempting to simulate and to give some information upon which to draw conclusions as to how well the two-dimensional version of RAMS faired in simulating the cloud system. Since we are interested in the sensitivity of the model to the chosen physical parameters (e.g. crystal habit, distribution shape parameter, nucleation scheme etc...) these results will also serve as a basis for the examination of sensitivity of the physical parameters.

6.0.3 Cirrus cloud development and dynamics

The cirrus cloud system that developed on the 26th of November, 1991 developed in the region of a mobile upper tropospheric trough that was associated with the dynamics of the exit region of an upper tropospheric jet streak. The upper level analysis (300 mb) of heights/isotachs (Figuer 6.1) for 0000 UTC on the 26th of November shows a jet streak with maximum winds of up to 110 knots centered over the northwestern portion of the United States. By 1200 UTC (Figure 6.2) the right, eastern exit region of the jet and an associated upper level trough entered the western part of Kansas. The system was first picked up by lidar and radar (Intreiri et al., 1993) at around 1800 UTC. By about 1930 UTC the base of the cirrus deck descended to about 6km retaining its top at around 9 km. After about 2100 UTC the cloud base descended to between 2 and 3 km.

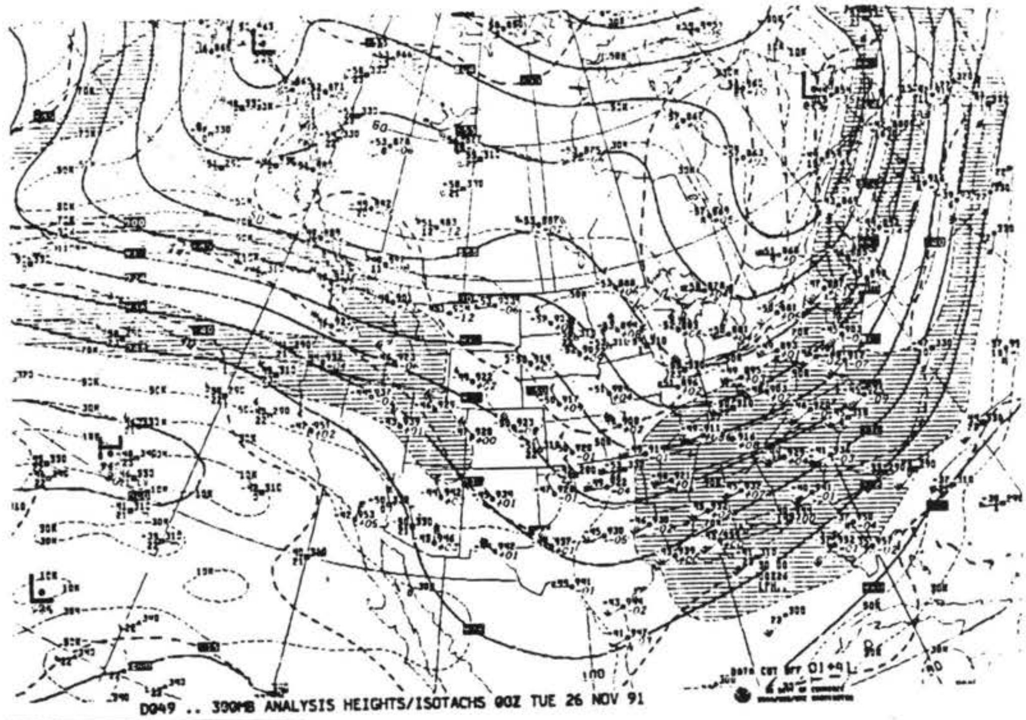

Figure 6.1: 300 mb analysis of heights/isotachs for 00 Z, November 26, 1991.

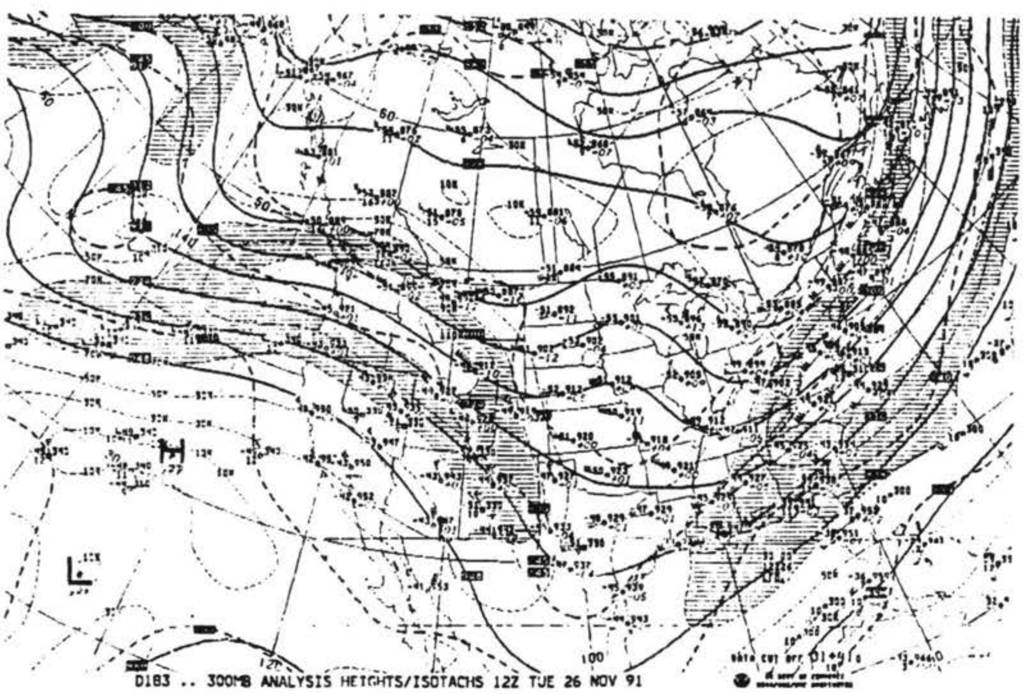

Figure 6.2: 300 mb analysis of heights/isotachs for 12 Z, November 26, 1991.

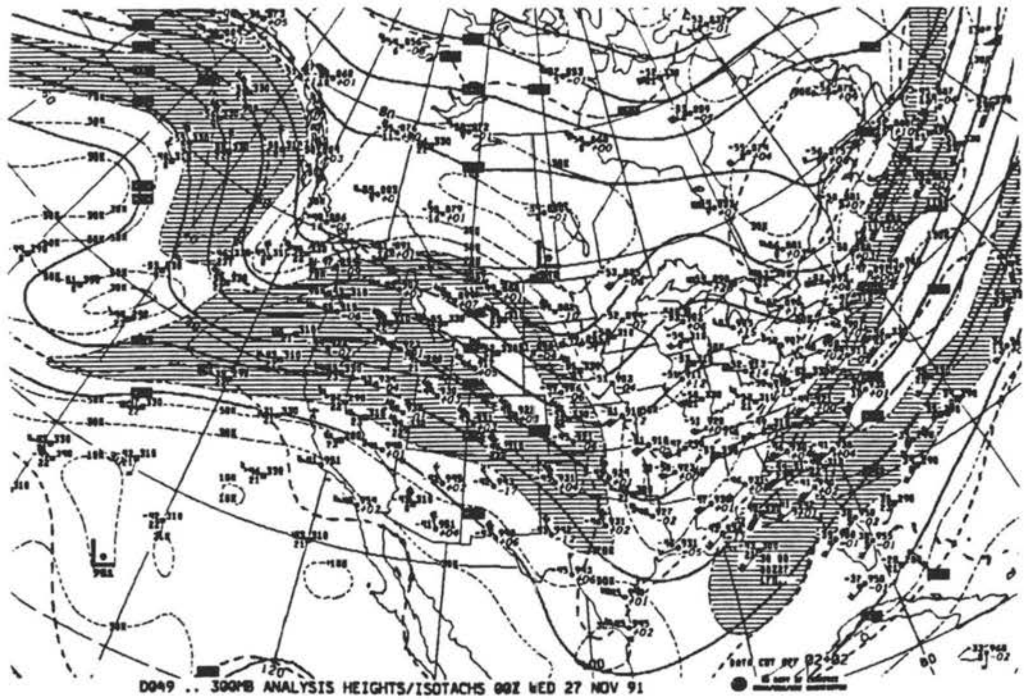

Figure 6.3: 300 mb analysis of heights/isotachs for 00 Z, November 27, 1991.

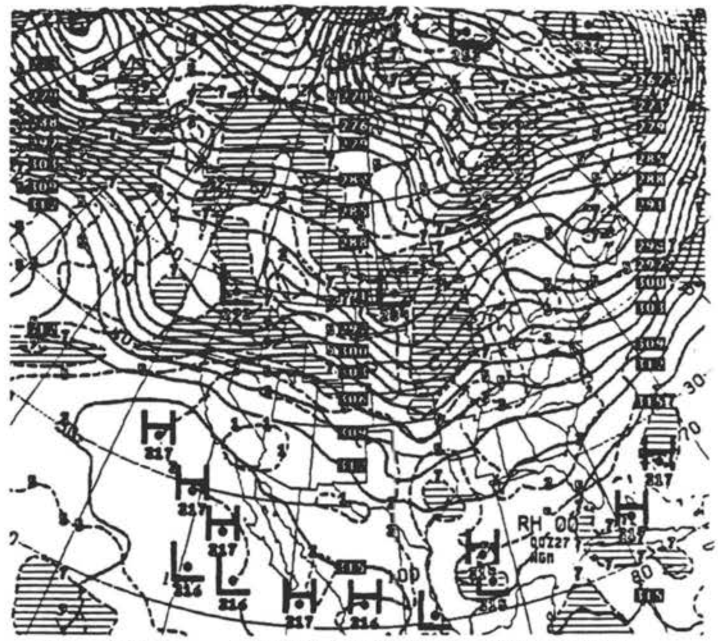

Figure 6.4: 700 mb NGM analysis of heights/RH for 00 Z, November 27, 1991.

Figure 6.3 shows the jet at 0000 UTC on November 27th; the right, eastern exit region of the jet is centered over portions of eastern Kansas, and the trough is moving out. The analysis of the NGM on 0000 UTC of the 27th shows 70 % relative humidity at 700 mb (about 3 km); the cloud base was at this level at this time (Figure 6.4).

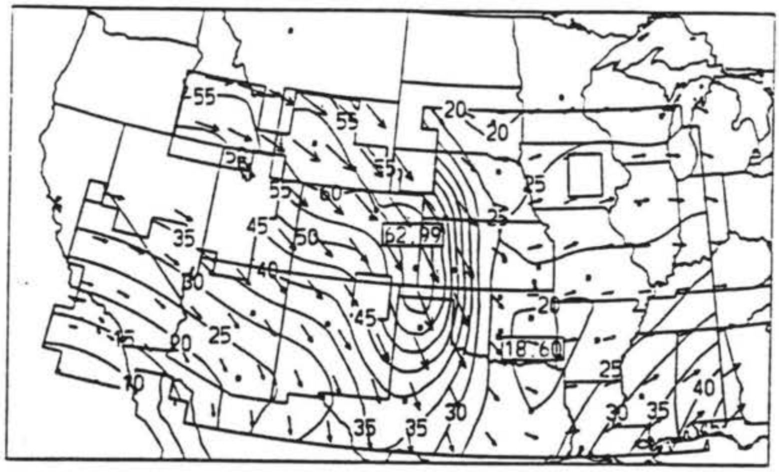

Figure 6.5: Wind speeds contoured at 10km on Nov. 26, 1991 (Mace et al., 1993).

Figure 6.5 shows the contours of wind speeds at 10 km (Mace et al. 1993) at 2100 UTC; the extent of the jet streak from South Dakota to northeastern Texas is evident. Mace et al. (1993) attributed the formation and maintenance of the November 26th cirrus cloud system to a difluent trough associated with the right, eastern edge of the jet streak shown in Figure 6.5. The authors noted that the geopotential height field exhibited a tilt in the upper level trough from the southeast below to the northwest at higher altitudes. This was noted as resembling a upper level jet front propagating through a synoptic scale baroclinic wave; both barotropic amplification of the front through the tilt in the height field and baroclinic amplification by cold advection were tell-tail signs of this. The upper level front motivated the formation and eastward propagation of the cirrus event as the dynamics of the system moved and intensified. This is noted in the vorticity field from Mace et al. (1993) (Figure 6.6) which shows the motion and intensification of the cyclonic vorticity pattern between 1800 UTC and 2100 UTC. These fields were constructed by the authors using both radiosonde and wind profiler data.

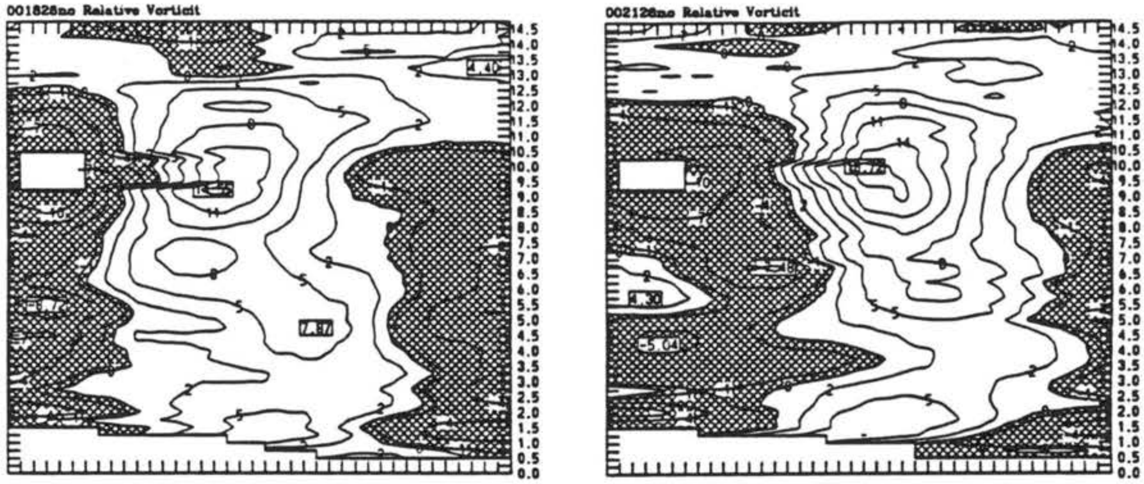

Figure 6.6: Vertical vorticity cross-sections for 18 UTC (a) and 21 UTC (b) on the 26th of November, 1991. Positive values of the relative vorticity are shaded; contours are in intervals of $10^{-5}\ s^{-1}$, (Mace et al., 1993).

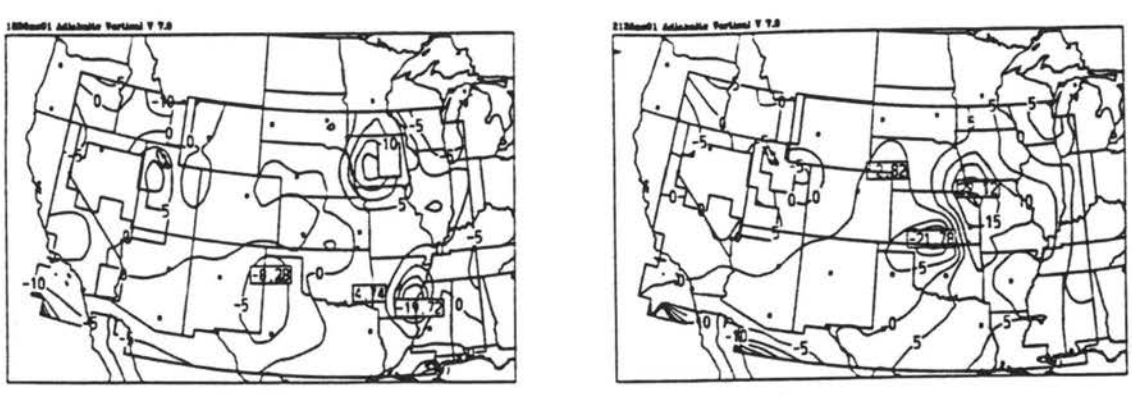

Figure 6.7: Vertical velocities from adiabatic flow for 18 and 21 UTC (a and b respectively). Velocities are in $cm\ s^{-1}$, (Mace et al., 1993).

Vertical motions were diagnosed by Mace et al. (1993) from the first law of thermodynamics assuming adiabatic flow. The 1800 UTC vertical motion field from their results at the 7.5 km level (Figure 6.7) show weak vertical motions over Coffeyville of around 0.01 $m\ s^{-1}$. Similar fields were constructed for the 2100 UTC data and shows the stronger vertical motions induced by the intensifying upper level trough (up to about 0.15 $m\ s^{-1}$).

Gultepe et al. (1993) used aricraft and radar measurements to derive some of the dynamical properties of the cirrus clouds that were observed during the Novemer 26-26 and the December 5-6 events. Their results showed that the vertical velocites observed in the cirrus layers were between a few hundreths of a meter per second and 1 $m\ s^{-1}$. Within the cirrus generating cells vertical motions were on the order of 1 $m\ s^{-1}$. The authors compared the fluxes of momentum and heat on the small (cloud) scale to the mesoscale and find that there is much momentum and heat transport being accomplished by the cloud-scale eddies.

6.1 Microphysical observations

A topic of general interest in the observational study of cirrus clouds (and one that needs to be parameterized correctly in numerical models) is the dominant crystalline habit in cloud. Heymsfield et al. (1993) used 2D-C probe and ice replicator data to examine crystalline shapes of the November 26 cirrus case. The 2D-C probe creates shadowed images of particles that pass through its beam. The 2D-C probe is known to undercount particles with sizes less than 70 μm while the ice replicator tends to overpredict the sizes of particles greater than 150 μm in size. Figure 6.8 shows the data from the probes. The 2D-C probe shows bullet and rosette shaped crystals and some, irreguarly shape crystals. The ice replicator data shows many small spherical-shaped crystals, irregular shaped crystals, and some bullets and rosettes.

Arnott et al. (1993) used these (2D-C probe and ice crystal replicator) data to derive spectral information of the ice particel size distributions in the cirrus clouds. Their results showed that a bimodal spectrum of ice particles can exist in cirrus clouds (see Figure 6.9).

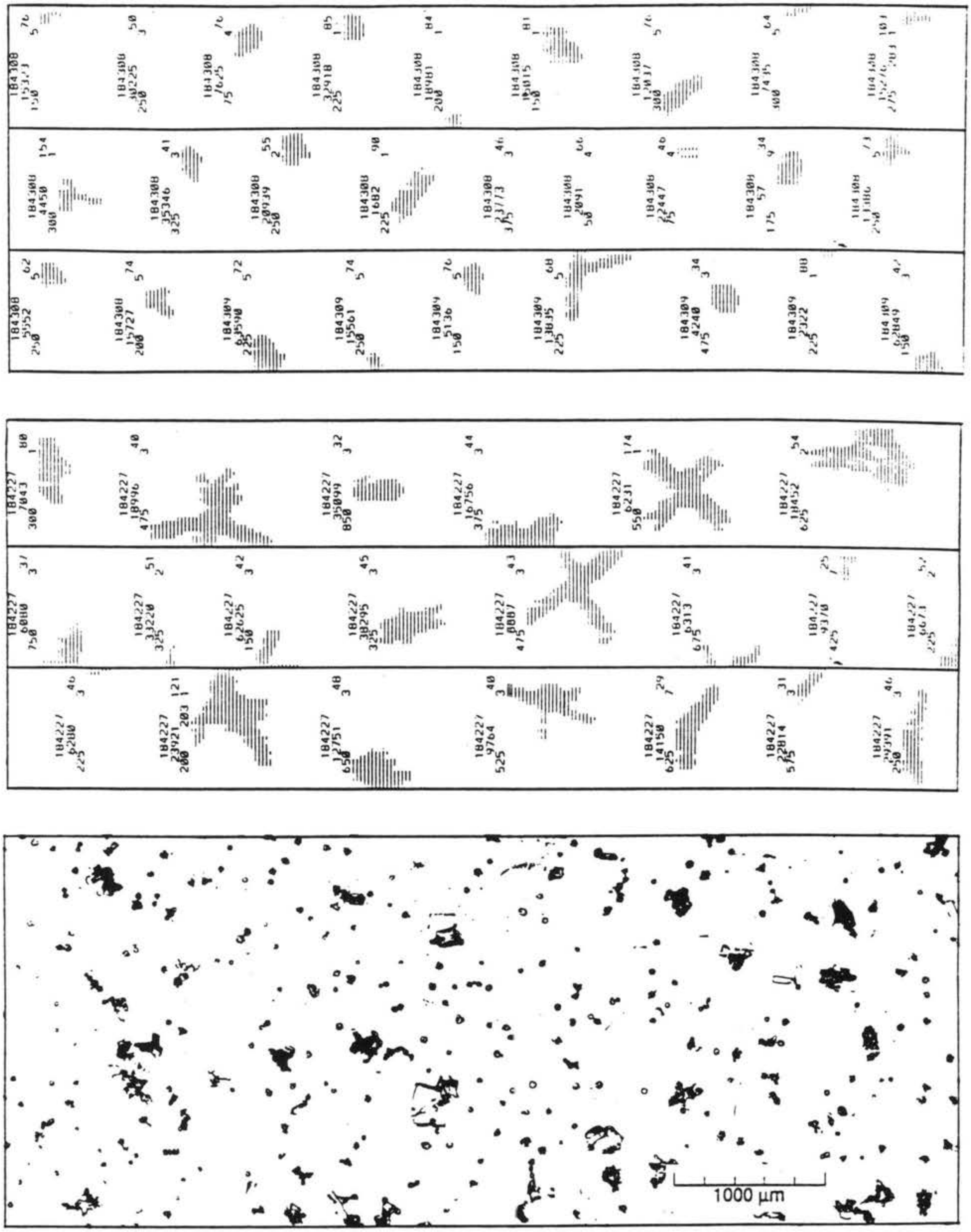

Figure 6.8: 2D-C probe and ice replicator measurements (a and b respectively) show crystalline habits that existed during the November 26 cirrus event (Heymsfield et al., 1993).

The analysis showed that there was a delination between the distribution of smaller particles and the distribution of larger particles; this delineation occured between about 120 and 190 μm.

Matrosov et al. (1993) retrieved cirrus cloud microphysical information by using doppler radar and and IR radiometer techniques.

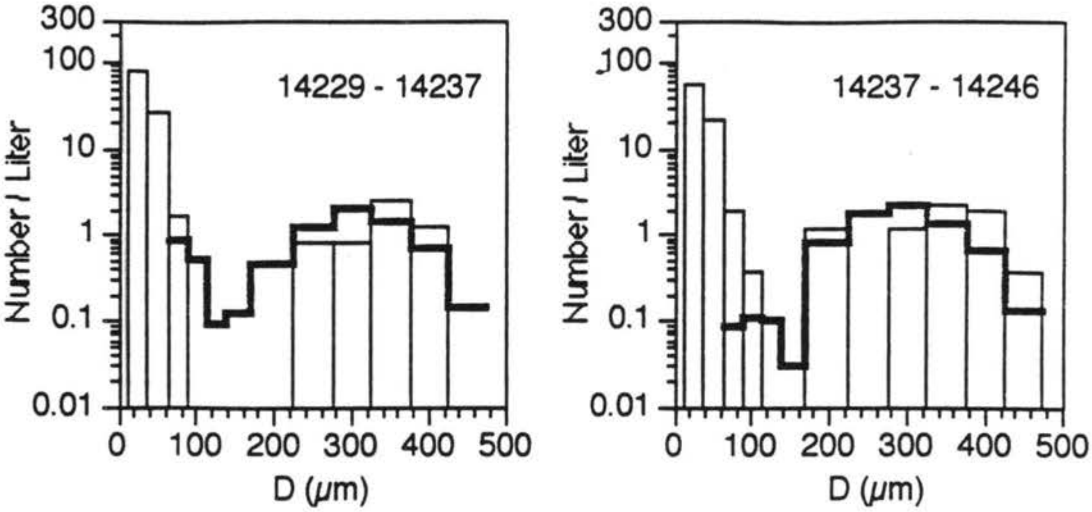

Figure 6.9: Spectral representation of the 2D-C probe (thick line) and ice replicator (thin line) data. A bimodal spectrum is evident (Arnott et al., 1993).

Their results, shown in Figure 6.10 and 6.11, show the general trend observed in the cloud layer; the cloud, initially thin, at about 8-9 km, dropping cloud base to about 6 km by 1900 UTC while maintaining its top at around 9 km. Concentrations near cloud top are in excess of 1000 l^{-1} while concentrations near cloud base are low (about 2.7 l^{-1}). Associated with the higher concentrations, these results showed particle median diameters of about 50 μm while the low concentrations at cloud base were associated with larger median diameters (about 400 μm) as one would expect. These general results were also shown by Intrieri et al. (1993). Their data (shown in Figure 6.12) showed concentrations up to 1000 l^{-1} at cloud top; associated with smaller diameters (around 30 μm) and usually smaller IWC. Concentrations near cloud base were low (about 101 l^{-1}) and associated with larger sizes (200 μm) and usually high IWC (up to 0.046 gm^{-3}).

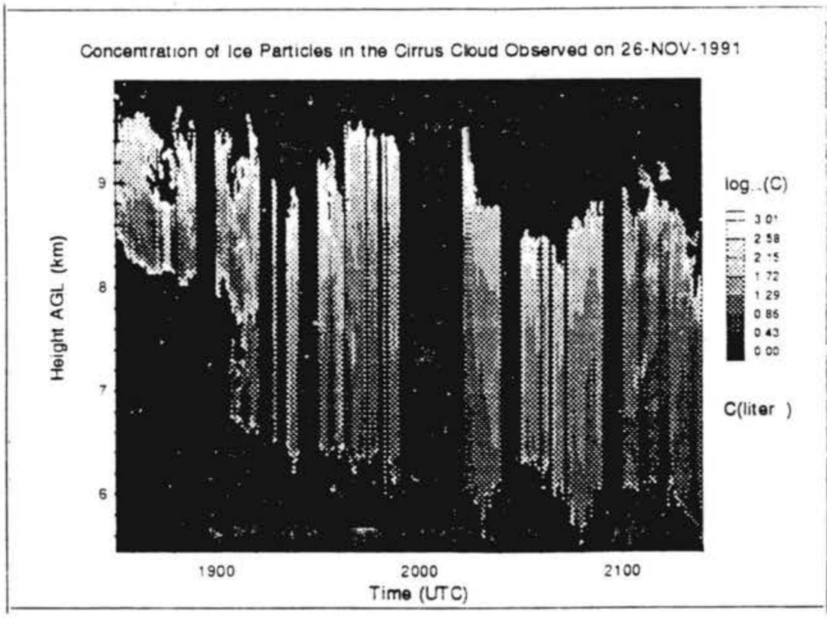

Figure 6.10: Time-height cross-section of retrieved ice crystal concentrations; in log(number l^{-1}) (Matrosov et al., 1993).

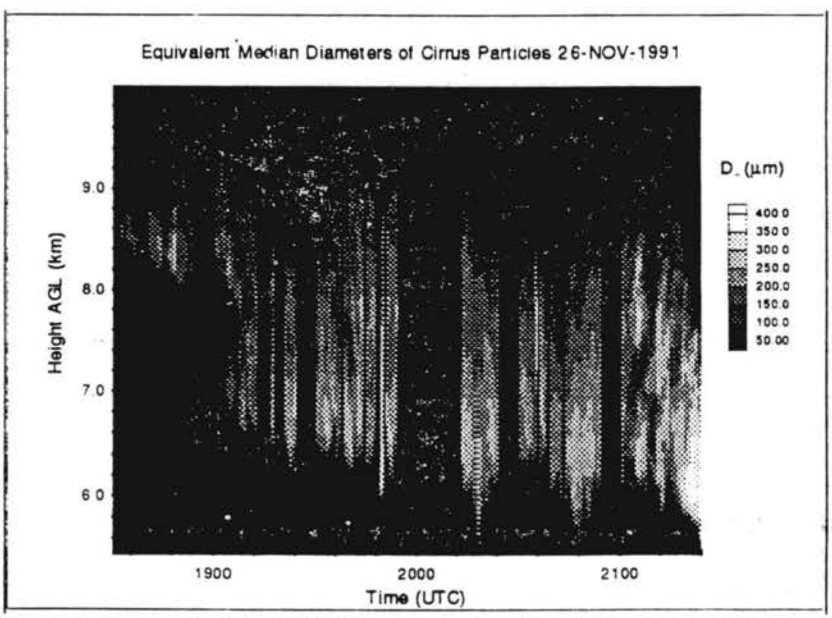

Figure 6.11: Time-height cross-section of retrieved ice crystal median diameters in μm (Matrosov et al., 1993).

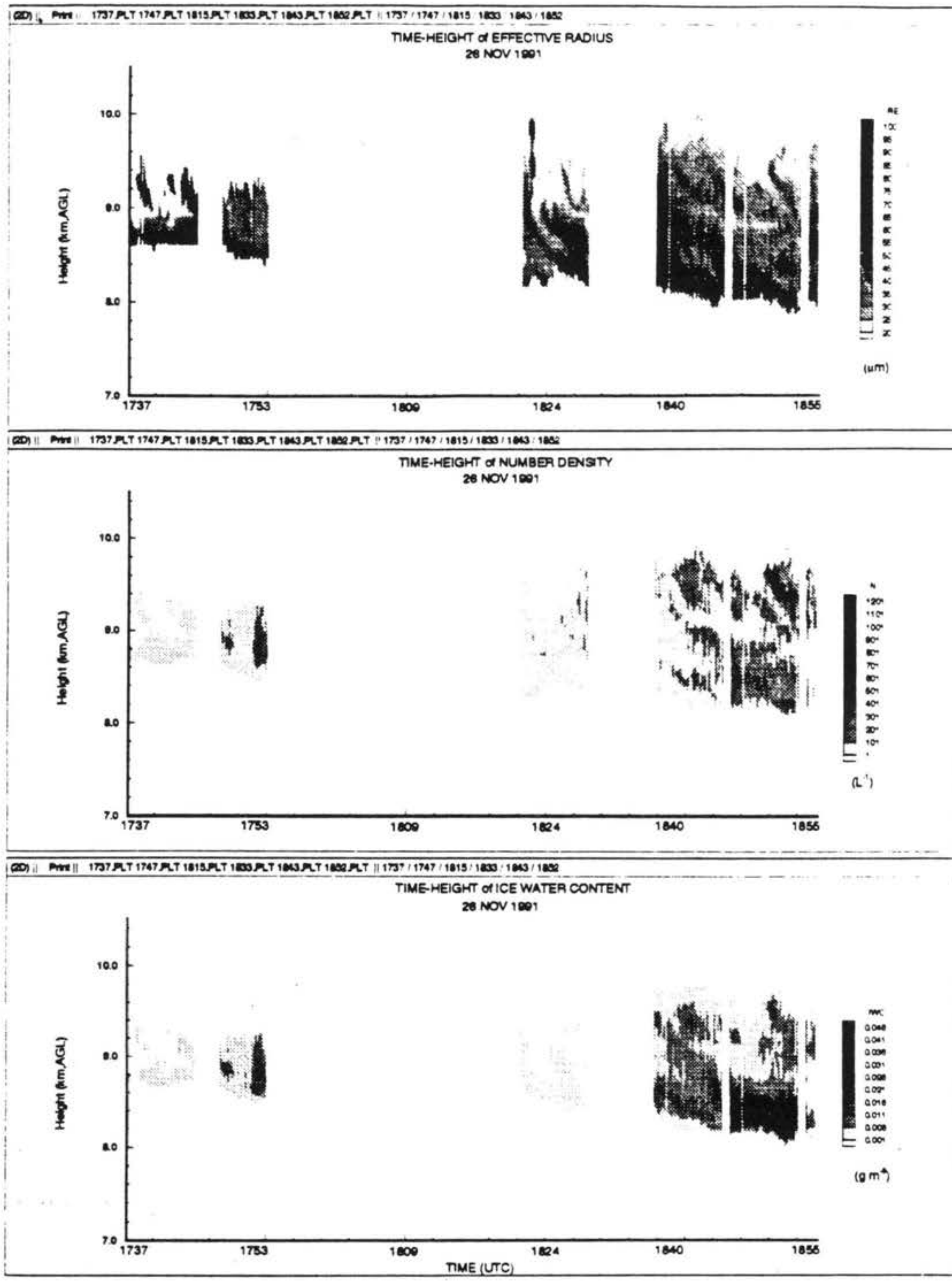

Figure 6.12: Time series of retrieved effective radius (a), number concentration (b), and IWC (c); values are in μm, number l^{-1} and $g\ m^{-3}$ respectively. (Intrieri et al., 1993).

Uttal et al. (1993) used radar data to define the upper and lower cloud boundaries observed during the November 26 cirrus case. Figure 6.13 shows a time-series plot of the radar echo boundaries of the cirrus cloud system. The cloud was initally thin, with a thickness of only about 1 km and a cloud top around 9 km. After about 19 UTC the cloud base dropped to 6km, and after about 21 UTC the cloud base dropped to around 3 km; the whole time the cloud top stayed at around 9 km.

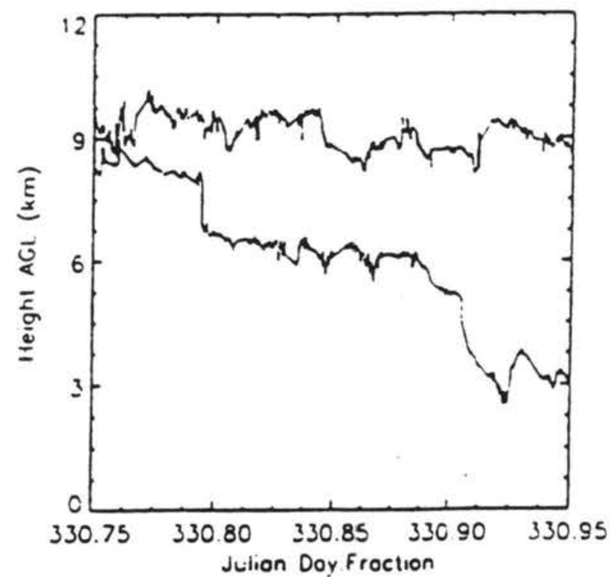

Figure 6.13: Radar echo boundaries of the Nov. 26 cirrus event (Uttal et al., 1993).

The next chapter describes the two-dimensional modeling study of this cirrus event. Variations in crystal habit, distribution shape, nucleation parameters, both single and double moment predictions, and radiation parameterizations are used to study the effects of these variations on the simulations of cirrus clouds with the RAMS modeling system.

Chapter 7

TWO-DIMENSIONAL SENSITIVITY TESTS WITH RAMS

This chapter is dedicated to two-dimensional simulations of the November 26, 1991 FIRE II cirrus case. The model was set up for the two dimensional simulations with 20 grid points in the east-west direction and a grid spacing of 10 km. In the vertical, the model contains 74 levels starting with 1500 m grid spacing at the ground, shrinking this to 50 m spacing at cloud level, and then strectching this spacing back to 1500 m above cloud. The model was initialized with a sounding that is representative of the atmospheric structure that occured on that day. As was pointed out by Heymsfield et al. (1993), the moisture profile derived from rawindsondes exhibited up to 20 % in cloud. Figure 7.1 shows the Heymsfield et al. (1993) data from the King Air and Saberliner flights in cloud. The model was run for 6 hours during the period of active cirrus on November 26 (about 1800 UTC to 2400 UTC).

As one can see, the relative humidity at cloud levels was significantly below that measured by the aircraft; it was in fact, lower than ice saturation at all levels. Because of this, we opted to modify our sounding between the 6 and 10 km levels in order to better conform with the atmospheric data at those levels.

The model was run using various properties of the two moment prediction scheme in order to understand the effects of these new parameterizations on the simulations of a cirrus cloud system. The following heirarchy was adheared to for the simulations: First, a control simulation was conducted and compared to observations of the case given in Chapter 6, the next section is dedicated to this simulation; second, various simulations were conducted

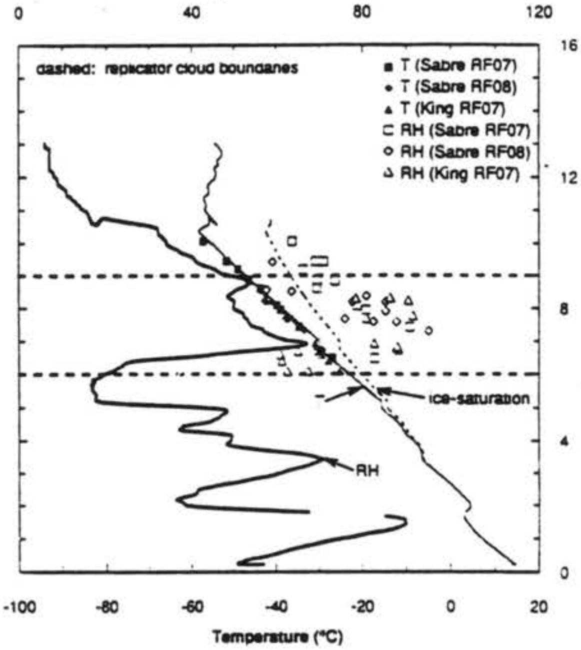

Figure 7.1: King Air and Saberliner data in cloud for the November 26 cirrus case. Upper abscissa is RH (%), ordinant is height (km). Note the larger RH values measured by the probes as compared to the rawindsonde sounding.

in which certain aspects of the two moment microphysical parameterization were changed, and are presented in Section 7.2. Table 7.1 contains a summary of the simulations and the variatons in parameters that were conducted.

The control simulation is compared to observations, thus all relevant parameterizations are turned on. The other simulations serve as sensitivities to the control. Simulations NN1 and PN1 test model sensitivity to changes in the assumed habit. Variable habits are allowed during model simulations but are not considered here since the idea is to test the sensitivity of these parameters. Simulations NN3 and RN3 test the effect of a different distribution shape parameter (ν) for snow and aggregates on the model results. The simulation RSM was done using the single moment prediction scheme in the model, RNR was done without the model radiative parameterization and shows the importance of radiative effects on cirrus simulations, RNH was done without homogeneous nucleation and RCIN was done with a pertubed ice nuclei profile.

Table 7.1: Simulations				
Test	Two Moment	Snow Shape	Habit	Radiation
Control	yes	1	Rosettes	on
NN1	yes	1	Needles	on
PN1	yes	1	Plates	on
NN3	yes	3	Needles	on
RN3	yes	3	Rosettes	on
RSM	no	1	Rosettes	on
RNR	yes	1	Rosettes	off
RNH	yes	1	Rosettes	on
N5RH	yes	1	Needles	on
RCIN	yes	1	Rosettes	on

Table 7.1: Simulations, continued		
Test	Homogeneous Nucleation	Ice Nuclei Profile
Control	on	tapered
NN1	on	tapered
PN1	on	tapered
NN3	on	tapered
RN3	on	tapered
RSM	on	tapered
RNR	on	tapered
RNH	off	tapered
N5RH	on	tapered
RCIN	on	perturbed

Table 7.1: Conducted simulations. Control simulation is compared to observations. Other simulations include variations of model parameters. For example, NN1 (Needles ν =1) and PN1 (Plates ν =1) are done to check model dependence on crystal habit.

The simulation N5RH was done with an increase of 5 % in the sounding RH values in cloud (from 7.5 to 9 km), showing the importance of correct sounding values in the simulations of these systems.

7.1 Control Simulation and Comparison with Observations

The control simulation was done with the full two moment prediction scheme, considering rosette crystals to be dominant in the cloud. Rosettes were chosen since, as is shown in Figure 6.8, many of the crystals observed in cirrus were of irregular shapes or were rosettes.

Figure 7.2 shows the total ice mixing ratio after 2 hours of simulation. Maximum values are upwards of 0.55×10^{-2} g/kg and cloud base has descended to about 5 km.

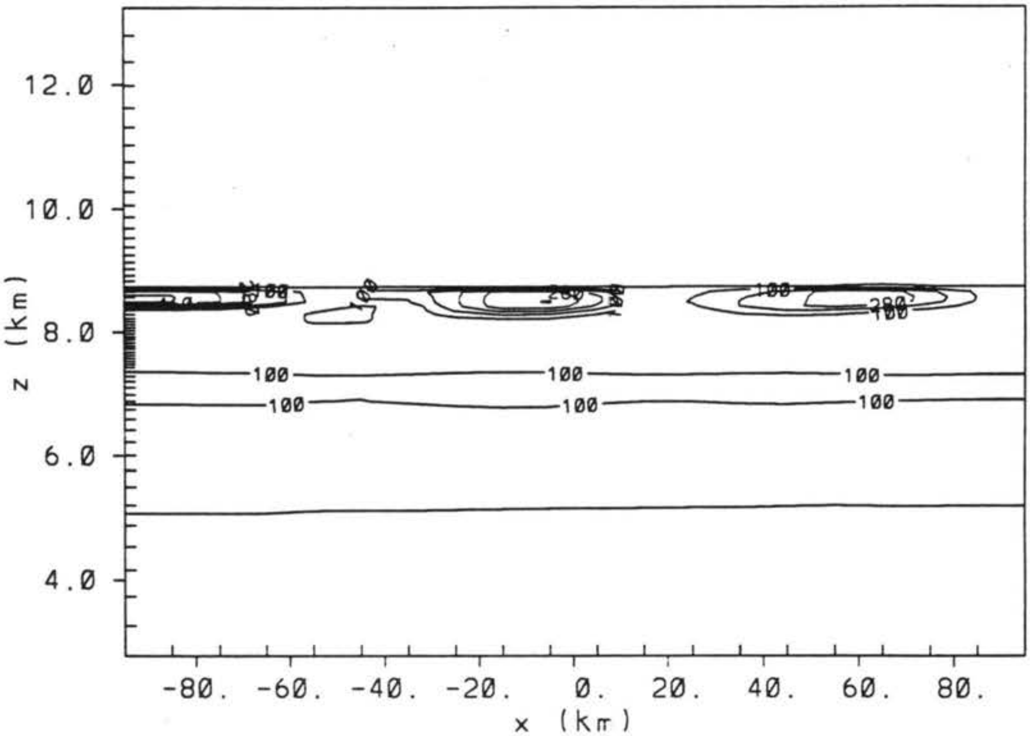

Figure 7.2: Total Ice Mixing Ratio for the RN1 simulation. Maximum contour, 0.55E-5 kg/kg; Smallest contour, 0.1E-6 kg/kg; Contour interval, 0.9E-6 kg/kg.

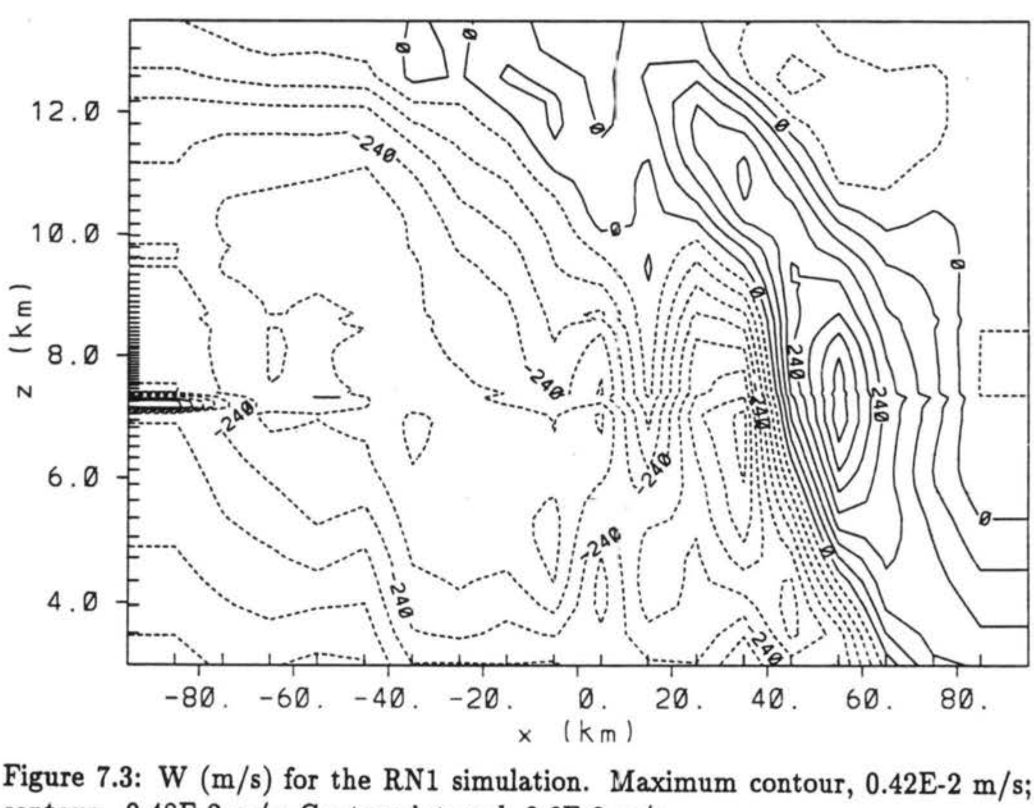

Figure 7.3: W (m/s) for the RN1 simulation. Maximum contour, 0.42E-2 m/s; Smallest contour, -0.48E-2 m/s; Contour interval, 0.6E-3 m/s.

Figure 7.3 shows maximums in updraft and downdraft velocities near cloud base which are on the order of 0.42×10^{-2} m/s (-0.48×10^{-2} m/s).

Figures 7.4-7.15 show the relevant ice fields for the cirrus simulations after 5 hours of model time. Figure 7.4 shows the pristine ice mixing ratio fields; maximums in mixing ratio values are up to 0.27×10^{-1} g/kg at mid-cloud levels. Cloud top is near 9.5 km while small values of pristine ice exist down to 6 km. Pristine ice concentrations, Figure 7.5, have maximum values of up to 960 l^{-1} near cloud top, dropping of to 10 l^{-1} near 7.5 km. As one would expect (Figure 7.6) the larger concentrations and smaller masses near cloud top are associated with smaller crystal sizes, while the smaller number concentrations near and below 7.5 km are associated with larger sizes. The snow mixing ratio and number concentraion values (Figures 7.7 and 7.8) show similar structure and have maximum values near the 6.5 km level (0.8×10^{-2} g/kg and 9 l^{-1}). Large values of the size of the snow crystals are associated with the low number concentrations and masses near cloud base (Figure 7.9). These values are in good agreement with the lidar and radar data presented in Figures 6.10 and 6.11. These observations show high number concentrations (up to 1000 l^{-1}) with small crystal sizes (around 20-40 μm) and masses. Smaller concentrations (down to 3 l^{-1}) and larger sizes (up to 400 μm) associated with cloud base seem to compare well with the snow and the aggregate model results described below.

Figures 7.10-7.12 show the contours of the aggregate mixing ratio fields, number concentration, and size. Significant aggregate mass and number concentrations are associated with the 6.2 km level; at this level aggregate sizes are respectively small. The largest aggregates are associated with the lower cloud level. The contours of total ice mass (Figure 7.13) shows maxima in total cloud ice around the 8km level with cloud top exisiting up to about 9.5 km and bases lowering to below the 5 km level. Lidar and radar measurements of cloud ice content (Figure 6.11) show significant mass in these regions; however larger masses exist in this data near cloud base than was predicted by the model. Model ice showed maxima up to 0.28×10^{-1} g/kg (about 0.02 gm^{-3}) at mid to upper cloud levels and mixing ratios near cloud base of 0.4×10^{-2} g/kg (about 0.004 gm^{-3}).

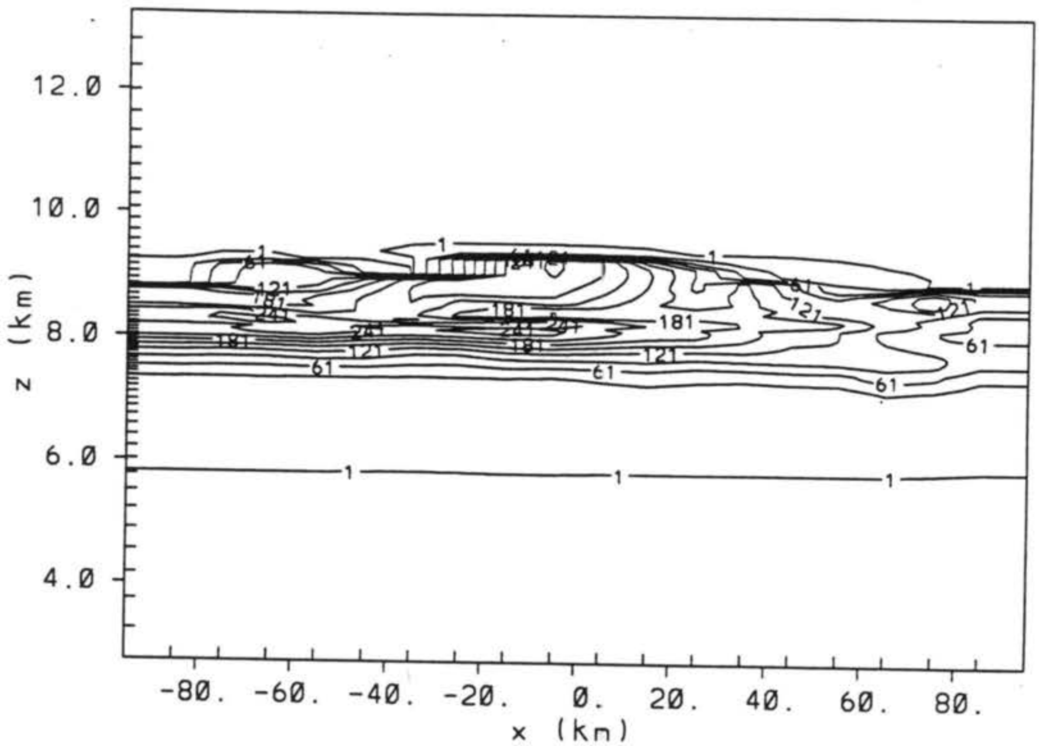

Figure 7.4: RN1 Pristine Ice Mixing Ratio. Max contour, 0.27E-4 kg/kg; Min contour, 0.1E-6 kg/kg; Contour interval, 0.3E-5 kg/kg.

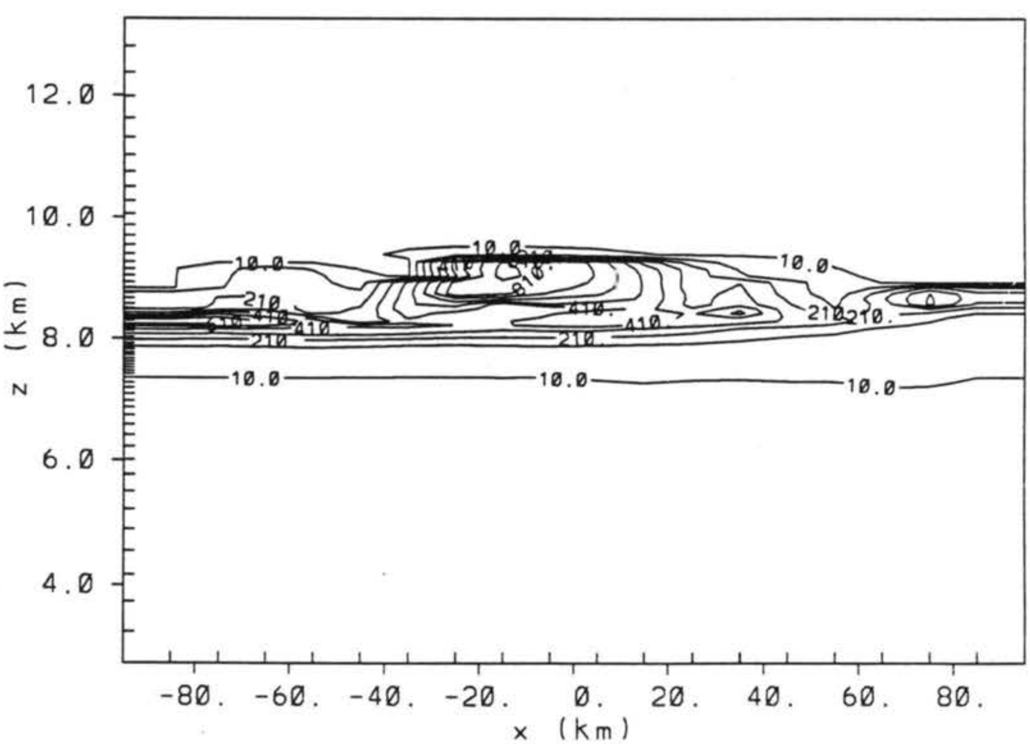

Figure 7.5: RN1 Pristine Ice Concentration. Max contour, 960 l^{-1} ; Min contour, 10 l^{-1}; Contour interval, 100 l^{-1}.

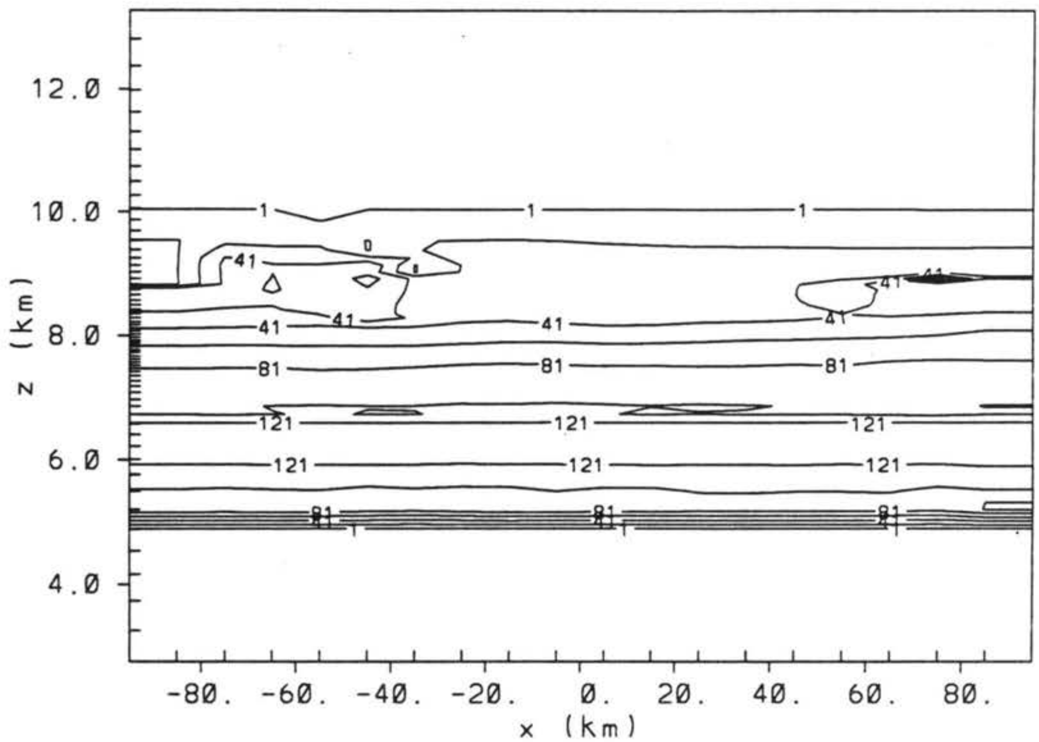

Figure 7.6: RN1 Pristine Ice Size. Max contour, 121 μm; Min contour, 1 μm; Contour interval, 20 μm.

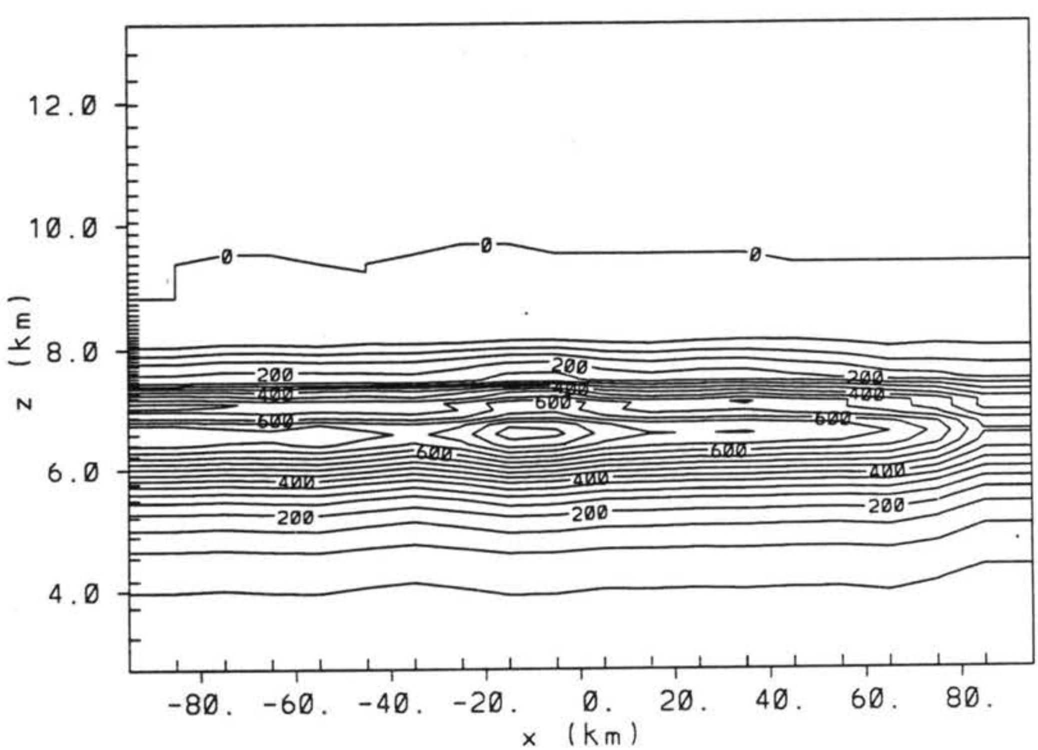

Figure 7.7: RN1 Snow Mixing Ratio. Max contour, 0.8E-5 kg/kg; Min contour, 0.0 kg/kg; Contour interval, 0.5E-6 kg/kg.

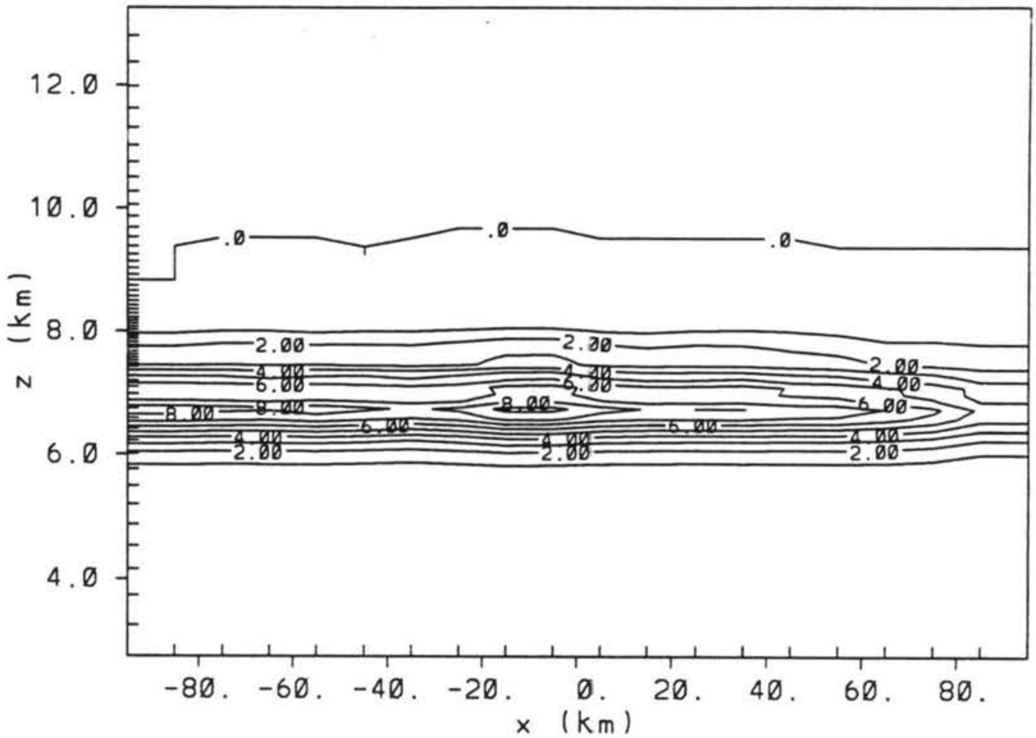

Figure 7.8: RN1 Snow Concentration. Max contour, 9 l^{-1} ; Min contour, 0.0 l^{-1}; Contour interval, 1 l^{-1}.

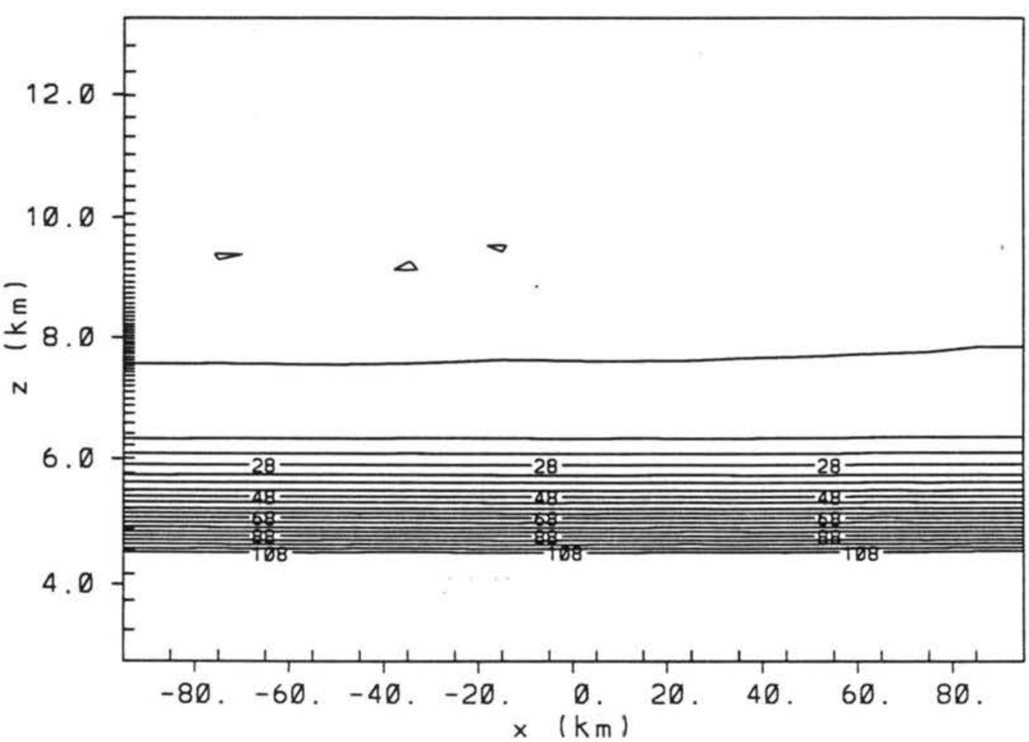

Figure 7.9: RN1 Snow Size. Max contour, 1080 μm; Min contour, 130 μm; Contour interval, 50 μm.

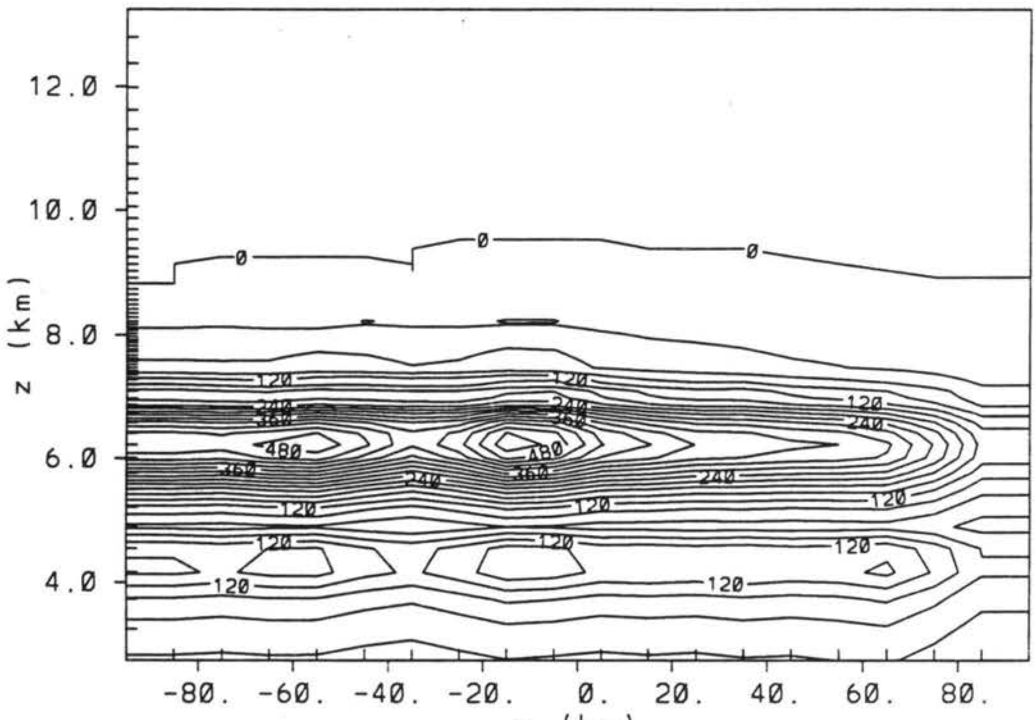

Figure 7.10: RN1 Aggregate Mixing Ratio. Max contour, 0.51E-6 kg/kg; Min contour, 0.0 kg/kg; Contour interval, 0.3E-7 kg/kg.

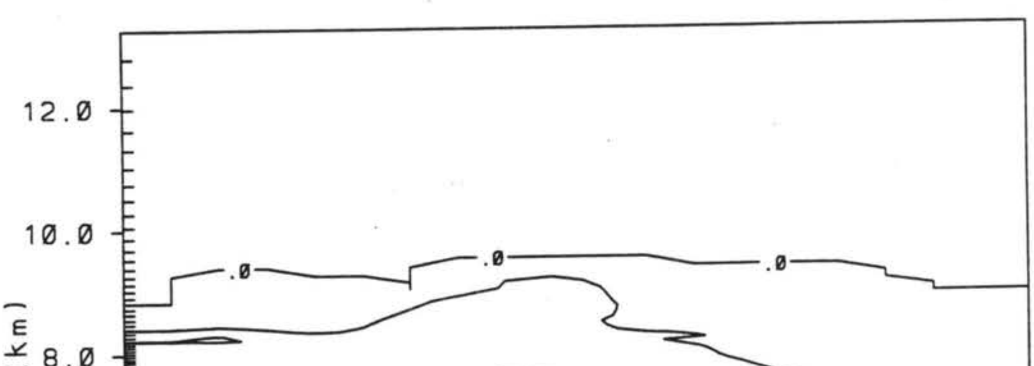

Figure 7.11: RN1 Aggregate Concentration. Max contour, 0.3 l^{-1} ; Min contour, 0.0 l^{-1}; Contour interval, 0.3E-1 l^{-1}.

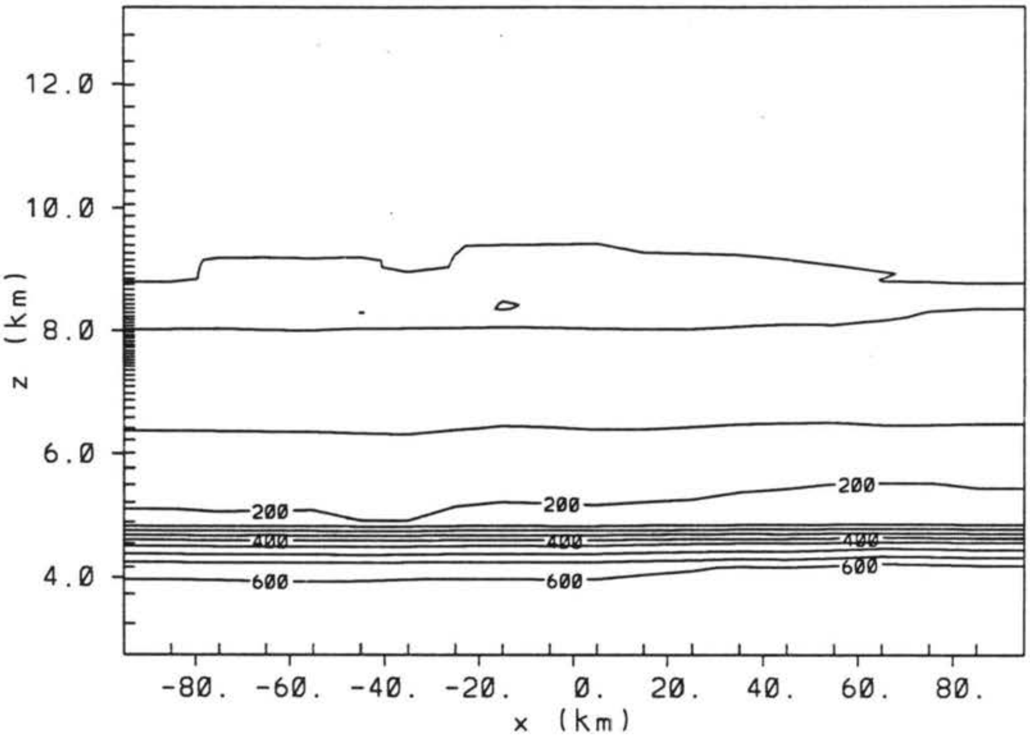

Figure 7.12: RN1 Aggregate Size. Max contour, 600 μm; Min contour, 50 μm; Contour interval, 50 μm.

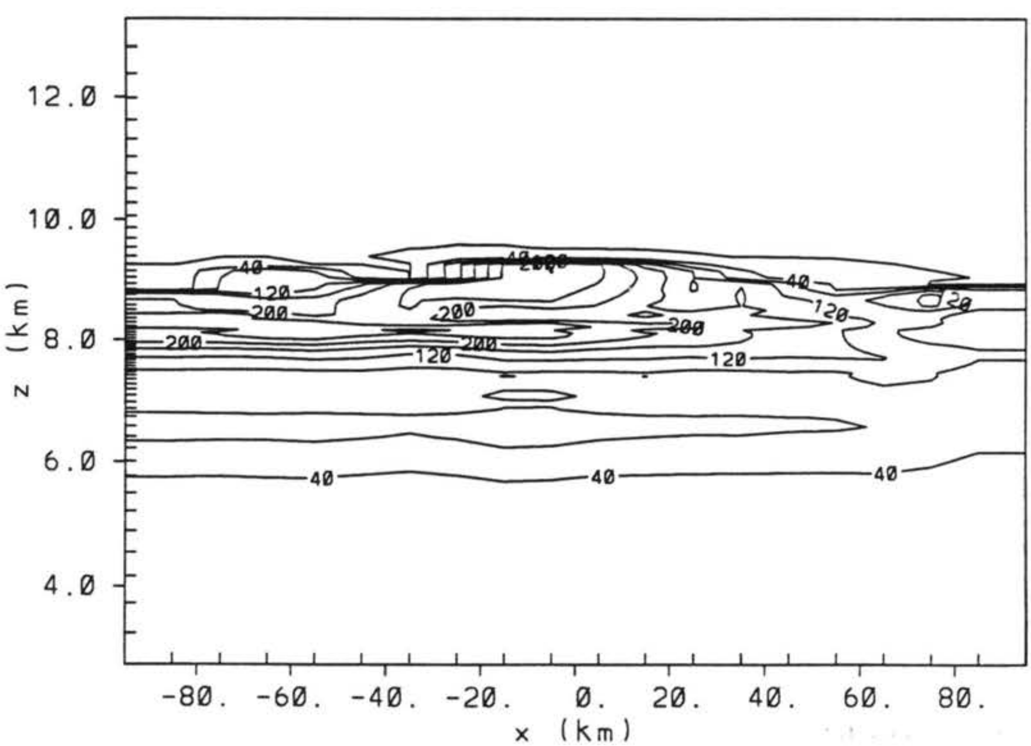

Figure 7.13: RN1 Total Mixing Ratio. Max contour, 0.28E-4 kg/kg; Min contour, 0.5E-7 kg/kg; Contour interval, 0.4E-5 kg/kg.

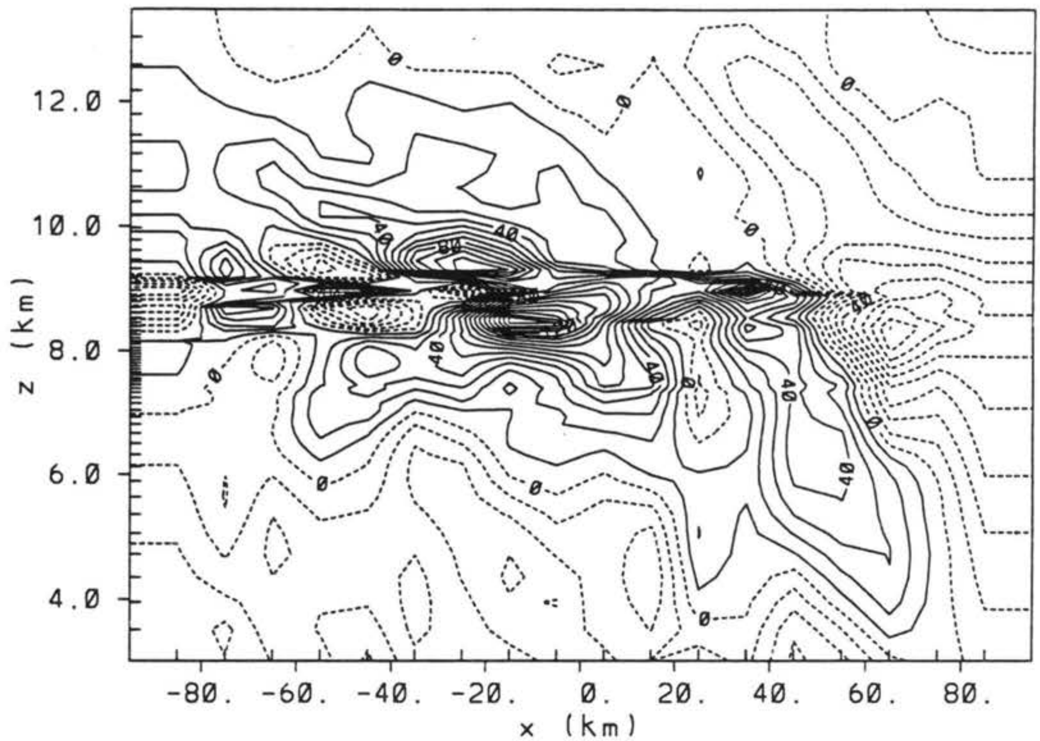

Figure 7.14: RN1 w field. Max contour, 0.16E-1 m/s; Smallest contour, -0.9E-2 m/s; Contour interval, 0.1E-2 m/s.

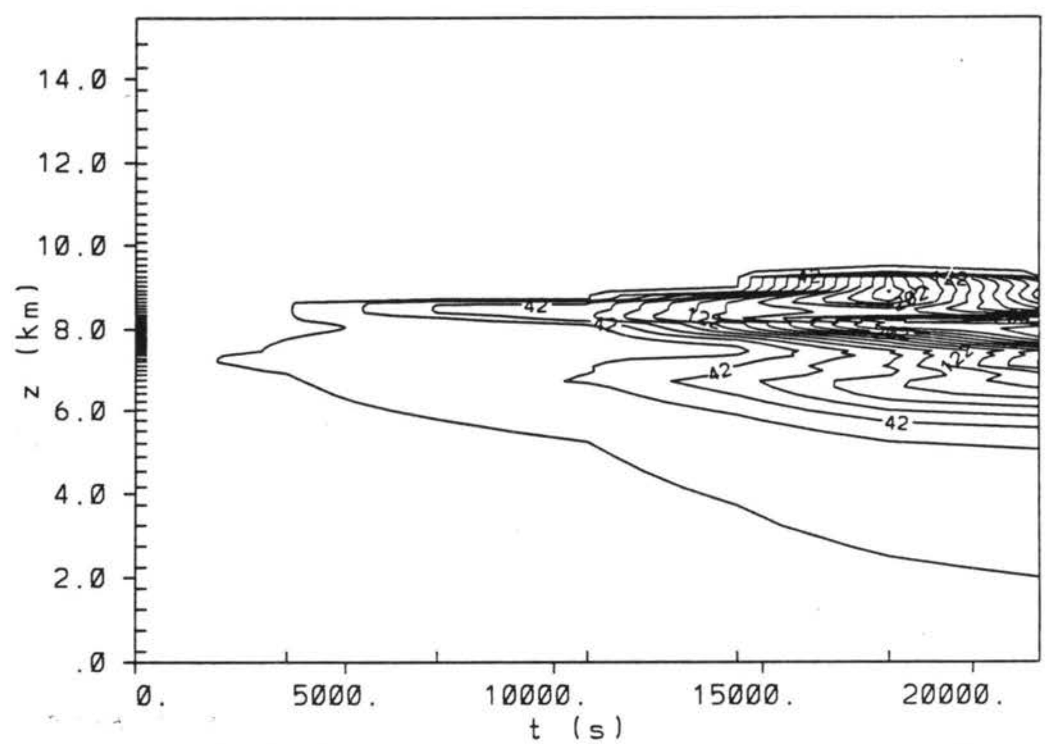

Figure 7.15: RN1 Total Mixing Ratio Time-Series. Max contour, 0.28E-4 kg/kg; Min contour, 0.25E-6 kg/kg; Contour interval, 0.2E-5 kg/kg.

The model predicited updraft and downdraft profiles (Figure 7.14) shows maximums in cloud of 0.16×10^{-1} m/s (-0.9×10^{-2} m/s). The observations presented in Figure 6.7 by Mace et al. (1993) shows values of w up to about 18 cm/s while model maxima were up to 2-3 cm/s.

The model results were lower than observations because cloud-top radiative cooling is the major source of convective motions. There is no mechanical forcing of updrafts by convergence of u wind component which would produce larger updraft velocities. The cloud boundaries as shown in a time-series plot of the cloud total ice content (Figure 7.15) compares well with the boundaries observed with radar (Figure 6.12). The model result shows cloud base lower than was observed, however the smallest contoured value of the mixing ratio in Figure 7.15 is 0.25×10^{-3} g/kg which is smaller than that observed by radar. Overall, the model seems to have done significantly well in describing the cirrus event.

7.2 Sensitivity Tests of the Model Parameterizations

In order to examine the multitude of sensitivity tests illustrated in Table 7.1 without the use of hundreds of figures, we will examine the relevant plots for each case and utilize tables in order to streamline the discussion process. Tables 7.2 and 7.3 contain maximum values for the various fields at 2 hours and 5 hours respectively. These tables will be referred to as necessary. In the following subsections we will discuss the sensitivity test results in comparison to the control run.

7.2.1 Needle Crystals, Snow and Aggregate Distribution Shape, $\nu = 1$

The use of needle crystals in the cirrus simulation differs quite substantially after 5 model hours from those done for the control run above. Even after 2 hours of simulation (Table 7.2) large differences in the mixing ratios of all fields is observed. Figure 7.16 and 7.17 show less structure to the pristine ice fields after 5 hours than that of the control run (Figures 7.2 and 7.3). Pristine ice concentrations are smaller for the needle simulation and ice masses are less. Note also that the pristine ice fields for needles is of much less vertical extent than for the control. The less vertical structure of these fields has to do with the stronger vertical motion exhibited by the control simulation (see Table 7.3) and the larger terminal velocities associated with the rosette crystals. As Mitchell et al. (1994) observed in his modeling of cirrus clouds, the more spatial habits tend to have larger number concentrations; this has to do with the growth of the given habit.

Table 7.2: Simulations: 2 Hour Values

Test	r_a (kg/kg)	N_a (l^{-1})	r_p (kg/kg)	N_p (l^{-1})	r_s (kg/kg)
Control	0.16×10^{-8}	0.27×10^{-2}	0.54×10^{-4}	270	0.57×10^{-6}
NN1	0.112×10^{-9}	0.68×10^{-3}	0.26×10^{-5}	540	0.72×10^{-7}
PN1	0.64×10^{-10}	0.10×10^{-2}	0.17×10^{-5}	440	0.10×10^{-8}
NN3	0.90×10^{-9}	0.11×10^{-2}	0.32×10^{-5}	460	0.64×10^{-7}
RN3	0.16×10^{-7}	0.20×10^{-2}	0.46×10^{-5}	260	0.51×10^{-6}
RSM	0.96×10^{-7}	—	0.40×10^{-5}	280	0.17×10^{-6}
RNR	0.16×10^{-6}	0.80×10^{-2}	0.85×10^{-6}	38	0.38×10^{-6}
RNH	0.17×10^{-6}	0.85×10^{-2}	0.85×10^{-6}	6.3	0.40×10^{-6}
N5RH	0.11×10^{-5}	.30	0.48×10^{-4}	9500	0.31×10^{-6}
RCIN	0.14×10^{-4}	2.5	0.12×10^{-4}	144	0.26×10^{-5}

Table 7.2: Simulations: 2 Hour Values, cont.

Test	N_s (l^{-1})	r_{tot} (kg/kg)	D_p (μm)	D_s (μm)	D_a (μm)	w (m/s)
Control	0.68	0.54×10^{-5}	121	1700	850	0.54×10^{-2}
NN1	0.19	0.26×10^{-5}	121	1600	950	0.54×10^{-2}
PN1	0.0012	0.17×10^{-5}	121	1700	160	0.54×10^{-2}
NN3	0.038	0.32×10^{-5}	121	190	1900	0.54×10^{-2}
RN3	0.112	0.48×10^{-5}	121	290	380	0.54×10^{-2}
RSM	—	0.44×10^{-5}	121	—	—	0.53×10^{-2}
RNR	0.57	0.11×10^{-5}	121	1020	760	0.72×10^{-2}
RNH	0.60	0.12×10^{-5}	121	1010	780	0.54×10^{-2}
N5RH	0.96	0.48×10^{-4}	121	340	900	0.30×10^{-1}
RCIN	3.8	0.20×10^{-4}	121	250	270	0.49×10^{-2}

Table 7.2: Model values for all tests after 2 hours of simulation. The table headings are defined as: r_a = aggregate mixing ratio, N_a = aggregate number concentration, r_p = pristine ice mixing ratio, N_p = prisine ice number concentration, r_s = snow mixing ratio, N_s = snow number concentration, r_{tot} = total ice mixing ratio, $\bar{D}_p$ = pristine ice size, $\bar{D}_s$ = snow size, $\bar{D}_a$ = aggregate size, and w = updraft velocity.

Table 7.3: Simulations: 5 Hour Values					
Test	r_a (kg/kg)	N_a (m^{-3})	r_p (kg/kg)	N_p (m^{-3})	r_s (kg/kg)
Control	0.51×10^{-7}	0.31	0.27×10^{-4}	960	0.80×10^{-5}
NN1	0.85×10^{-7}	0.57×10^{-1}	0.11×10^{-4}	200	0.16×10^{-5}
PN1	0.10×10^{-8}	0.15×10^{-2}	0.32×10^{-5}	310	0.40×10^{-7}
NN3	0.64×10^{-6}	0.76×10^{-1}	0.76×10^{-5}	136	0.13×10^{-5}
RN3	0.18×10^{-5}	.22	0.90×10^{-5}	54	0.42×10^{-5}
RSM	0.11×10^{-5}	—	0.85×10^{-5}	60	0.48×10^{-6}
RNR	0.36×10^{-6}	0.11×10^{-1}	0.12×10^{-5}	4.8	0.46×10^{-6}
RNH	0.11×10^{-6}	0.32×10^{-2}	0.12×10^{-5}	3.8	0.16×10^{-6}
N5RH	0.96×10^{-5}	4.0	0.60×10^{-4}	7200	0.85×10^{-6}
RCIN	0.68×10^{-5}	0.72	0.90×10^{-5}	96	0.14×10^{-5}

Table 7.3: Simulations: 5 Hour Values, cont.						
Test	N_s (m^{-3})	r_{tot} (kg/kg)	$\bar{D}_p$ (μm)	$\bar{D}_s$ (μm)	$\bar{D}_a$ (μm)	w
Control	9.0	0.28×10^{-4}	121	2300	960	0.16×10^{-1}
NN1	3.6	0.11×10^{-4}	121	2000	1120	0.64×10^{-2}
PN1	0.051	0.32×10^{-5}	121	2400	640	0.64×10^{-2}
NN3	0.76	0.80×10^{-5}	121	210	310	0.64×10^{-2}
RN3	0.96	0.10×10^{-4}	121	290	1180	0.90×10^{-2}
RSM	—	0.90×10^{-5}	121	—	—	0.56×10^{-2}
RNR	0.64	0.17×10^{-5}	121	1020	1080	0.52×10^{-2}
RNH	0.14	0.14×10^{-5}	121	1360	800	0.51×10^{-2}
N5RH	2.6	0.63×10^{-4}	121	153	680	0.32×10^{-1}
RCIN	2.1	0.11×10^{-4}	121	300	380	0.56×10^{-2}

Table 7.3: Model values of various quantites after 5 hours of model simulations. Symbols are as stated above in Table 7.2.

A more spatial habit has a larger value of the mass-dimensional exponent, β; this means that for a given mass increase a habit with a smaller value of β will increase in size more than that of a habit with a larger β exponent (shown in Figure 5.23). One can think of this simply as having to distribute the given mass over a larger surface area in the case of the habit with larger β values; this causes the smaller β valued crystals to transfer number concentrations faster with less associated mass.

Of course, there are many other factors acting than just vapor deposition, such as aggregation, however this general trend seems to hold. Examination of the diameters of pristine ice in the region of the largest mass and number concentration (about 8.2 km in Figure 7.18) shows that the needle

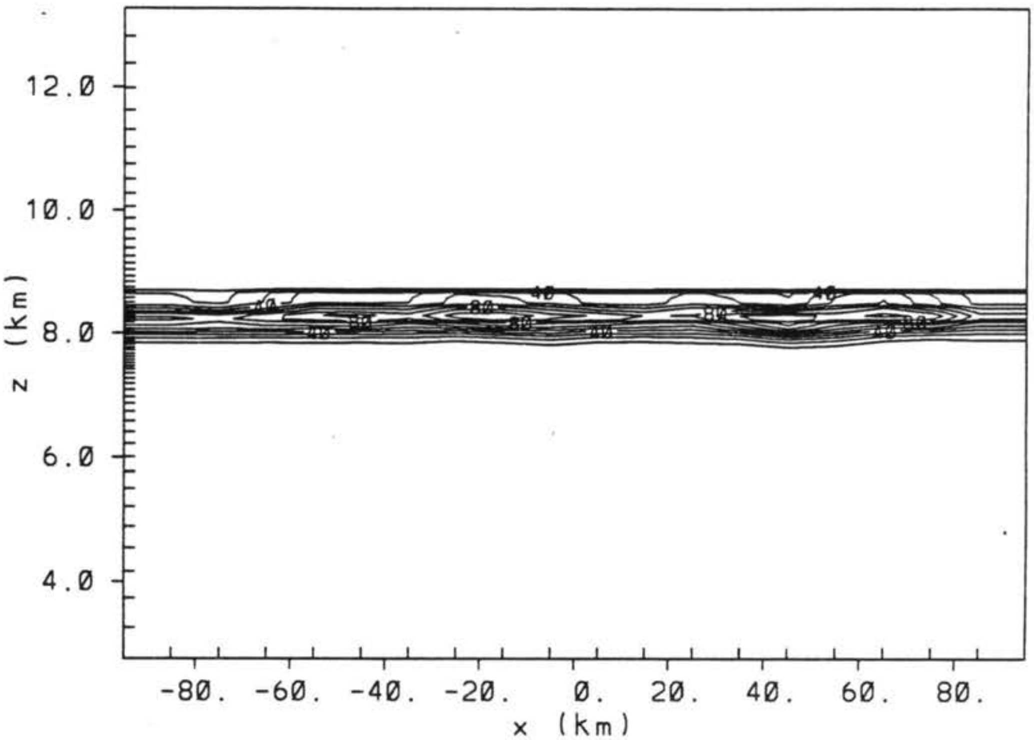

Figure 7.16: NN1 Pristine Ice Mixing Ratio. Max contour, 0.12E-4 kg/kg; Min contour, 0.1E-5 kg/kg; Contour interval, 0.1E-5 kg/kg.

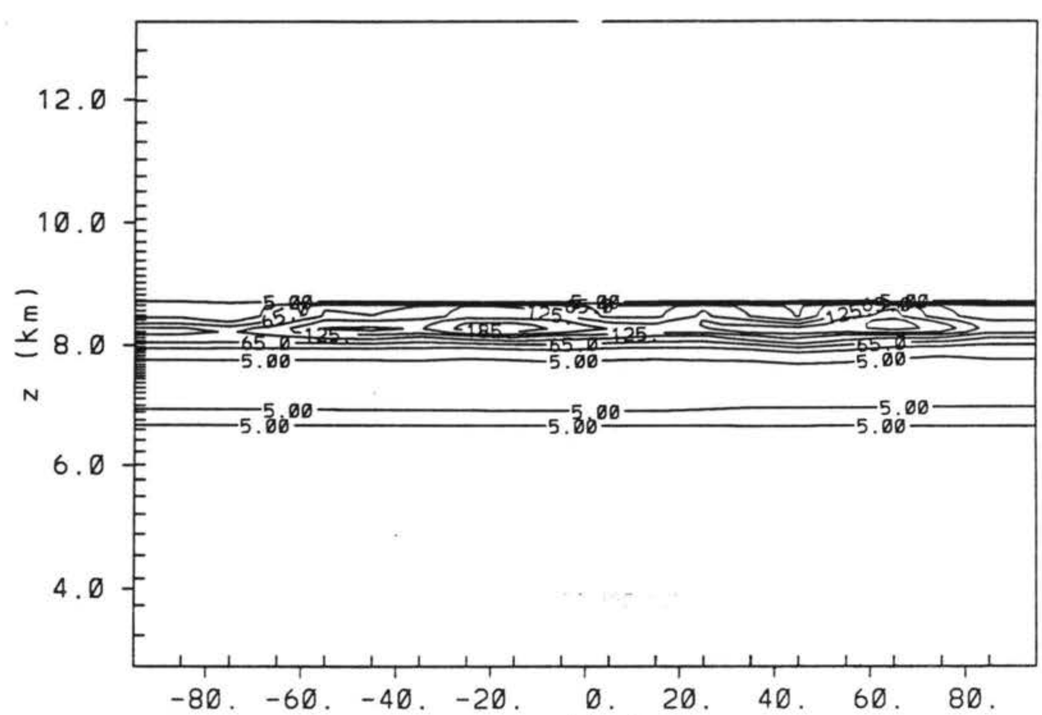

Figure 7.17: NN1 Pristine Ice Concentration. Max contour, 185 l^{-1} ; Min contour, 5 l^{-1}; Contour interval, 30 l^{-1}.

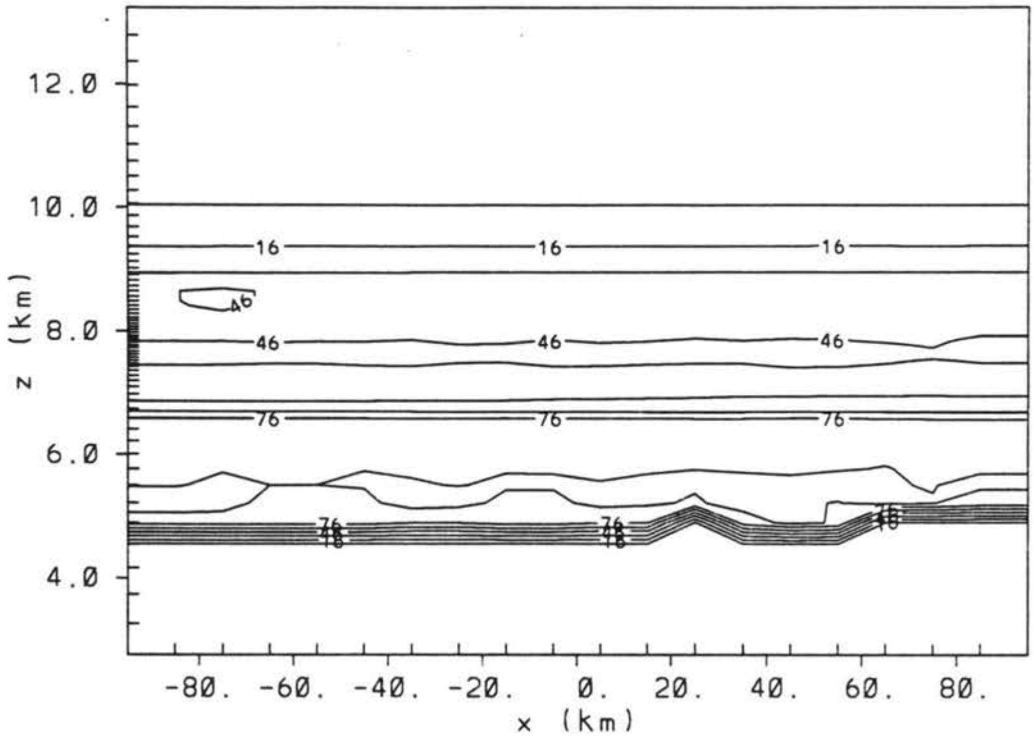

Figure 7.18: NN1 Pristine Ice Size. Max contour, 121 μm; Min contour, 1 μm; Contour interval, 15 μm.

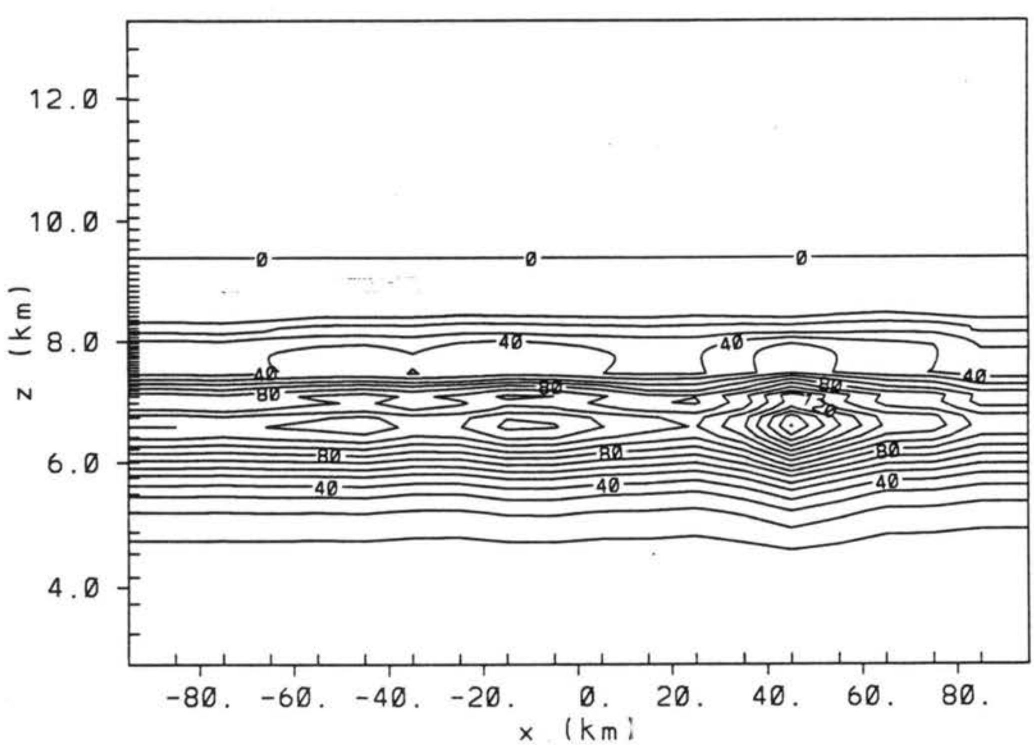

Figure 7.19: NN1 Snow Mixing Ratio. Max contour, 0.16E-5 kg/kg; Min contour, 0.0 kg/kg; Contour interval, 0.1E-6 kg/kg.

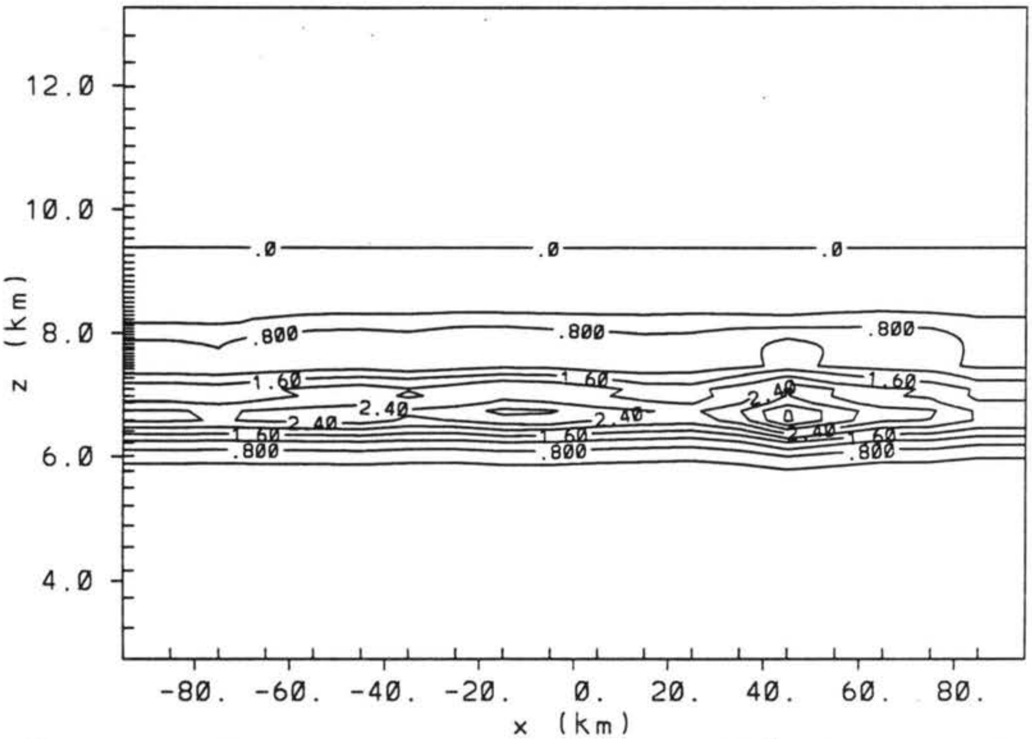

Figure 7.20: NN1 Snow Concentration. Max contour, 3.6 l^{-1} ; Min contour, 0.0 l^{-1}; Contour interval, 0.4 l^{-1}.

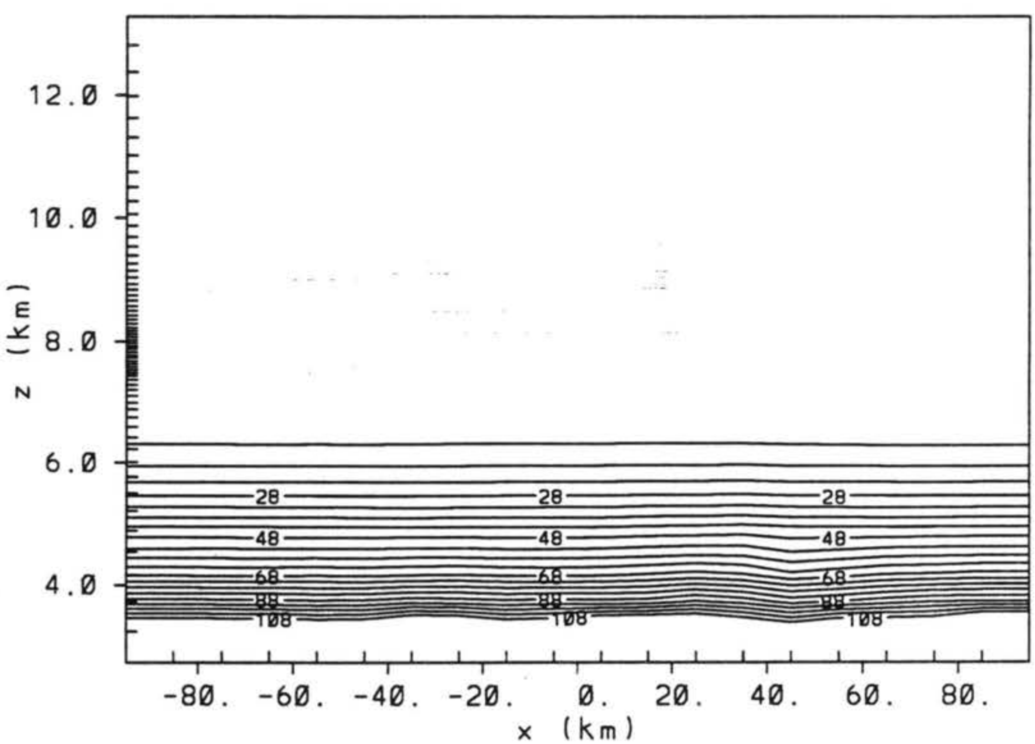

Figure 7.21: NN1 Snow Size. Max contour, 1080 μm; Min contour, 130 μm; Contour interval, 50 μm.

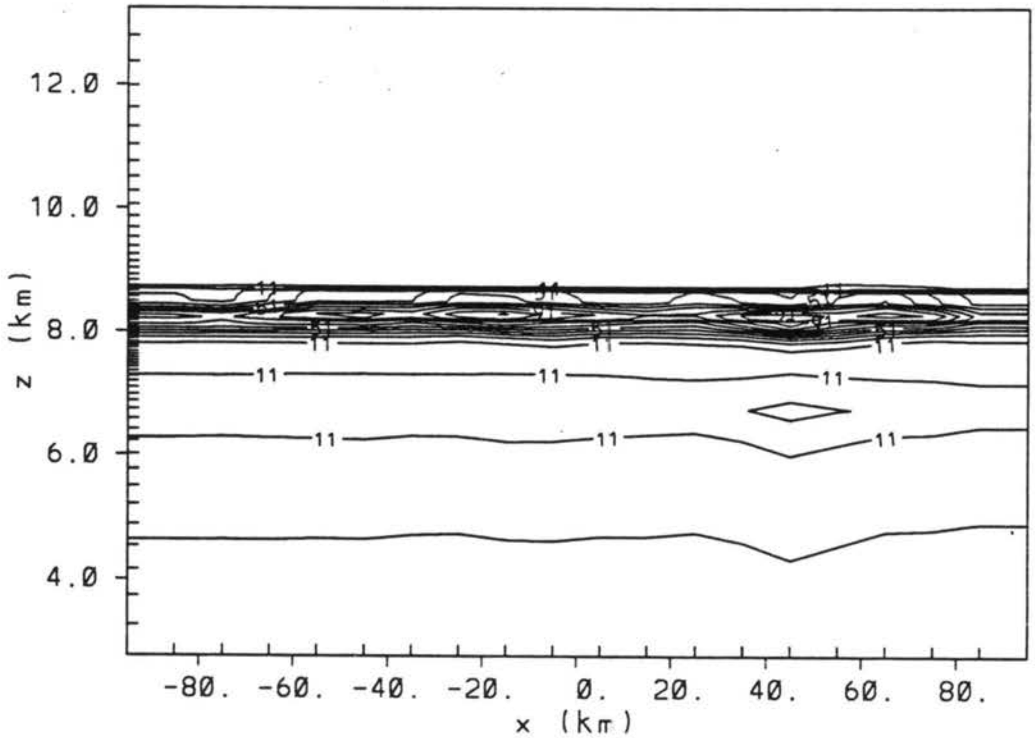

Figure 7.22: NN1 Total Ice Mixing Ratio. Max contour, 0.11E-4 kg/kg; Min contour, 0.1E-6 kg/kg; Contour interval, 0.1E-5 kg/kg.

simulations contain larger size crystals than do the rosettes. This tendency would also, assumedly, produce smaller overall masses for the distributions. This can be seen in Table 7.3 where the overall masses for all of the fields are less for NN1 than for the control simulation. The model produced snow fields (Figures 7.19 and 7.20) show lower mass and number concentrations than are produced for the control simulation, (Figures 7.5 and 7.6), however the sizes of the snow crystals are larger in the rosette case (compare Figures 7.21 and 7.7). The total ice fields (Figure 7.22) as compared to the fields produced by the model for the control simulation (Figure 7.13) shows that the needle crystal cloud has about 1/2 the mass of the rosette cloud. The rosette cloud contains more mass at lower level due to the enhanced growth due to the stronger updraft velocities, fallout from upper cloud levels due to their larger terminal velocites and their larger masses associated with their mass-dimensional relationship. The total ice field also shows that the control simulation has much more of an overal structure to it than the NN1 simulation.

This is in part due to the more complex updraft structure of the control simulation, which no doubt is effected by the differing growth kinetics of the rosette crystals. These crystals would most likely release more heat during vapor depositional growth which affect the cloud updraft and downdraft structure.

7.2.2 Plate Crystals with Snow Distribution Shape $\nu = 1$

The plate crystal simulation (PN1), shows much less structure in its pristine ice fields than the control and the NN1 simulation. After 2 hours of model simulation (Table 7.2) this simulation produces less overall mass but higher number concentrations than the control simulation. Figures 7.23 and 7.24 show the pristine ice modeled mixing ratio and number concentration contour plots after 5 horus of simulation. Mixing ratios and number concentrations are much smaller for the plate simulation than for the rosette simulation. Since plate crystals have mass-dimension exponent that is larger than for rosettes (2.5 as compared with 2.26) one would expect that their might be larger number cocnentrations associated with this simulation than with the control. It appears, however, that the updraft profiles produced by the model in the control case played a large role in the maintenance of ice in cloud. Interaction with microphysics is also important; for rosette crystals, as was stated above, growth kinetics can play a greater role in the heat budget. The sizes of the pristine ice crystals are much smaller in cloud for the plate simulation than for the control, evidence that a much narrower distribution of ice exists in this case (see Figure 7.25).

The contour plots of the snow fields for plate crystals shown in Figures 7.26 and 7.27 show maximum values of the mixing ratio of two orders of magnitude higher in the control case. This field is very low because the pristine ice distribution for plates contains low mass and is very narrow. Since these crystals tend to grow slowly in comparison to needles or rosettes, there will not be a very large transfer of pristine ice to snow. The plots of snow size (Figure 7.28) shows crystals on the order of 1 mm down to 2 km. In the control simulation, as is shown in Table 7.3, snow in both simulations reach about the same maximum size, however, the control simulation has larger mass and number concentraitons associated with these snow sizes.

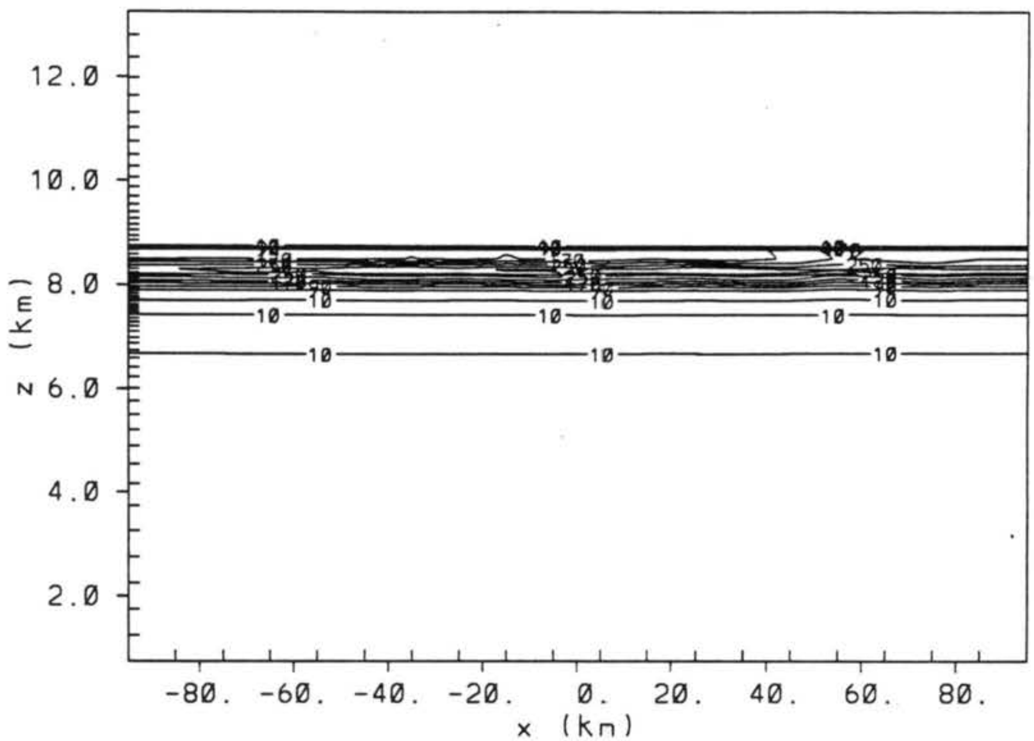

Figure 7.23: PN1 Pristine Ice Mixing Ratio. Max contour, 0.37E-5 kg/kg; Min contour, 0.1E-6 kg/kg; Contour interval, 0.4E-6 kg/kg.

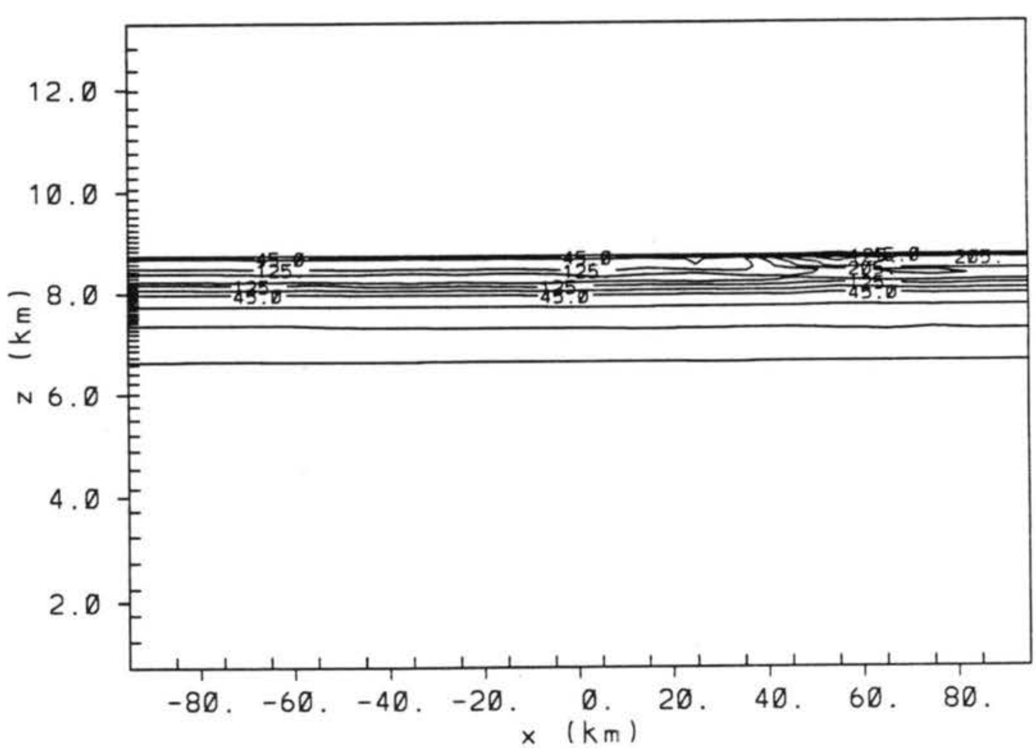

Figure 7.24: PN1 Pristine Ice Concentration. Max contour, 325 l^{-1} ; Min contour, 5 l^{-1}; Contour interval, 40 l^{-1}.

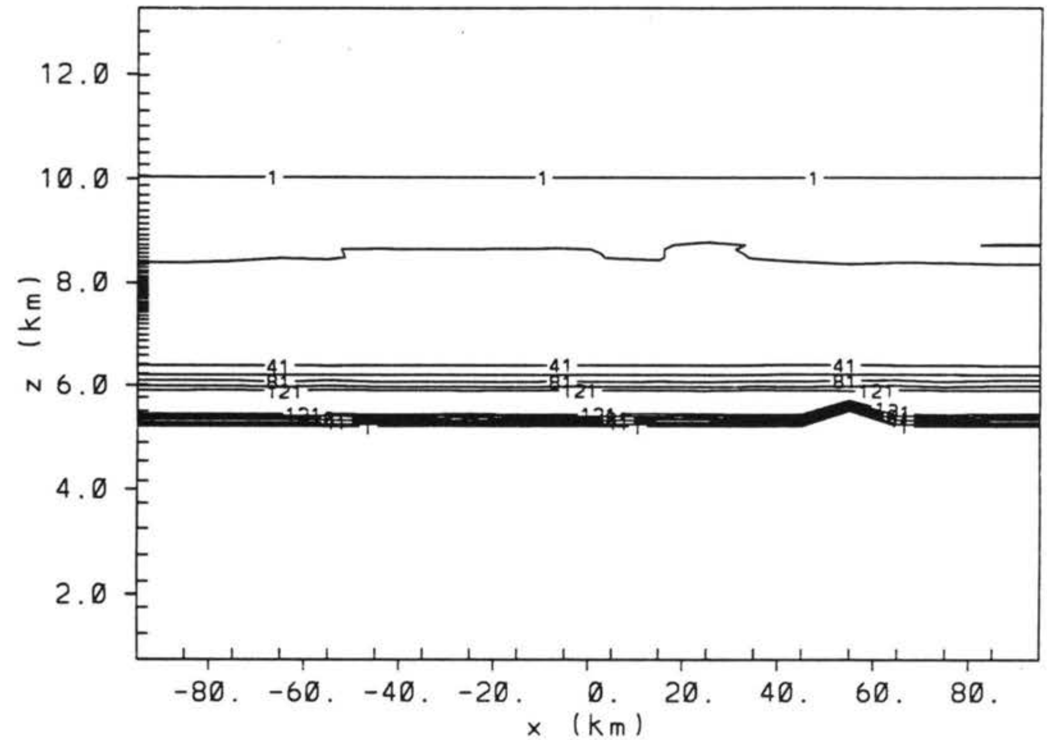

Figure 7.25: PN1 Pristine Ice Size. Max contour, 121 μm; Min contour, 1 μm; Contour interval, 20 μm.

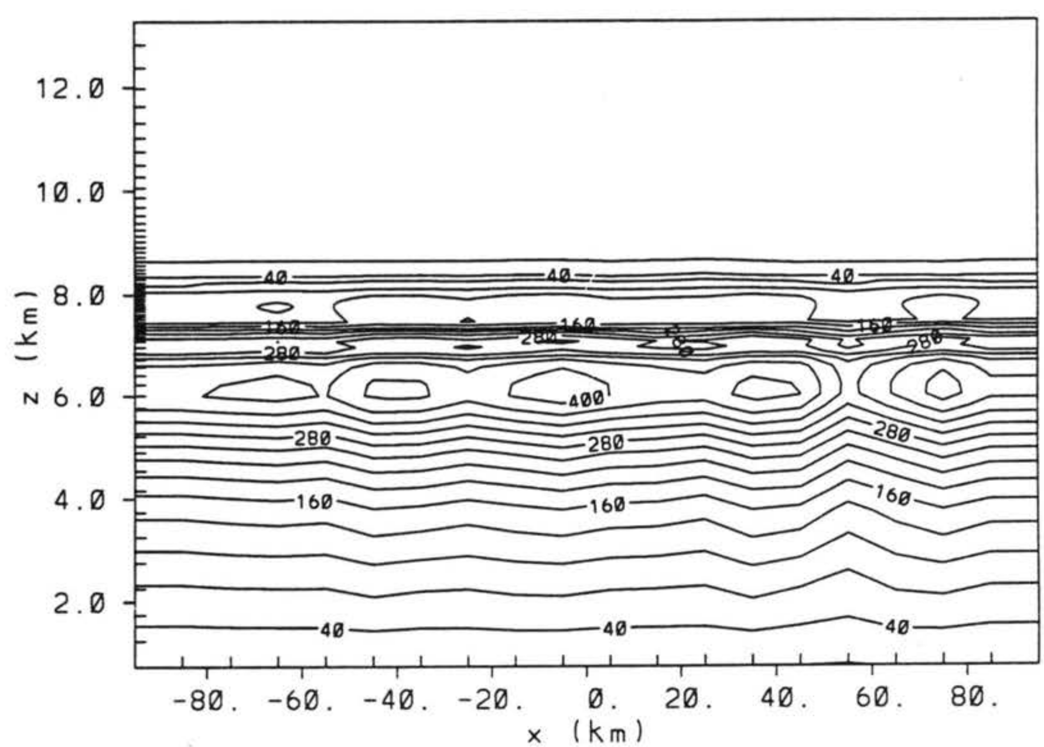

Figure 7.26: PN1 Snow Mixing Ratio. Max contour, 0.49E-7 kg/kg; Min contour, 0.1E-8 kg/kg; Contour interval, 0.3E-8 kg/kg.

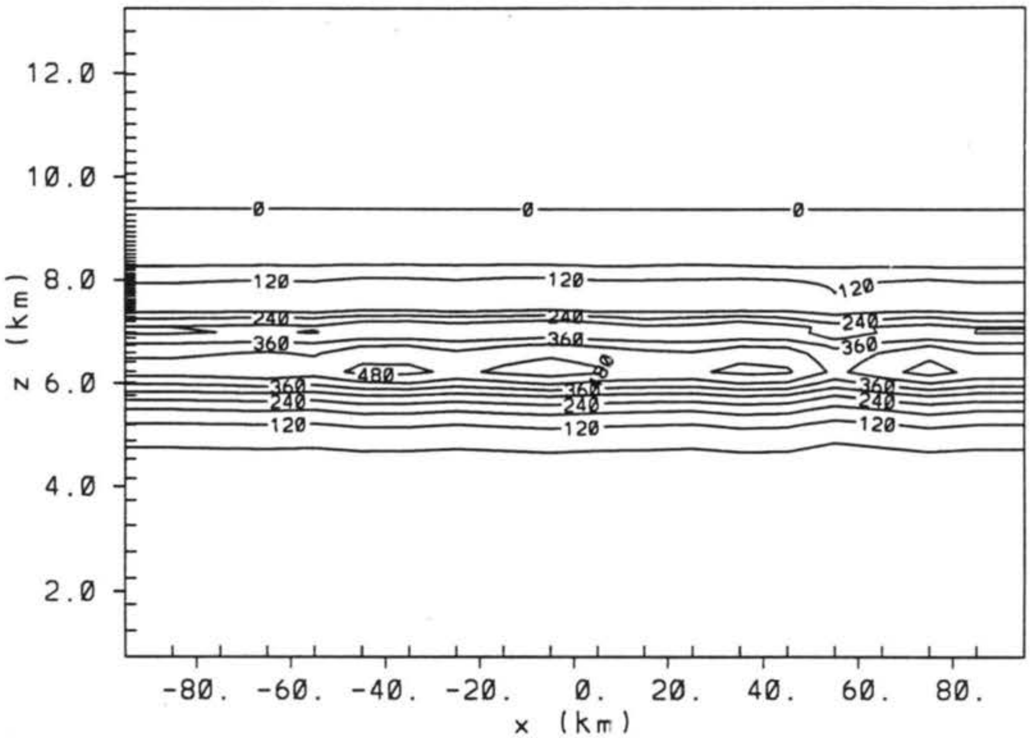

Figure 7.27: PN1 Snow Concentration. Max contour, 0.48E-1 l^{-1} ; Min contour, 0.0 l^{-1}; Contour interval, 0.6E-2 l^{-1}.

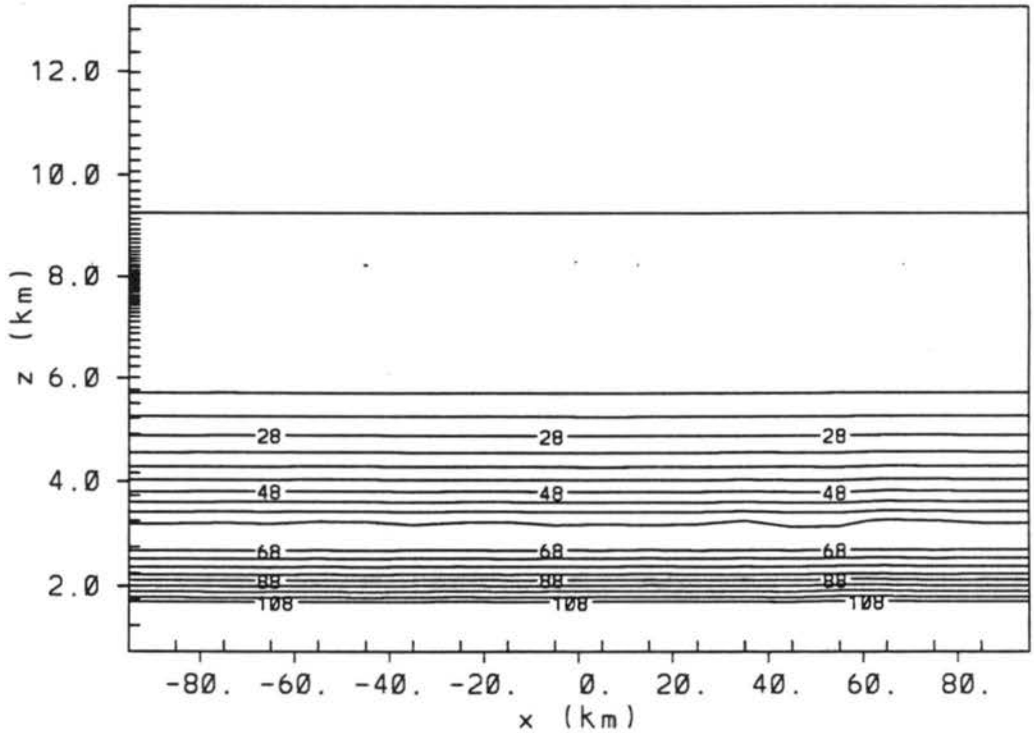

Figure 7.28: PN1 Snow Size. Max contour, 1080 μm; Min contour, 130 μm; Contour interval, 50 μm.

Overall, it can be seen from these simulations that choice of crystalline habit makes a large difference in the final results.

7.2.3 Needle crystals with Snow Distribution Shape $\nu = 3$

The simulations in which the shape of the snow distribution is varied shows how important this parameter is in cirrus simulations. Figure 6.9 (from Arnott et al., 1993) shows that larger cirrus ice crystals can be distributed in what appears to be a $\nu = 3$ distribution shape. In this and the next subsection we examine the effects of distribution shape on the cirrus cloud simulations.

The total ice mixing ratio produced for this case, NN3 (Figure 7.29), shows smaller values than for the NN1 case simulation; Figure 7.22. Cloud structure and height is about the same as for the NN1 case, however. Also, the number concentrations are lower for pristine ice and snow in this case than the NN1 case. This has to do with the $\nu = 3$ distribution shape assumed for snow and aggregates which affects, vapor depositional growth, collection, and transfer rates from pristine ice to snow. The difference is due to the higher weight given to larger crystals in the $\nu = 3$ distribution; thus vapor deposition, collection, and transfers from pristine ice to snow should be about 3 times larger. This is shown in Table 7.3, note that the mass of aggregates for this case is much larger than for the NN1 case. Aggregate mass is enhanced over the control due to the higher weighted collection functions in this case. Figure 7.32 shows the effect on pristine ice mean diameter. Since mass is a higher weighted moment, the largest crystals will contribute the most to this process. Also, the higher weighted snow and aggregate distributions will increase competiton for the available vapor, thus there will not be as much around for the vapor depositional transfer process or nucleation. Therefore, pristine ice mean diameters decrease. This will decrease the transfer of pristine ice to snow since the pristine ice in the vicinty of 125 μm are weigheted much less. The larger value of ν for the snow and aggregate cases increases their masses due to collection. These effects can be noted in Table 7.3 by examining the differences between the simulations NN1 and NN3.

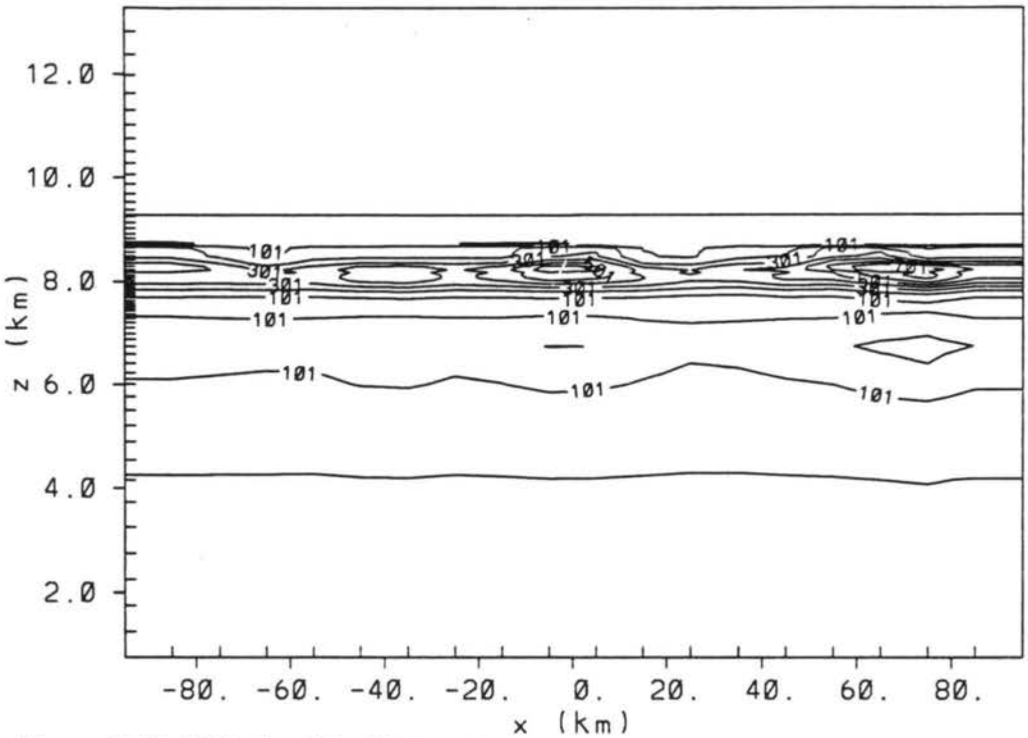

Figure 7.29: NN3 Total Ice Mixing Ratio. Max contour, 0.7E-5 kg/kg; Min contour, 0.1E-7 kg/kg; Contour interval, 0.1E-5 kg/kg.

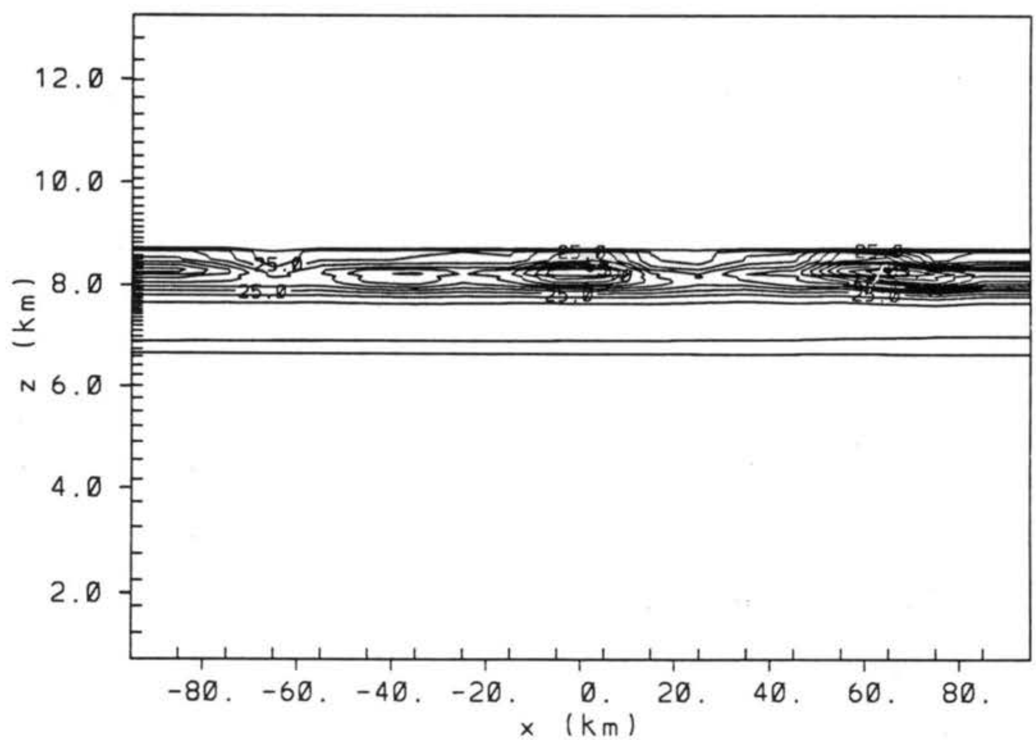

Figure 7.30: NN3 Pristine Ice Concentration. Max contour, 145 l^{-1} ; Min contour, 5 l^{-1}; Contour interval, 10 l^{-1}.

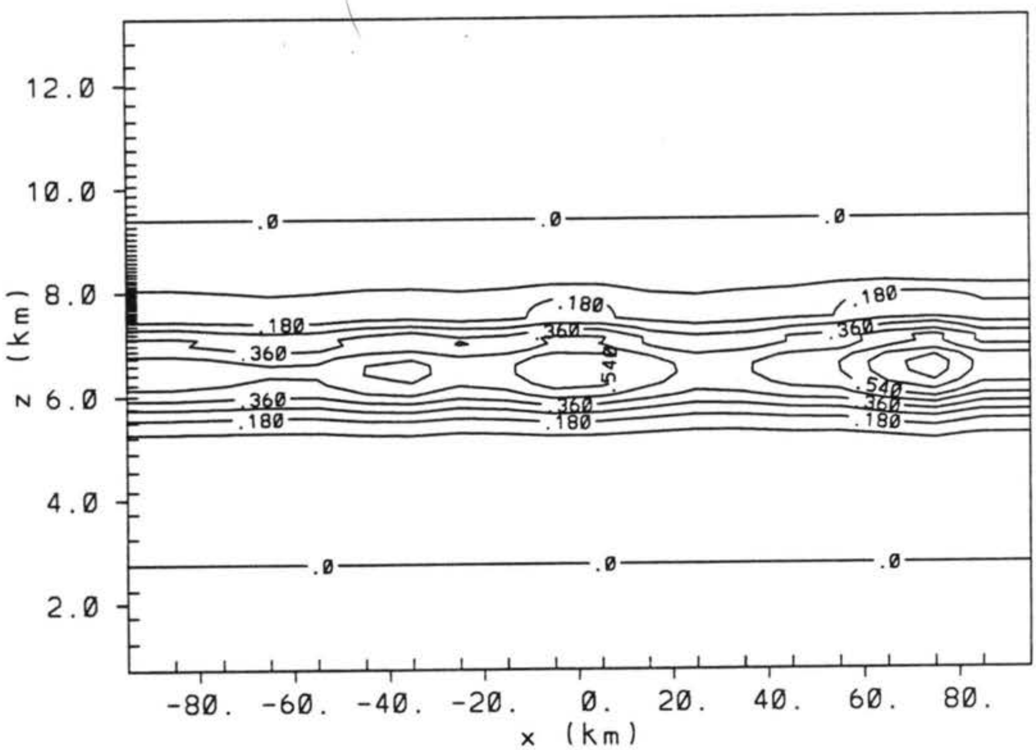

Figure 7.31: NN3 Snow Concentration. Max contour, 7.2 l^{-1} ; Min contour, 0.0 l^{-1}; Contour interval, .9E-1 l^{-1}.

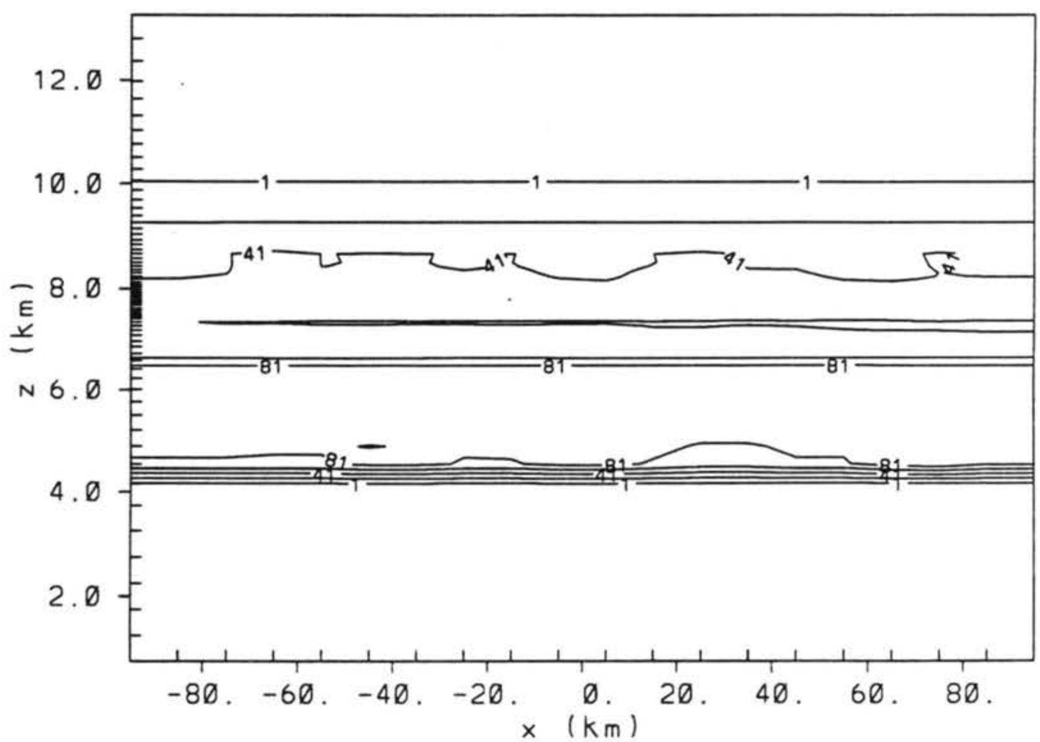

Figure 7.32: NN3 Pristine Ice Size. Max contour, 121 μm; Min contour, 1 μm; Contour interval, 20 μm.

For NN1 there is quite a large gap between the masses of pristine ice and snow, with pristine ice having almost and order of magnitude larger mixing ratio value than snow. Also, in the NN1 case, aggregates are much smaller in mass than either snow or pristine ice. For the NN3 simulation, snow and pristine ice have comparable mixing ratios, and the value of the aggregate mixing ratio is much closer to either pristine ice or snow than in the NN1 case.

7.2.4 Rosettes with Snow and Aggregate Distribution Shape $\nu = 3$

This situation of a larger distribution shape parameter was tested with rosette crystals in the RN3 simulation. Comparison of the total ice mixing ratio field for this simulation (figure 7.33) with that of the control simulation (Figure 7.13) shows that about half of the mass of the control simulation was produced in the RN3 simulation. Cloud structure is different in the RN3 simulation with more mass being associated with the lower cloud levels (about 6.5 km); in the control simulation the largest values in mass were associated with the 8.5 km level. Also, pristine ice and snow concentrations, shown in Figures 7.34 and 7.35 respectively, have lower values than in the control simulation. The reasons for this are the same as those presented above for the NN3 simulation; the larger value of ν increases the mass gained by both snow and aggregates with respect to pristine ice due to increases in the collection and vapor depositional processes. Table 7.3 and Figure 7.33 show this well; in Figure 7.33 more mass is associated with the lower cloud regions, indicitive of mass associated with larger crystals. Table 7.3 shows that pristine ice, snow, and aggregates all have similar mixing ratio maxima; in contrast to the control simulation in which pristine ice dominated. The pristine ice sizes (not shown for this case) had a similar profile as compared to Figure 7.6 for the control, except that the maxima at 121 μm occured at a higher level. These simulations show the importance of the chosen distribution shapes in modeling studies. It seems that $\nu = 3$ may be a better choice for larger ice classes such as snow and aggregates since it weights the larger crystals more and, therefore, seems more physically plausible.

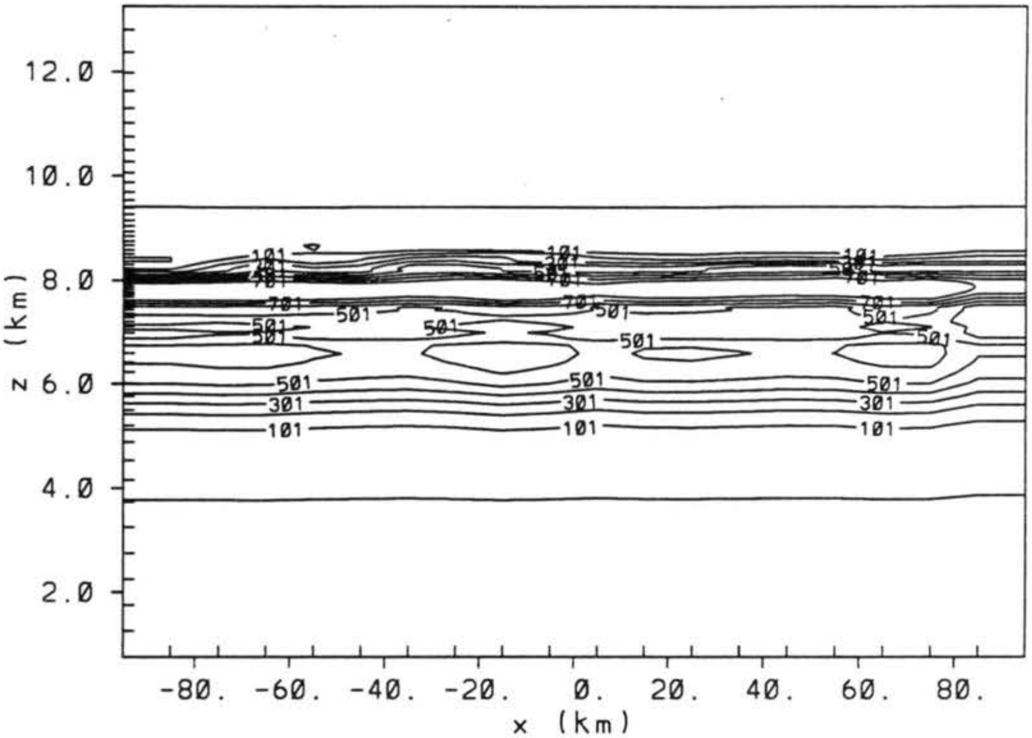

Figure 7.33: RN3 Total Ice Mixing Ratio. Max contour, 0.8E-5 kg/kg; Min contour, 0.1E-7 kg/kg; Contour interval, 0.1E-5 kg/kg.

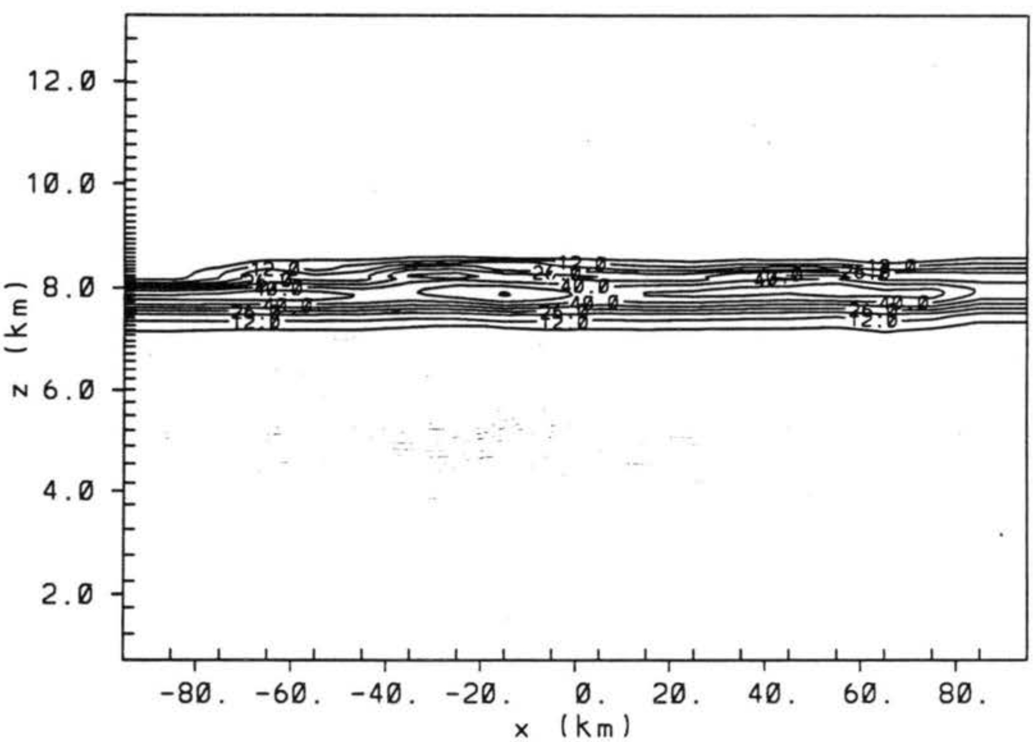

Figure 7.34: RN3 Pristine Ice Concentration. Max contour, 61 l^{-1} ; Min contour, 5 l^{-1}; Contour interval, 7 l^{-1}.

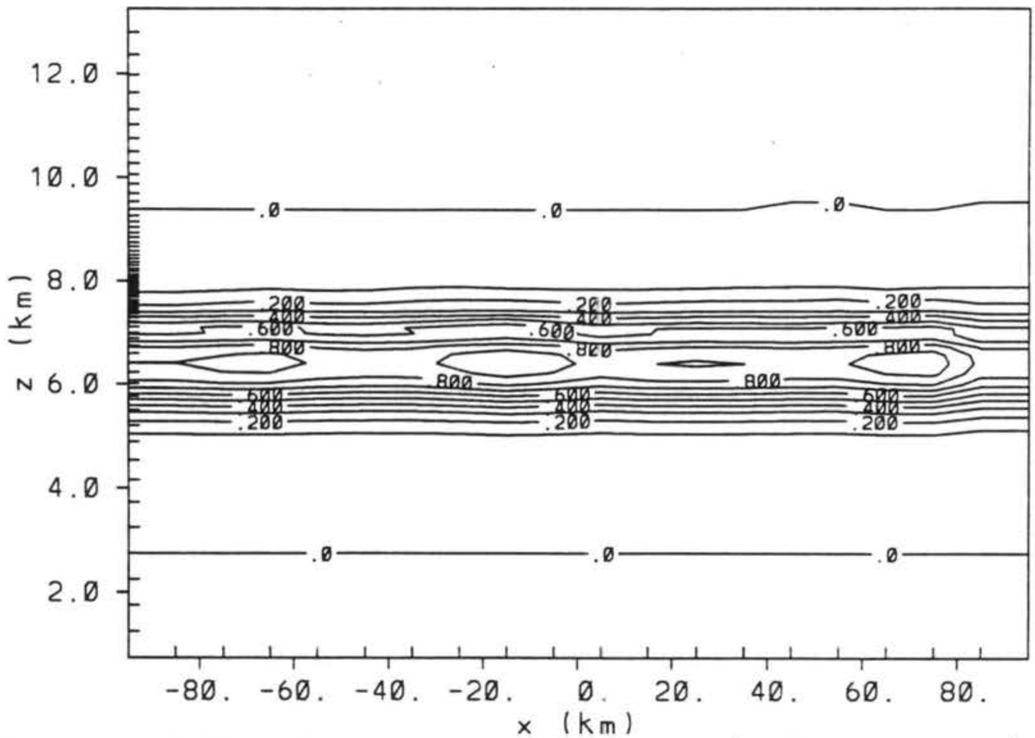

Figure 7.35: RN3 Snow Concentration. Max contour, 0.9 l^{-1} ; Min contour, 0.0 l^{-1}; Contour interval, .1E-1 l^{-1}.

Also, the simulations using this distribution shape produced larger masses near cloud base as opposed to the mid and upper cloud levels which is also more physically reasonable.

7.2.5 Rosette Crystals, Single Moment Predictions

The differences between the single moment prediction scheme and the results using the two moment scheme (control) are drastic. In order for RAMS to predict on only one moment of the size spectra, some user-defined parameter must be set; either a constant number concentration or a constant median size of the ice species must be defined. In this case, we opt to allow pristine ice to use two moment prediction because of ice initiation processes. Instead of pristine ice flux into the snow distirbution, the distribution size is kept in bounds by not allowing the mean diameter of the pristine ice particles to go beyond the D_b threshold. This is accomplished by conserving mass when the distribution gets too large and adjusting number concentration to compensate. Mass mixing ratio is predicted for snow and aggregates and number concentration is diagnosed from the specified mean diameter.

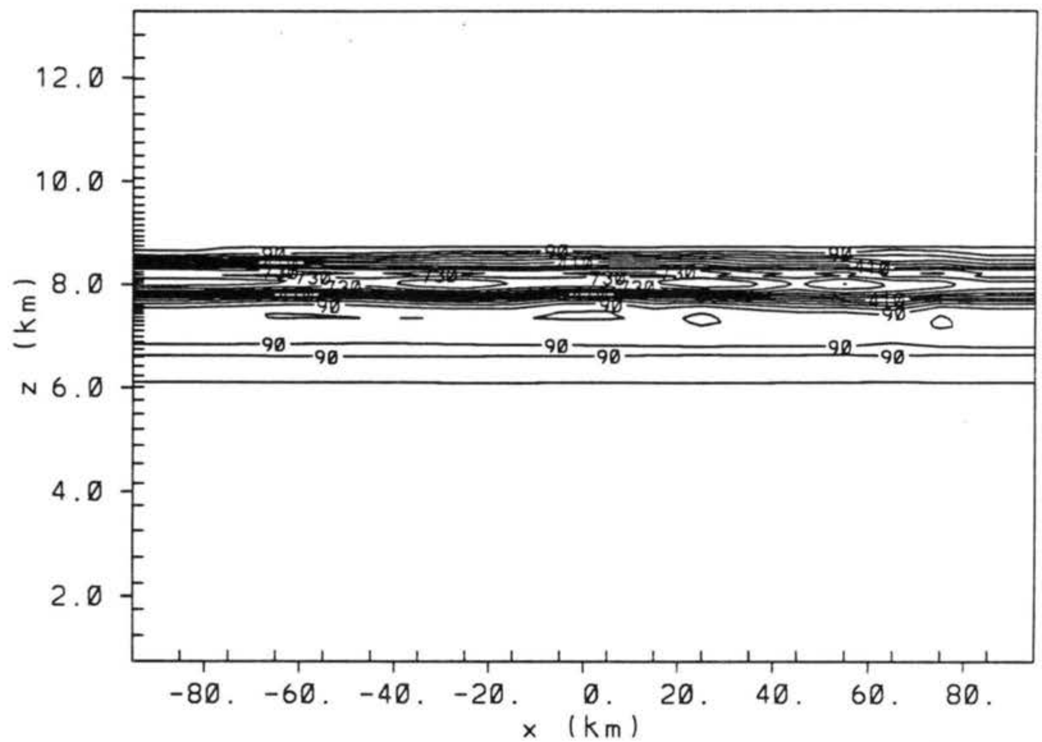

Figure 7.36: RSM Pristine Ice Mixing Ratio. Max contour, 0.89E-5 kg/kg; Min contour, 0.1E-6 kg/kg; Contour interval, 0.8E-6 kg/kg.

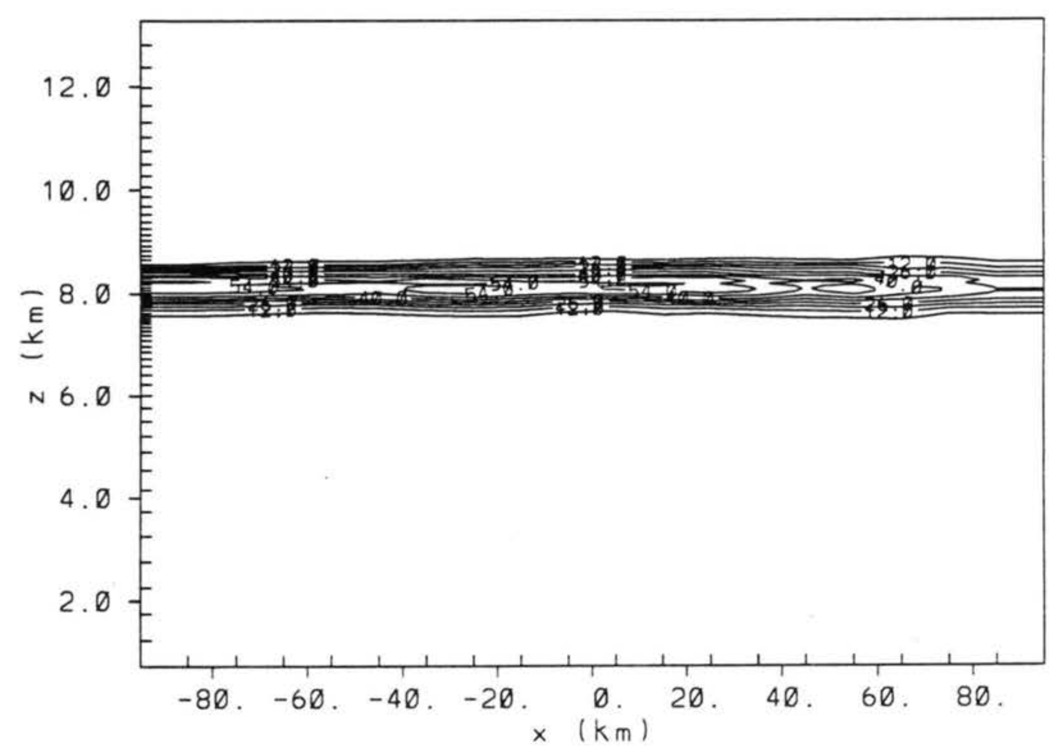

Figure 7.37: RSM Pristine Ice Concentration. Max contour, 61 l^{-1} ; Min contour, 5 l^{-1}; Contour interval, 7 l^{-1}.

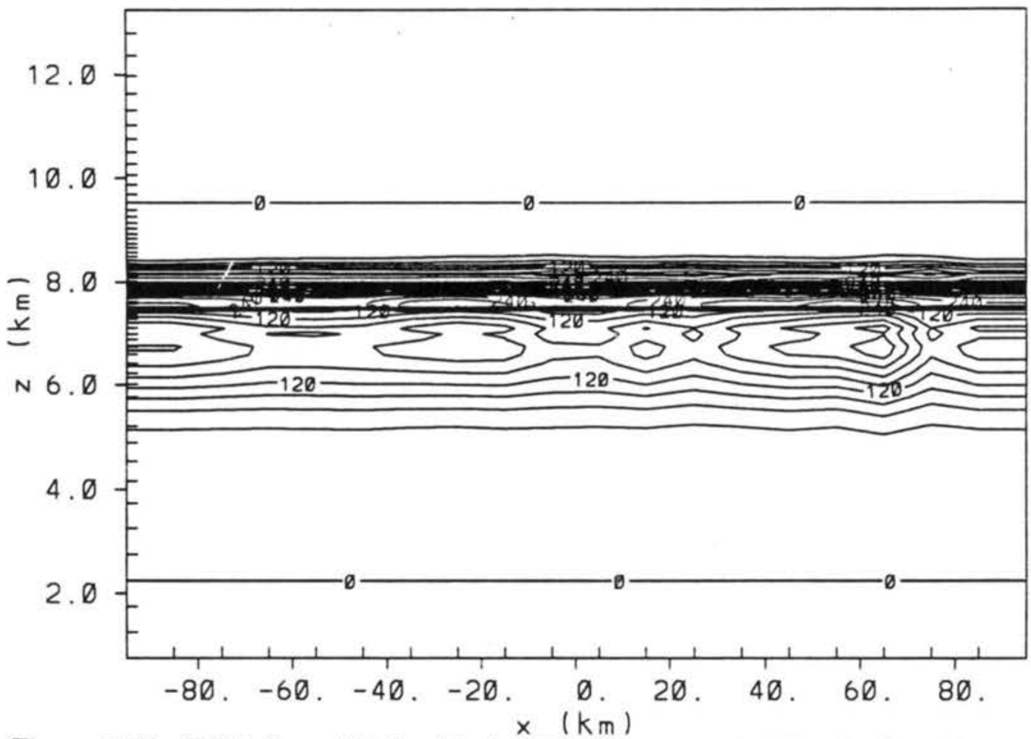

Figure 7.38: RSM Snow Mixing Ratio. Max contour, 0.48E-6 kg/kg; Min contour, 0.0 kg/kg; Contour interval, 0.3E-7 kg/kg.

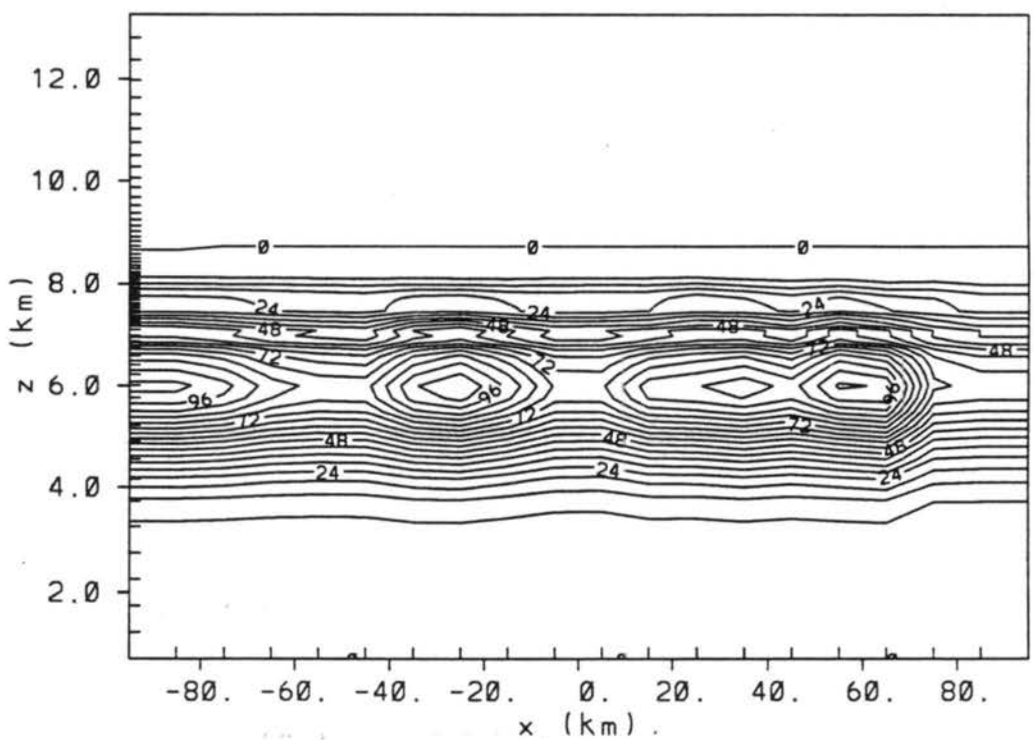

Figure 7.39: RSM Aggregate Mixing Ratio. Max contour, 0.11E-5 kg/kg; Min contour, 0.0 kg/kg; Contour interval, 0.6E-7 kg/kg.

Observations have shown crystals in cirrus for the November 26 case to be up to 400 μm (see Figure 6.10) in size. This number seems reasonable, thus, snow and aggregates are assumed to be 400 μm in sizes for this simulation.

The pristine ice mixing ratio for the single momemnt predictions (RSM) (Figure 7.36) show mixing ratio maxima that are about half that of the control simulation. Comparisons of the pristine ice concentrations produced by the RSM simulation (Figure 7.37) and the control simulation (Figure 7.5) shows much less structure produced by the single moment scheme and lower number concentrations through a thinner pristine ice layer. The snow mixing ratio shown in Figure 7.38 is similarly lower in magnitude than that produced by the control. The model produced aggregate field of mass mixing ratio (Figure 7.39) is much larger than that produced by the control simulation (Figure 7.10) and includes only one maxima in the fields (around 6 km). The reasons for the differences are easily explained. In the case of the single moment scheme, the sizes of snow and aggregates are set at the aforementioned values. So, for any given transfer process these values must be conserved; this puts constraints on the transfer processes itself.

Since larger masses must be transfered to conserve the set sizes of the crystals, the number concentrations that are removed from the pristine ice distribution are larger. Also, vapor depositional growth rates are much larger initially for the snow and aggregates in this simulation since the sizes of these ice species are set mean values. For the control simulation, vapor depositional growth rates will be much less since their sizes will be smaller initially. This constant value of the mean size of the larger ice species artifically depleats the available vapor which in turn hinders the ice initiation processes. Since aggregates have a larger initial size, collection in order to keep the set size of aggregates high must be large, this would reduce the size and masses of both pristine ice and snow. This is shown to occur in Table 7.3 where it can be seen that aggregates have much larger maxima in mass mixing ratio than in the control simulation. This artifical process of conserving the mean size (or spread) of the ice crystal spectra as is done in the single moment scheme obviously limits the results possible by the model.

7.2.6 Rosettes without the Radiative Parameterization

Radiative effects are important to the formation and maintenance of real atmospheric cirrus cloud systems. Thus, it should seem that the radiative parameterization used in a numerical model for the prediction of these clouds would be of equal importance. The following figures demonstrate this well. The total ice produced without the use of the model radiative parameterization is lower than any other simulation except the simulation without homogeneous nucelation (Tables 7.2 and 7.3).

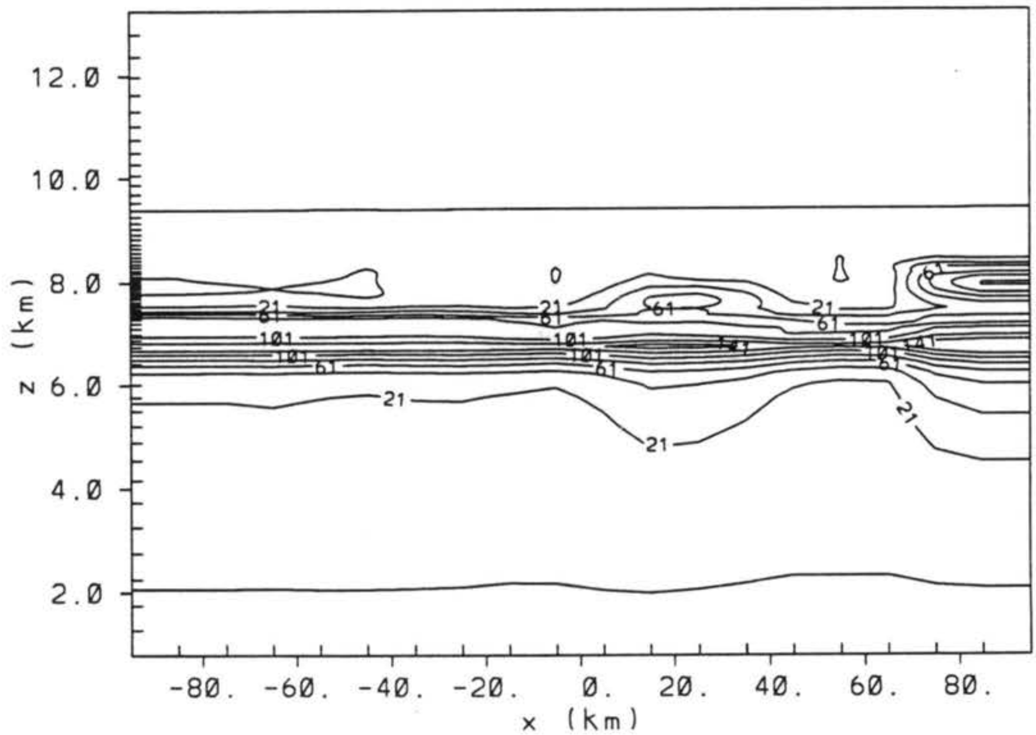

Figure 7.40: RNR Total Ice Mixing Ratio. Max contour, 0.14E-5 kg/kg; Min contour, 0.1E-7 kg/kg; Contour interval, 0.2E-6 kg/kg.

Note that the fields of pristine ice and snow concentration (Figures 7.41 and 7.42) are similarly low. All of these fields lack the structure evident in the control simulation. Examination of the w profile given in Figure 7.43 in comparison to that of the control simulation (Figure 7.14) shows that the updraft (downdraft) field is much less structured and contains much smaller updraft and downdraft maxima.

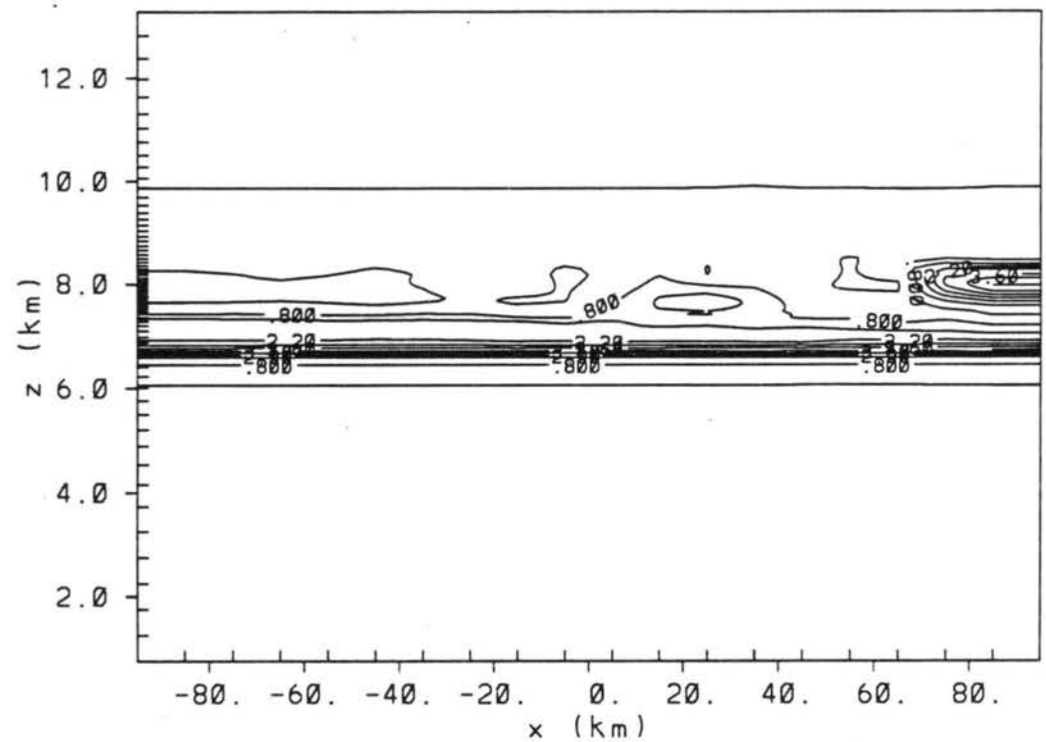

Figure 7.41: RNR Pristine Ice Concentration. Max contour, 5.7 l^{-1} ; Min contour, 0.1 l^{-1}; Contour interval, 0.7 l^{-1}.

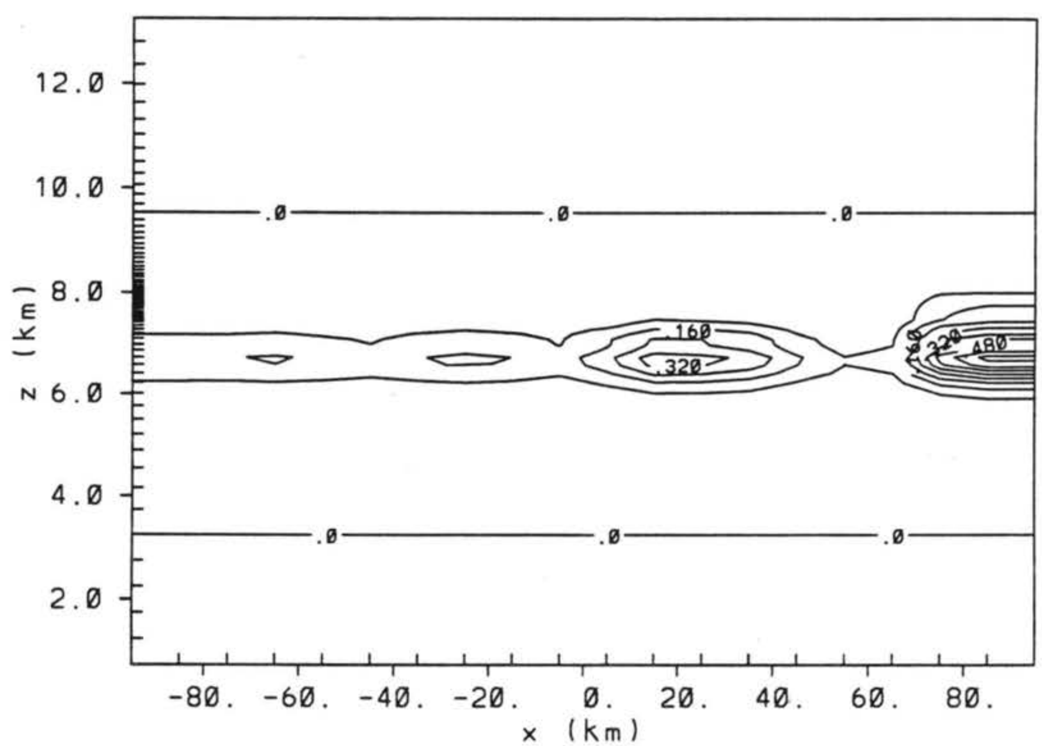

Figure 7.42: RNR Snow Concentration. Max contour, 0.64 l^{-1} ; Min contour, 0.0 l^{-1}; Contour interval, 0.08 l^{-1}.

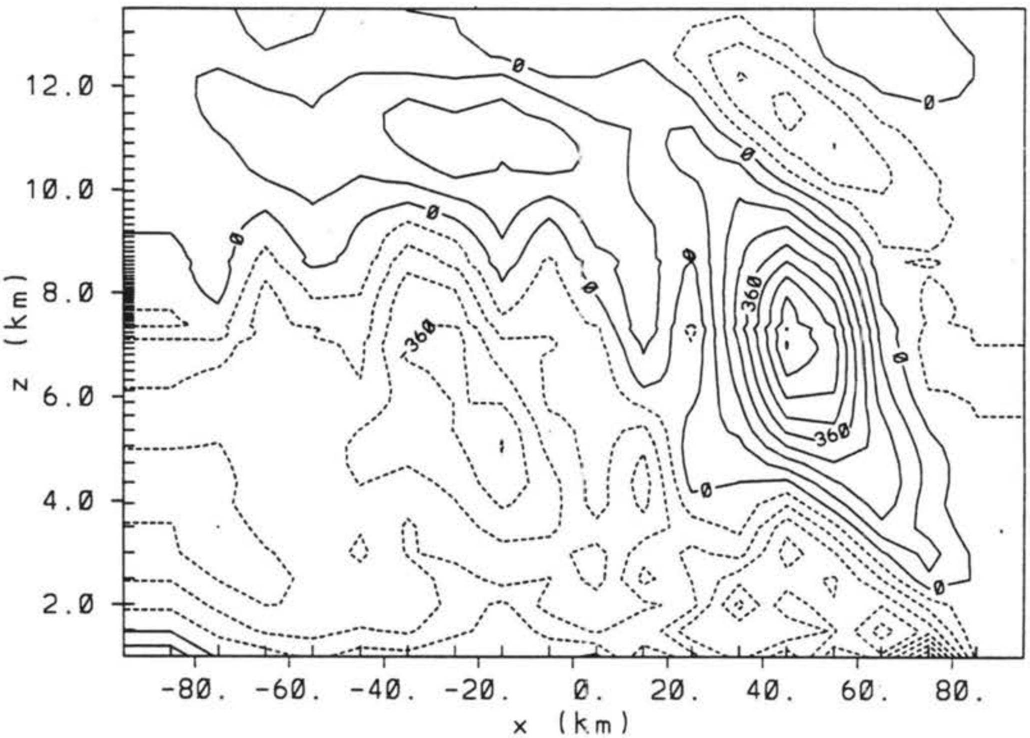

Figure 7.43: RNR W Fields. Max contour, 0.72E-2 m/s; Min contour, -0.72E-2 m/s; Contour interval, 0.9E-3 m/s.

Without the radiative parameterization, cloud top cooling does not occur; this cooling helps to increase the convection in the cirrus layer and ice initiation near cloud top (due to the colder temperatures). Obviously, the radiative parameterization is a major element in the forcing of vertical motion and in the developement of the structure of the cirrus cloud layer.

7.2.7 Rosettes without Homogeneous Nucleation

The effects of homogeneous nucleation on the control simulation is examined here by turning off homogeneous nucleation in the model but allowing heterogeneous nucelation to proceed. Total ice masses (Figure 7.44) and pristine ice and snow concentrations (Figures 7.45 and 7.46) are of much smaller maginitudes and show much less structure than their counter-parts in the control simulation. Note that pristine ice concentration maxima appear at lower altitudes (about 6.7 km) than in the control simulation. At the level where the gradient in

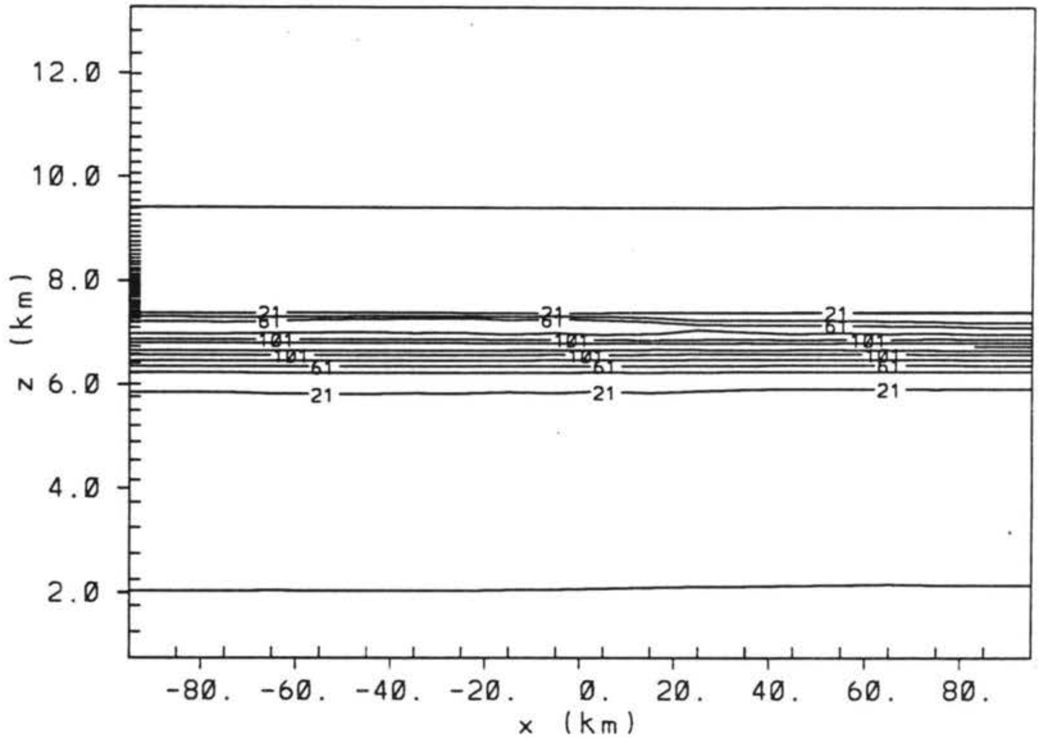

Figure 7.44: RNH Total Ice Mixing Ratio. Max contour, 0.14E-5 kg/kg; Min contour, 0.1E-7 kg/kg; Contour interval, 0.2E-6 kg/kg.

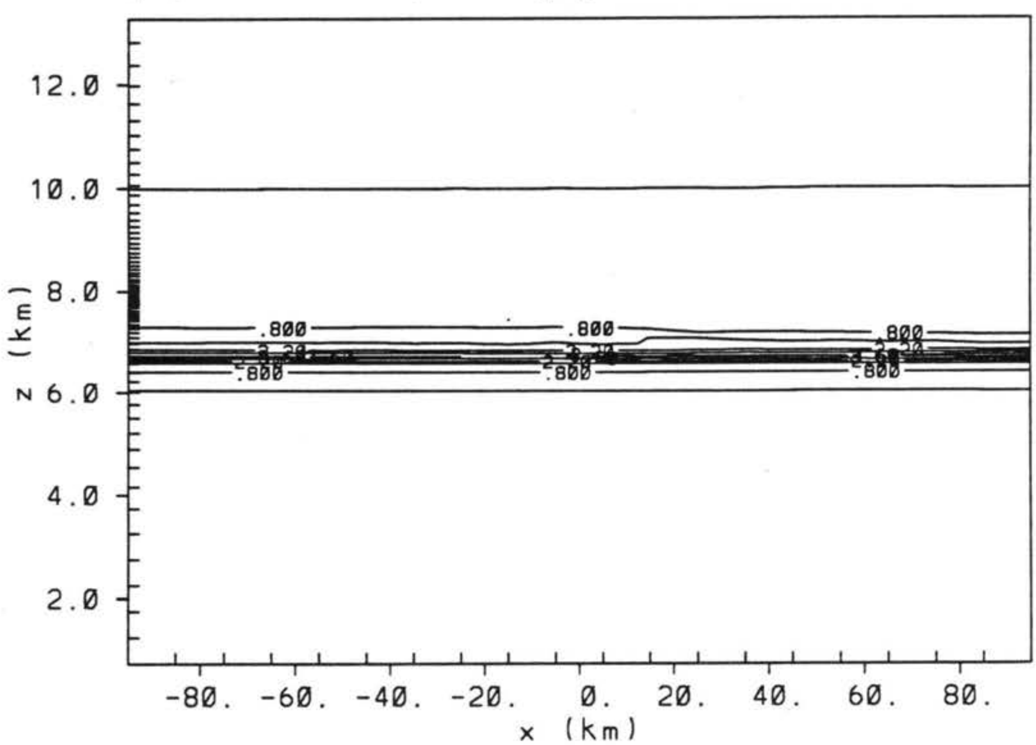

Figure 7.45: RNH Pristine Ice Concentration. Max contour, 5.7 l^{-1} ; Min contour, 0.1 l^{-1}; Contour interval, 0.7 l^{-1}.

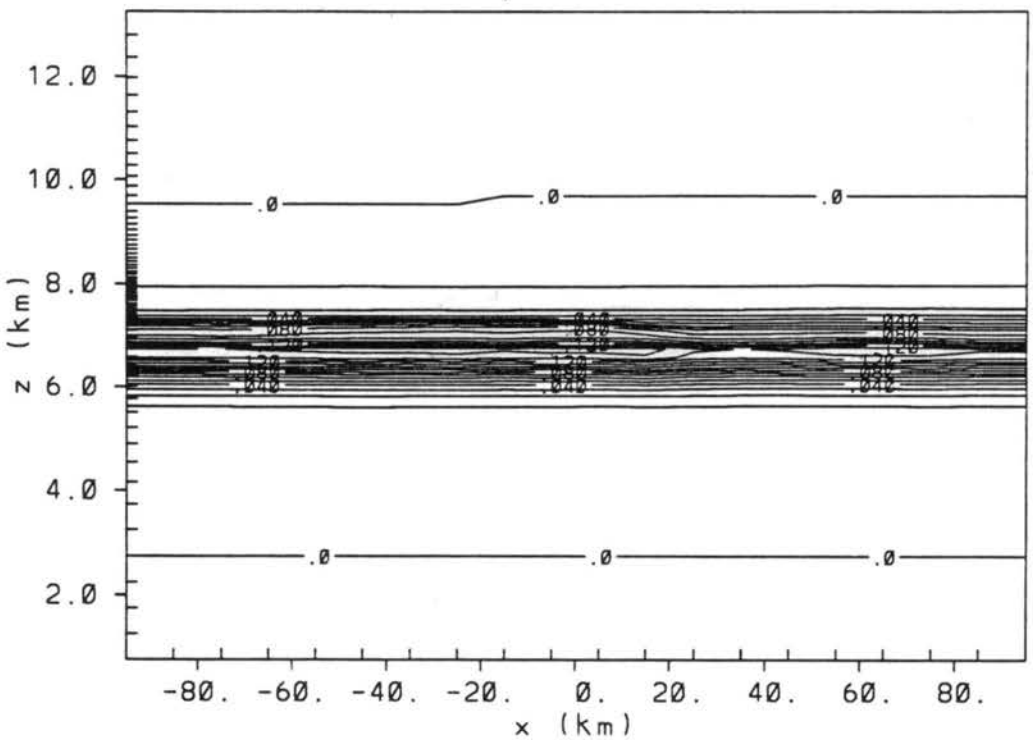

Figure 7.46: RNH Snow Concentration. Max contour, 0.14 l^{-1} ; Min contour, 0.0 l^{-1}; Contour interval, 0.01 l^{-1}.

the pristine ice fields is largest (6 to 7 km) is the level where the model relative humidity increases to values exceeding ice saturation. Since ice nuclei taper with height, we expect the heighest concentrations in pristine ice to occur at these lower levels, where relative humidities and ice nuclei concentrations are high.

The tapering of ice nuclei explains the decrease in ice species above the 7 km level. Snow crystals and total ice are also associated with these lower altitudes since the processes that produce the snow are linked directly to the pristine ice fields. Tables 7.2 and 7.3 show that snow and aggregate sizes are quite large for both the 2 hour and 5 hour model times. This is due to the fact that not many ice crystals are initiated by just the heterogeneous process. Thus, there is less competition for the available vapor; more is available for the vapor depositional growth of the ice crystals. Obviously, the homogeneous nucelation scheme contributes significantly to the model cirrus simulations.

7.2.8 Needles with a Modified Sounding

In order to examine the effects of perturbations in the RH fields to the overall effects of the cirrus simulation, runs are done in which the relative humidity in cloud is increased by 5 %. The total ice field produced by the model is shown in Figure 7.47 and contains maxima that are larger than those produced by the NN1 simulation (Figure 7.22). The modified sounding field shows much more structure in cloud, however the cloud base does not drop as low as it does in the case of the NN1 simulation. As is shown in Table 7.3, the diameters of snow and aggregates neven reach the sizes as in the NN1 "control" run; this is why the cloud base is higher in this simulation. Also, at these higher saturations, there is a lot of initial ice nucelation (Table 7.2 shows concentrations of pristine ice up to 9500 l^{-1}) that depleates the available vapor. Thus, most of the ice stays in the pristine ice category (Table 7.3 shows these values) at smaller sizes. Most of the mass should then be associated with the upper cloud level; this is verified by Figure 7.47. Figures 7.48 and 7.49 both show maxima in number concentration in the mid to upper cloud levels. The pristine ice fields show more structure than the NN1 simulation; pristine ice concentrations reach large values (up to 7200 l^{-1} in the 9 km region while snow concentrations stay relatively small. Since the high nucleation rates depleate the available water vapor, the pristine ice distribution is relatively narrow and can be seen in Figure 7.50; high number concentrations and mixing ratios result in smaller ice crystal sizes. This shows that the bulk of the mass and number concentration is associated with smaller sizes (around 20 μm). This narrow distribution coupled with the lower vapor depositional growth rates due to the high vapor competition causes the low transfer rates and, consequently, the low snow mass and number concentrations observed in the simulation.

The sounding values input into the model are quite important to the simulation of the cirrus system. As is shown in this simulation, the values of the meterological conditions put into the model can drastically affect the results.

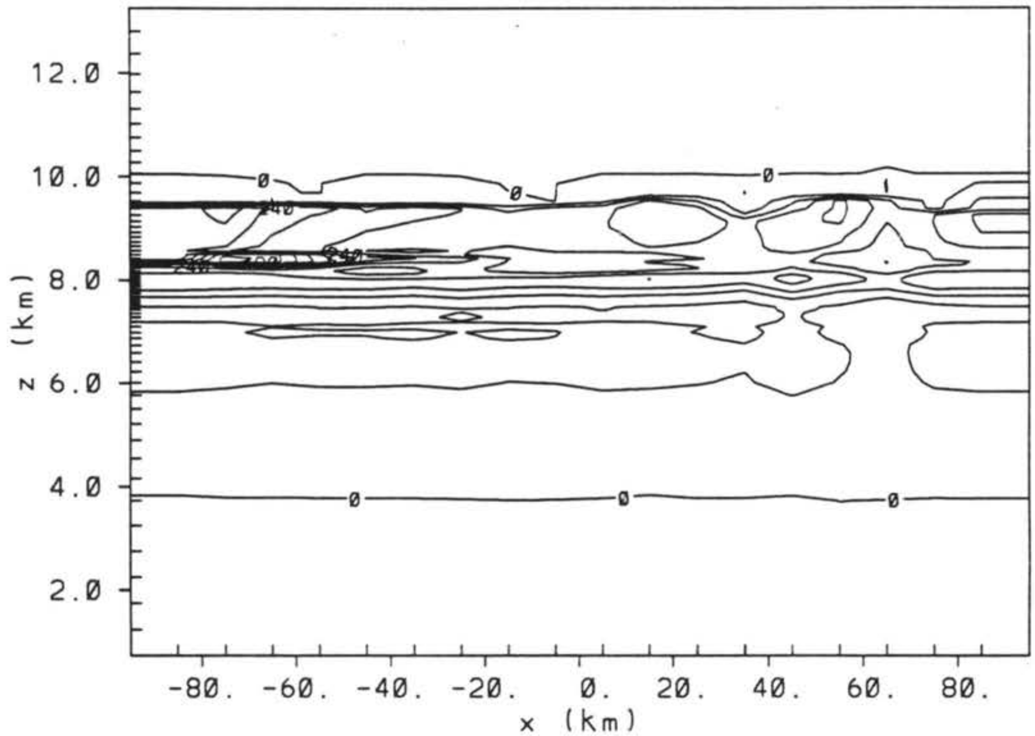

Figure 7.47: N5RH Total Ice Mixing Ratio. Max contour, 0.66E-4 kg/kg; Min contour, 0.1E-7 kg/kg; Contour interval, 0.6E-5 kg/kg.

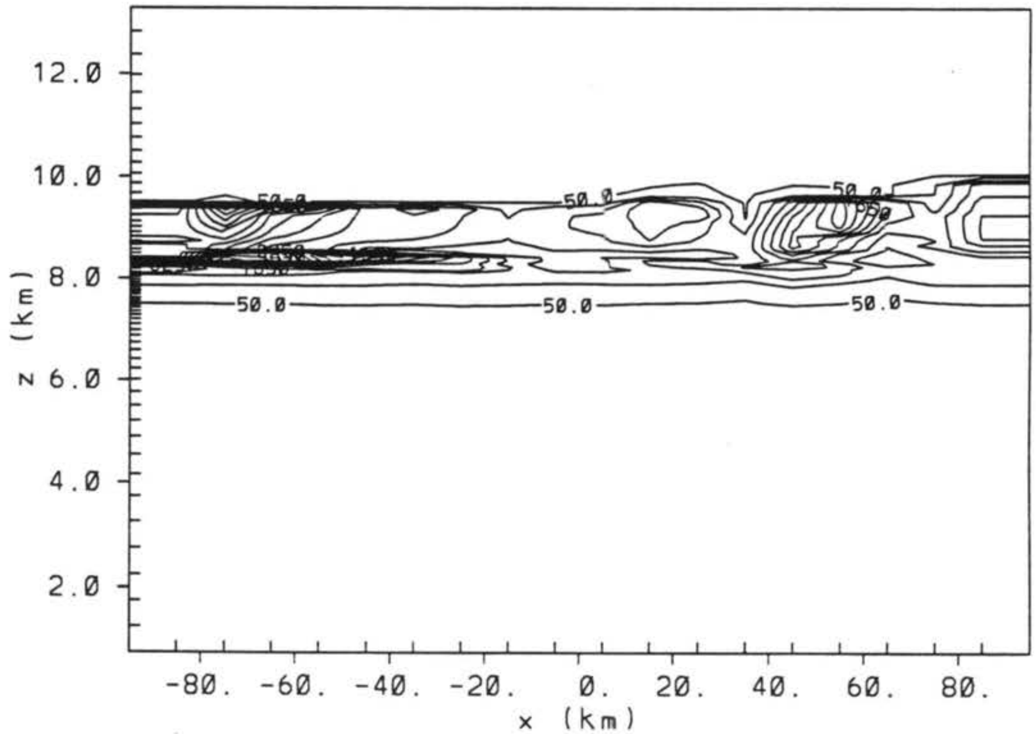

Figure 7.48: N5RH Pristine Ice Concentration. Max contour, 7200 l^{-1} ; Min contour, 50 l^{-1}; Contour interval, 400 l^{-1}.

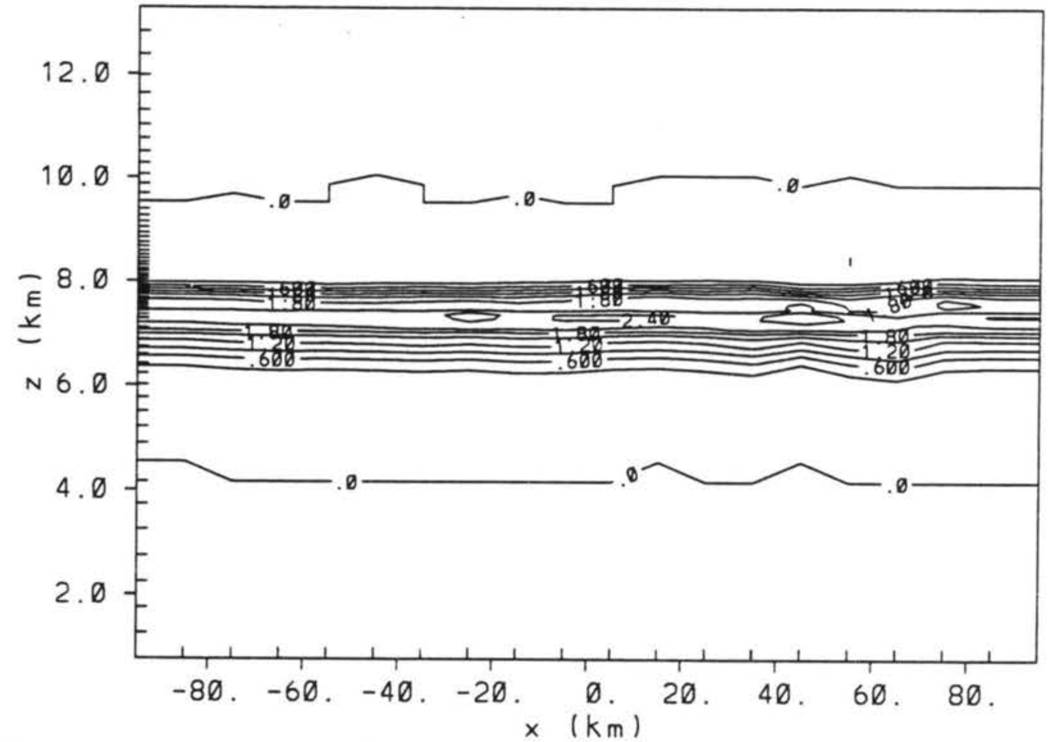

Figure 7.49: N5RH Snow Concentration. Max contour, 2.4 l^{-1} ; Min contour, 0.0 l^{-1}; Contour interval, 0.3 l^{-1}.

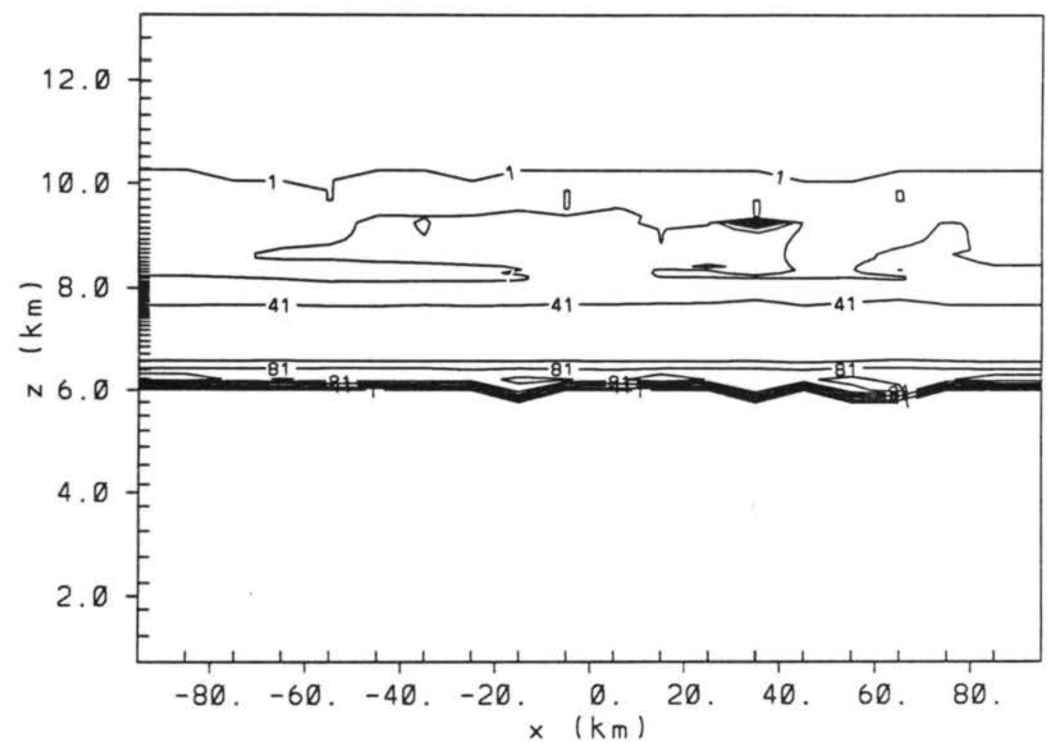

Figure 7.50: N5RH Pristine Ice Size. Max contour, 121 μm; Min contour, 1 μm; Contour interval, 20 μm.

7.2.9 Rosettes with Perturbed Ice Nuclei Profile

To simulate the effect of perturbed ice nuclei profiles influencing the nucleation of ice in the upper troposphere, we have modified the model ice nuclei profile by not tapering it with height (as was done in the previous simulations) and using the ground based value throughout the depth of the troposphere. The simulation shows the effects of ice nuclei injection from natural and anthropogenic sources (high flying aircraft, volcanic debris, etc...) on the control simulation.

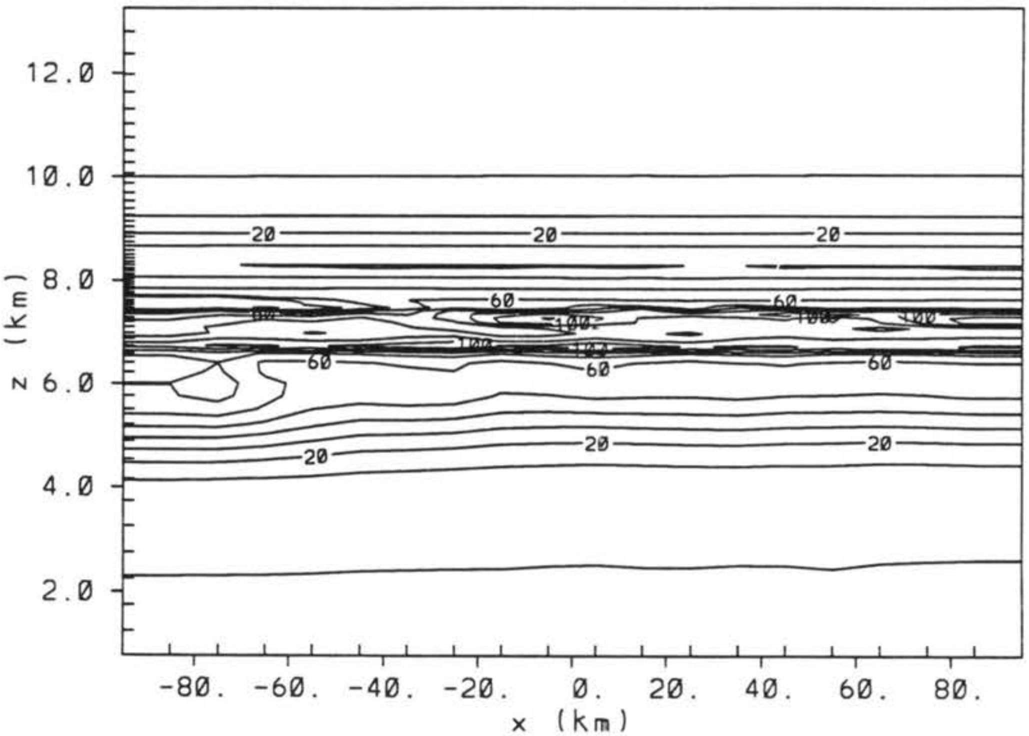

Figure 7.51: RCIN Total Ice Mixing Ratio. Max contour, 0.14E-4 kg/kg; Min contour, 0.1E-7 kg/kg; Contour interval, 0.1E-5 kg/kg.

Figure 7.51 shows the model produced total ice fields. In comparison to the control simulation results (Figure 7.13), total mixing ratios are similar, however in the RCIN simulation the maxima in ice mixing ratio occur near mid-cloud (about 7 km) while the control has maxima between 8.5 and 9 km. The vertical extent of the simulated cloud is deeper, even though the sizes of the snow and aggregates are less than the control run (Table 7.3). The pristine ice concentration field (Figure 7.52) contains two areas of maxima; one near 9.5 km and the second around 7 km. Snow concentrations presented in Figure 7.53, show lower concentrations with less vertical extent than the control simulation. The reason for lower ice concentrations and ice sizes in these simulations has to do with the increased competition for vapor by the larger concentration of IN at cirrus levels. These IN compete for the available vapor and hinder homogeneous nucleation; which we have already seen as a large contributor to ice in these simulations.

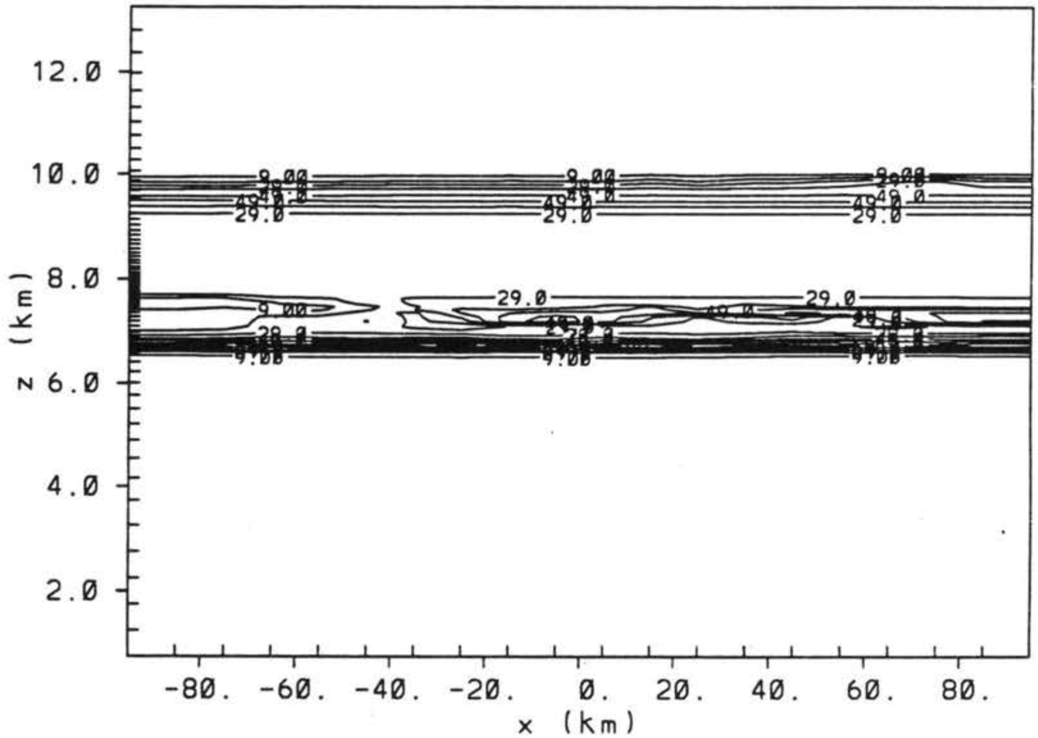

Figure 7.52: RCIN Pristine Ice Concentration. Max contour, 89 l^{-1} ; Min contour, 9 l^{-1}; Contour interval, 10 l^{-1}.

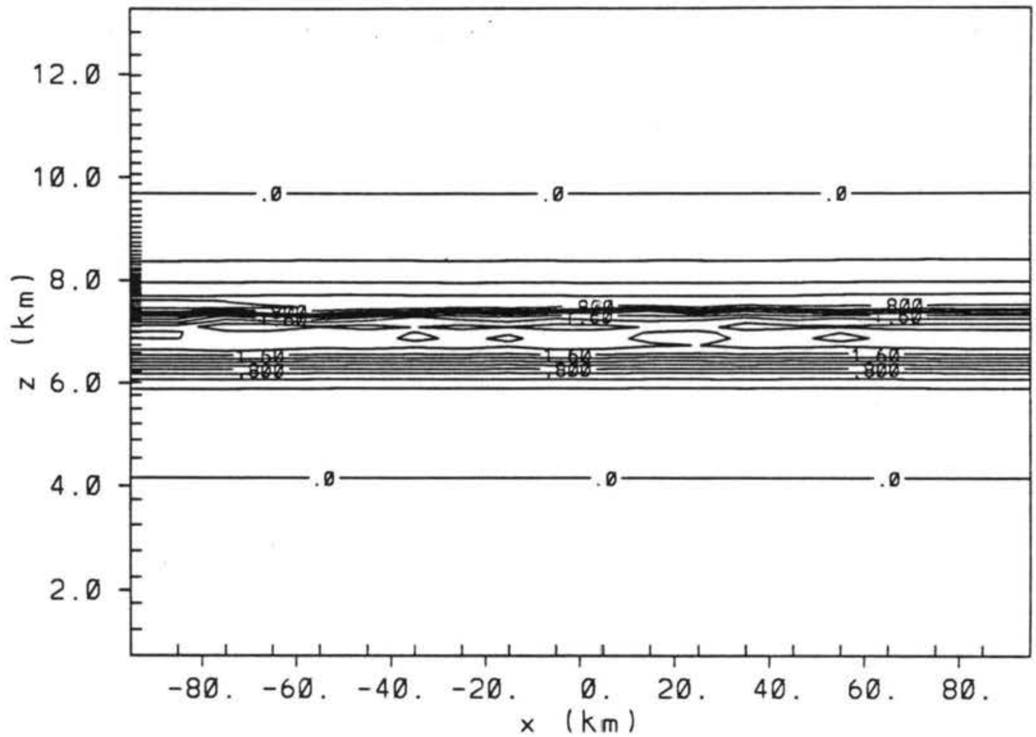

Figure 7.53: RCIN Snow Concentration. Max contour, 2 l^{-1} ; Min contour, 0.0 l^{-1}; Contour interval, 0.2 l^{-1}.

Chapter 8

SUMMARY AND CONCLUSIONS

8.1 Conclusions

The accurate prediction of cirrus cloud microphysical properties is important for a number of reasons. First of all, there exists the current "climate problem". The climate effects of various perturbations in the earth-atmosphere-ocean system is, in general, difficult to understand without the aid of numerical modeling. It is important to derive reasonable parameterizations of the microphysics of clouds, such as in the case of cirrus clouds described here, to better understand the radiative feedback effects. Cirrus clouds are globally frequent and, as stated by Stephens et al. (1990) and Mitchell (1994), their complex microphysical properties and radiative interactions makes credible parameterizations of these processes important. On a more practical side, predictions of cirrus clouds and their microphysical properties has importance to the aviation industry. As was noted by Sassen (1992), aircraft flying at cirrus levels have detected significant wing icing (evidence of supercooled liquid water at these levels). The difficulties in the modeling of ice clouds are, on a physical level, quite large. Cirrus clouds contain various ice crystal habits and understanding variations in these habits is a must to better simulate these systems. Ice crystals have very complex growth kinetics in vapor fields, and the interaction between the various habits with radiation is quite complex.

In this study we have presented a parameterization of ice crystal conversion processes for cirrus cloud modeling. This process is based on two-moment basis functions describing the hydromemtor species. Two categories are defined, pristine ice and snow, with each species described by separate, complete gamma functions. Pristine ice is, as its name describes, pristine in it's modeled nature; these crystals are assumed to grow only by vapor deposition and are initiated by both heterogeneous and homogeneous processes. Since vapor deposition is the only growth mode of pristine ice, transfer equatiions are developed for the flux of pristine ice number concentration and mass mixing ratio between the two distributions for both ice supersaturated and subsaturated atmospheric regimes. A number sink for the smallest pristine ice and snow crystals existing in ice subsaturated regimes is parameterized by a function of the form,

$$N_f = f(r_f, habit, \nu) \tag{8.1}$$

where N_f is the fractional number concentraiton loss, r_f is the fractional mass loss and ν is the distribution shape parameter. A bin model is calculated to test the supposition that N_f depends only on the above parameters. The tests show that the above variables are the most important for the parameterization. Since cost-efficient analytical expressions may be impossible to formulate for this function, values are calculated and stored in look-up table format.

The one-dimensional Lagrangian model described in Tripoli and Cotton (1982) was used for simple tests of the transfer and sublimational number loss schemes. The model is a simple parcel model that calculates the distribution evolutions during an ice saturated ascent and an ice subsaturated descent between two user-defined atmospheric pressure levels. The distributions are allowed to evolve due to vapor depositional growth (sublimation). Tests were run for needle and plate crystals using various values of the distribution shape parameter, ν. The simulations showed the sensitivity of ice crystal habit and distribution shape parameter to the evolution of the distributions. The results showed that, as one would expect, a larger value of ν tends to increase the mass growth of the distribution since the larger particles in the distribution are weighted more. Crystals with a smaller value of β in the mass-dimensional relationship tend to grow faster in maximum dimension with a lesser increase in mass. This causes greater fluxes of number concentrations (but not necessarily mass) to snow in ice supersaturated regimes, as compared to runs with larger values of β. The distribution of pristine ice needles, therefore, exhibited lesser number concentrations with larger mean particle sizes as compared to plates (which have a larger β value). One way to think of this is that with a smaller value of the mass-dimensional exponent, a given increase in mass, Δm, is distributed over a smaller surface area than for crystals with larger β values. Thus, the needles will gain size faster but not necessarily mass. Mitchell (1994) noted similar effects in his two-dimensional explicit cirrus cloud simulations; he noted that "more spatial" habits (habits with larger β values, such as rosettes or speheres) tended to have higher number concentrations as compared to the less spatial habits, such as needles or columns.

The transfer and sublimation number concentration loss schemes were implemented into the RAMS model (the sublimation scheme was made general so that it included all ice hydrometeor species) and two-dimensional tests were run using sounding data from the FIRE II experiment in Coffeyville, Kansas for the November 26, 1991 cirrus event. The model grid domain consisted of 20 points in the x (east-west) direction with a grid spacing of 10 km and 74 points in the vertical with a grid spacing starting at 1500 m at the ground, shrinking this to 50 m at 8 km, and then stretching back to 1500 m at 14 km. The sounding used was modified in the 6 to 10 km levels since it was noted by Heymsfield et al. (1993) that the rawindsonde data was in error generally by about 20 % in cloud (the rawindsonde data was consistently below ice saturation levels). A heirarchy was constructed for the test simulations which consisited of the following parts: 1) control simulation for comparistion with radar and lidar observations of the November 26, 1991 case; 2) variations in the various model parameterizations to test their effects on the simulations of cirrus clouds with the RAMS model.

The control simulation consisited of a cloud made up of rosette crystals, distribution shapes are assumed exponential, homogeneous and hetereogeneous nucelation are utilized and the radiative parameterization (Chen and Cotton, 1983) is used. The model allows for variations in these crystalline habits, but this parameterization is foregone here since tests of the sensitivity of the model to different crystalline habits is important; also the control could have been run with different values of ν, however keeping all of the values of ν the same for the control simulation seemed the best way to isolate the tests.

The control simulation compared quite well wtih observations. After 2 hours of simulation maximum ice concentrations were 270 l^{-1}, masses and vertical motions were small. The number concentrations were small in comparision to observations, however, there is a certain degree of model "spin-up" time that needs to be considered. Cloud base at this time had dropped to around 6 km. After 5 hours of simulation crystal concentrations had maximum values of 960 l^{-1}, IWC were around 0.28×10^{-1} g/kg (or 0.02 g m^{-3}), and cloud base was down to about 3 km. The values of the ice crystal number concentrations and masses compared very favorably to lidar and radar studies if this system. The control simulation also predicted small ice sizes (20-40 μm) near cloud top with larger sizes near cloud base (1000 μm). A time-series plot of the modeled cirrus layer shows the cloud initially at about 8km and having a very thin vertical structure. After about 2 hours the cloud deepens to around 6km, and after the full 6 hours of simulation the cloud base has dropped to around 2.5-3km while cloud top has remained fairly constant at 9-9.5 km. This time-series compares favorably with radar-echo boundaries observed during the FIRE II Noveber 26 cirrus case.

Sensitivity tests were run to understand the effects of variations in certain parameterizations on the simulated cirrus system. Variations in the crystalline habit (needles and plates were substituted for rosettes) had the effect of decreasing the simulated number concetrations and mass mixing ratios of the cloud deck. Also, cloud depths were not as great and cloud structure was more homogeneous for these simulations. These variations were attributed to the differences in the mass-dimensional exponent, modeled updraft profiles, and to the different growth kinetics of the crystalline habits. To test variations in distribution shape parameters, the value of ν was set to 3 for the larger ice species (snow and aggregates). The larger value of the shape parameter has the effect of weighting mass gain by collection and vapor depositional growth of these distributions more than in the $\nu = 1$ counterparts. Masses of the ice fields were lower than the control after 5 hours of simulation due to the increased depleation of the vapor field by the snow and aggregate distributions. Since the snow and aggregate distributions are weighted more due to the larger value of ν, the masses of pristine ice, snow and aggregates are comparable in this simulation as compared to the control in which pristine ice mass dominates. Maxima in masses are in the mid to lower cloud regions, as shown by observations. This is a reason for considering using larger shape parameters for larger ice species in the model. Also, number concentrations of pristine ice and snow were lower than the control and can be attributed to less nucleation due to more vapor depletion by the larger hydrometeors and larger transfer rates.

The single moment prediction scheme was used to show the importance of two-moment predictions. The fields produced were much less structured than the control and contained lower number concentrations and ice masses. This is attributed to the snow and aggregates starting with a much larger value of their mean size than they would in the two-moment scheme. The artifical constraint tends to depleate the available vapor (thus constraining ice production) and artificially increases collection and ice transfer between pristine ice and snow. The simulations in which the radiative parameterization was turned off shows a very homogeneous field with low ice mass, high cloud base and low number concentrations. Without the radiative parameterization, cloud top cooling does not occur. This would tend to supress nucleation at cloud top and, as the w fields showed, decreases the converction in the cloud. Thus, the radiative parameterization is important to the initiation and maintenance of the modeled cirrus layer. The simulation in which the homogeneous nucleation parameterization was turned off showed that model nucleation was dominated by this process. This simulation produced a much thinner cloud than the control.

A simulation in which the RH field in cloud was perturbed systematically by 5% shows how important the initial moisture profile is to model simulations. The cirrus cloud ice mass was much higher than the needle simulation without the perturbed RH values. The cloud depth was larger, however pristine ice sizes were small as were concentrations of snow and aggregates. This was attributed to the nucleation processes in the model. Nucleation rates were so high throughout the simulation that pristine ice crystals remained small. Even though there was plenty of vapor for the transfer equations, nucleation kept the number concentrations of pristine ice high enough so that pristine ice sizes were small, thus mass and number concentrations were transfered to snow. This was verified by the large ice mass and number concentrations near cloud top, associated with small mean pristine ice sizes. The final test that was run utilized a perturbed IN profile to simulate aerosol perturbations. The results of the model showed that the IN competition for the available vapor was large enough to hinder the homogeneous nucelation processes. The overall effect of which produced a homogeneous cloud layer with a vertical extent from above 10km to 4 km. This IN perturbation caused slow ice transfer rates and smaller overall masses to be produced.

These simulations show the not only the flexibility of the RAMS model in upper level cloud simulations, but also its ability to produce reasonable cirrus cloud fields. The control simulation produced values and contoured fields that agree well with lidar and radar measurements of the observed cirrus microphysical fields. Vertical motion fields were low in comparison to observations, however, the major driving force of the vertical velocities was the cloud top radiative cooling induced with the Chen and Cotton (1983) radiative parameterization. It is not unreasonable to assume that 3-D modeling studies would produce better vertical motion fields due mechanical forcing of the vertical winds. The sensitivity tests that were run show the varied sensitivity of the model to many different changes in the model parameterizations. In order to produce credible simulations of these systems, it is important to initialize the model with these values as best as one can.

8.2 Future Research

Since observations at cirrus levels are sparse and limited to few field projects, it will be important in the future to get a better understanding of the microphysical processes from an observational standpoint. Cirrus cloud particle size spectra need to be measured with a good degree of accuracy down to smaller crystal sizes. Also, more measurements of IN and nucelation processes in cirrus need to be made in order to increase the accuracy of model parameterizations. More ground based laboratory work needs to be done on these areas as well. Observations and measurements of the influences of volcanic aerosols on cirrus properties needs to be done.

On the modeling side of things, better observations make for better parameterizations! Better observations would increase the accuracy of modeled predictions of these systems.

In the future full, three-dimensional simulations of the November 25-26 and December 5-6, 1991 FIRE II cirrus cases should be carried out with the above parameterization. This would show the applicability of the new microphysics parameterizations to fully 3-D cirrus cloud simulations. A two-stream parameterization of cloud radiative transfer processes should be incorporated and run with the above cases. The two-stream model takes into account individual hydrometeor species distirbution parameters. This should increase the accurcy of the RAMS model simulations. Also, it might be important to introduce a bulk change in crystalline habit aspect ratio as discussed in Chapter 4; this would favour larger growth rates for larger crystals.

References

Ambromovitz, Milton and Irene A. Stegun, 1972: *Handbook of Mathematical Functions.* Dover Publications, INC., New York. 1046pp

Arnott, W.P., Y.Y. Dong, and J. Hallett, 1993: Cirrus microphysics observations made during FIRE II: Small particles, high concentrations, and probe comparisons. Preprints, *FIRE Cirrus Science Conf.*, June 14-17, 1993, Breckenridge, Colorado, 5-8.

Arakawa, A. and V.R. Lamb, 1981: A potential enstrophy and energy conserving scheme for the shallow water equations. *Mon. Wea. Rev.*, **109**, 18-36.

Ben-Jacob, E., Nigel Goldenfeld, J.S. Langer, and Gerd Schon, 1983: Boundary layer model of pattern formation in solidification. *Phys. Review*, **A29**, 330-340.

Berry, E.X., 1967: Cloud droplet growth by collection. *J. Atmos. Sci.,* **24**, 688-701.

Blanchard, D.C., 1957: The supercooling freezing and melting of giant water drops at terminal velocity in air. *Artificial Simulation of Rain*, Pergamon Press, 233-249.

Chen, C. and W.R. Cotton, 1983: Numerical experiments with a one-dimensional higher order turbulence model: Simulation of the wanganra day 33 case. *Boundary-Layer Meteorol.,* **25**, 375-404.

Cooper, W.A., 1980: A method of detecting contact ice nuclei using filter samples. Preprints, *Eighth International Conf. on Cloud Physics*, Clermont-Ferrand, France, 665-668.

Cotton, W.R., M.A. Stephens, T. Nehrkorn, and G.J. Tripoli, 1982: The Colorado State University three-dimensional cloud/mesoscale model - 1982. Part II: An ice phase parameterization. *J. de Rech. Atmos.*, **16**, 295-320.

Cotton, W.R., G.J. Tripoli, R.M. Rauber, and E.A. Mulvihill, 1986: Numerical simulation of the effects of varying ice crystal nucleation rates and aggregation processes on orographic snowfall. *J. Climate Appl. Meteor.,* 25, 1658-1680.

DeMott, P.J. and D.C. Rodgers, 1990: Freezing nucleation rates of dilute solution droplets measured between $-30°C$ and $-40°C$ in laboratory simulations of natural clouds. *J. Atmos. Sci.*, **47**, 1056-1064.

DeMott, P.J., M.P. Meyers, and W.R. Cotton, 1993: Parameterization and impact of ice initiation processes relevant to numerical model simulations of cirrus clouds. *J. Atmos. Sci.*, **51**, 77-90.

Deshler, T., 1982: Contact ice nucleation by submicron atmospheric aerosols. Ph.D. dissertation, Dept. of Physics and Astronomy, University of Wyoming, 107 pp.

Eadie, W.J. 1971: A molecular theory of homogeneous nucleation of ice from supercooled water. Ph.D. dissertation, University of Chicago, Cloud Physics Lab., Tech. Note 40, 117 pp.

Ferrier, B.S., 1994: A double-moment multiple-phase four-class bulk ice scheme. Part I: Description. To be published *J. Atmos. Sci.*

Flatau, P.J., G. Dalu, W.R. Cotton, G.L. Stephens, Hemsfield, 1988: Mixed layer model of cirrus clouds: Growth and dissipation mechanisms. Preprints, *Symposium on the Pole of Clouds in Atmospheric Chemistry and Global Climate*, January 29-February 3, 1989, Anaheim, CA.

Flatau, P.J., G.J. Tripoli, J. Verlinde, W.R. Cotton, 1989: The CSU-RAMS cloud microphysical module: General theory and code documentation. Colorado State University, Dept. of Atmospheric Science, Fort Collins, Colorado 80523. (Atmospheric Science Paper No. 451), 88 pp.

Flatau, P.J., I. Gultepe, G. Nastrom, W.R. Cotton, and A.J. Heymsfield, 1990: Cirrus cloud spectar and layers observed during the FIRE and GASP projects. Preprints, *Conference on cloud physics*, July 23-27, 1990, San Francisco, CA.

Fletcher, N. H., 1962: *Physics of Rain Clouds.* Cambridge Univ. Press, London, Eng.

Gultepe, I., A.J. Heymsfield, and G.V. Rao, 1990: Moisture and heat budgets of a cirrus cloud from aircraft measurements during FIRE - October 31 case study. Preprints, *Conference on cloud physics*, July 23-27, 1990, San Francisco, CA.

Heckman, Capt. Scot T., 1991: Numerical simulation of cirrus clouds – FIRE case study and sensitivity analysis. M.S. Thesis, Colorado State University, Dept. of Atmospheric Science, Fort Collins, CO 80523, 132 pp. (Atmospheric Science Paper #483)

Heckman, Scot T. and William R. Cotton, 1993: Mesoscale numerical simulations of cirrus clouds - FIRE case study and sensitivity analysis. *Mon. Wea. Rev.*, **121,** 2266-2284.

Hein, P.F., John M. Davis, and Stephen Cox, 1993: Spectral variation of scattering and absorption by cirrus. Preprints, *FIRE Cirrus Science Conf.*, June 14-17, 1993, Breckenridge, Colorado, 112-115.

Heymsfield, A.J. and R.G. Knollenberg, 1972: Properties of cirrus generating cells. *J. Atmos. Sci.*, **29,** 1358-1366.

Heymsfield, Andrew, 1975: Cirrus uncinus generating cells and the evolution of cirriform clouds. Part II: The structure and circulations of the cirrus uncinus generating head. *J. Atmos. Sci.*, **32,** 809-819.

Heymsfield, Andrew J. and Robert M. Sabin, 1989: Cirrus crystal nucleation by homogeneous freezing of solution drops. *J. Atmos. Sci.*, **46,** 2252-2264.

Heymsfield, Andrew J. and Larry M. Milloshevich, 1993: Overview of microphysical and state parameter measurements from FIRE II. Preprints, *FIRE Cirrus Science Conf.*, June 14-17, 1993, Breckenridge, Colorado, 1-4.

Huffman, P.J., 1973: Supersaturation dependence of ice nucleation by deposition for silver iodide and natural aerosols. Report No. AR 108, 29 pp.

Huffman, P.J., 1973: Supersaturation spectra of AgI and natural ice nuclei. *J. Appl. Metero.*, **12**, 1080-1087.

Huffman, P. J. and G. Vali, 1973: The effect of vapor depletion on ice nucleus measurements with membrane filters. *J. Appl. Meteor.*, **12**, 1018-1024.

Intrieri, Janet M. and Graham Feingold, 1993: Lidar and radar derived cirrus microphysical properties for the 26 November 1991 case study. Preprints, *FIRE Cirrus Science Conf.*, June 14-17, 1993, Breckenridge, Colorado, 48-51.

Klemp, J.B. and R.B. Wilhelmson, 1978: The simulation of three-dimensional convective storm dynamics. *J. Atmos. Sci.*, **35**, 1070-1096.

Langer, J.S., 1980: Instabilities and pattern formation in crystal growth. *Rev. Modern Phys.*, **52**, 1-28.

Levinson, David H., 1993: CO_2 lidar observations of Mount Pinatubo debris: FIRE II and longer-term measurements. Preprints, *FIRE Cirrus Science Conf.*, June 14-17, 1993, Breckenridge, Colorado, 130-133.

Lilly, Douglas K., 1988: Cirrus outflow dynamics. *J. Atmos. Sci.*, **45**, 1594-1605.

Mace, Gerald G. and Thomas P. Ackerman 1993: Cirrus cloud developement in a mobile upper tropospheric trough: The November 26th FIRE II cirrus case study. Preprints, *FIRE Cirrus Science Conf.*, June 14-17, 1993, Breckenridge, Colorado, 148-152.

Mahrer, Y. and R.A. Pielke, 1977: A numerical study of the airflow over irregular terrain. *Beitrage zur Physik der Atmosphare,* **50**, 98-113.

Matrosov, Sergey Y. 1993: Microphysical properties of the November 26 cirrus cloud retrieved by doppler radar/IR radiometer technique. Preprints, *FIRE Cirrus Science Conf.*, June 14-17, 1993, Breckenridge, Colorado, 44-47.

Meyers, M.P.,P.J. DeMott, and W.R. Cotton, 1992: New primary ice nucleation parameterizations in an explicit cloud model. *J. Appl. Meteor.,* **31**, 708-721.

Meyers, M.P., R.L. Walko, J.L. Harrington, and W.R. Cotton, 1994: New RAMS cloud microphysics parameterization Part II: The two-moment scheme. Submitted to *Atmos. Res.*

Mitchell, David L., 1988: Evolution of snow-size spectra in cyclonic storms. Part I: Snow growth by vapor deposition and aggregation. *J. Atmos. Sci.*, **45**, 3431-3451.

Mitchell, David L., 1994: A model predicting the evolution of ice particle size spectra and radiative properties of cirrus clouds. Part I: Microphysics. *J. Atmos. Sci.*, In press.

Mitchell, David L., and W. Patrick Arnott, 1994: A model predicting the evolution of ice particle size spectra and radiative properties of cirrus clouds. Part II: Dependence of absorption and extinction on ice crystal morphology. *J. Atmos. Sci.*, In press.

Nickerson, E.C., 1979: On the numerical simulation of airflow and clouds over mountainous terrain. *Contrib. Atmos. Phys.*, **52**, 161-177.

Peilke, R.A., W.R. Cotton, R.L. Walko, C.J. Tremback, W.A. Lyons, L.D. Grasso, M.E. Nicholls, M.D. Moran, D.A. Wesley, T.J. Lee, J.H. Copeland, 1992: A comprehensive meteorological modeling system–RAMS. *Metero. and Atmos. Phys.*, **49**, 69-91.

Pitter, R.C. 1977: A reexamination of riming on thin ice plates. *J. Atmos. Sci.*, **34**, 684-685.

Sassen, K., 1992: Evidence for liquid-phase cirrus cloud formation from volcanic aerosols: climatic implications. *Science*, **257**, 516-519.

Schlamp, R.J., H.R. Pruppacher, and A.E. Hamielec 1975: A numerical investigation of the efficiency with which simple columnar ice crystals collide with supercooled water drops. *J. Atmos. Sci.*, **32**, 2330-2337.

Schlamp, R.J. and H.R. Pruppacher, 1977: On the hydrodynamic behavior of supercooled water drops interacting with columnar ice crystals. *Pure and Applied Geophys.*, **115**, 805-843.

Stackhouse, P.W., and G.L. Stephens, 1991: A theoretical and observational study of the radiative properties of cirrus. Results from FIRE 1986. *J. Atmos. Sci.*, **48**, 2044-2059.

Starr, D.O. and S.K. Cox, 1980: Characteristics of middle and upper tropospheric clouds as deduced from rawinsonde data. Atmospheric Science Paper 327, Deparment of Atmospheric Science, Colorado State University, Fort Collins, CO.

Starr, D.O. and S.K. Cox, 1985: Cirrus clouds. Part I: A cirrus cloud model. *J. Atmos. Sci.*, **42**, 2663-2680.

Starr, D.O. and S.K. Cox, 1985: Cirrus clouds. Part II: Numerical experiments on the formation and maintenance of cirrus. *J. Atmos. Sci.*, **42**, 2682-2694.

Stephens, G.L., S. Tsay, P.W. Stackhouse, Jr., and P.J. Flatau 1990: The relevance of microphysical and radiative properties of cirrus clouds to climate and climate feedback. *J. Atmos. Sci.*, **47**, 1742-1753.

Tremback, C. J., 1990: Numerical simulation of a mesoscale convective complex: model development and numerical results. Ph.D. dissertation, Atmos. Sci. Paper No. 465, Colorado State University, Dept. of Atmospheric Science, Fort Collins, CO 80523.

Tremback, C.J. and R. Kessler, 1985: A surface temperature and moisture parameterization for use in mesoscale numerical models. Preprints, *7th Conference on Numerical Weather Prediction*, 17-20 June 1985, Montreal, Canada, AMS.

Tremback, C.J., G.J. Tripoli, and W.R. Cotton, 1985: A regional scale atmospheric numerical model including explicit moist physics and a hydrostatic time-split scheme. Preprints, *7th Conference on Numerical Weather Prediction*, June 17-20, 1985, Montreal, Quebec, AMS.

Tripoli, G.J. and W.R. Cotton, 1981: The use of ice-liquid water potential temperature as a thermodynamic variable in deep atmospheric models. *Mon. Wea. Rev.*, **109**, 1094-1102.

Tripoli, G.J., 1986: A numerical investigation of an orogenic mesoscale convective system. Ph.D. dissertation, Colorado State University, Dept. of Atmospheric Science, Fort Collins, Colorado 80523, 290 pp. (Atmospheric Science Paper No. 401).

Uttal, Taneil and Janet M. Intrieri, 1993: Comparison of cloud boundaries measured with 8.6 mm radar and 10.6 μm lidar. Preprints, *FIRE Cirrus Science Conf.*, June 14-17, 1993, Breckenridge, Colorado, 107-110.

Vali, G., 1974: Contact ice nucleation by natural and artificial aerosols. *Conf. on Cloud Physics*, Tucson, Amer. Meteor. Soc., 34-37.

Vali, G., 1976: Contact-freezing nucleation measured by the DFC instrument. *Third International Workshop on Ice Nucleus Measurements.* Laramie, Univ. of Wyoming, 159-178.

Verlinde, J., P.J. Flatau, and W.R. Cotton, 1990: Analytical solutions to the collection growth equation: Comparison with approximate methods and application to cloud microphysics parameterization schemes. *J. Atmos. Sci.,* **47**, 2871-2880.

Walko, Robert L., William R. Cotton, Jerry L. Harrington, and Michael P. Meyers, 1994: New RAMS cloud microphysics parameterization. Part I: The single-moment scheme. Submitted to *Atmos. Research.*

Young, K.C., 1974a: The role of contact nucleation in ice phase initiation in clouds. *J. Atmos. Sci.*, **31**, 768-776.

Zeigler, Conrad L., 1988: Retrieval of thermal and microphysical variables in observed convective convective storms. Part II: Sensitivity of cloud processes to variation of the microphysical parameterization. *J. Atmos. Sci.*, **45**, 1072-1090.

892007 E